Effect of Temperature on Lithium-Iron Phosphate Battery Performance and Plug-in Hybrid Electric Vehicle Range

by

Joshua Lo

A thesis
presented to the University of Waterloo
in fulfillment of the
thesis requirement for the degree of
Master of Applied Science
in
Mechanical Engineering

Waterloo, Ontario, Canada, 2013

AUTHOR'S DECLARATION

I hereby declare that I am the sole author of this thesis. This is a true copy of the thesis, including any required final revisions, as accepted by my examiners.

I understand that my thesis may be made electronically available to the public.

Abstract

Increasing pressure from environmental, political and economic sources are driving the development of an electric vehicle powertrain. The advent of hybrid electric vehicles (HEVs), plug-in hybrid electric vehicles (PHEVs), and battery electric vehicles (BEVs) bring significant technological and design challenges. The success of electric vehicle powertrains depends heavily on the robustness and longevity of the on-board energy storage system or battery. Currently, lithium-ion batteries are the most suitable technology for use in electrified vehicles. The majority of literature and commercially available battery performance data assumes a working environment that is at room temperature. However, an electrified vehicle battery will need to perform under a wide range of temperatures, including the extreme cold and hot environments. Battery performance changes significantly with temperature, so the effects of extreme temperature operation must be understood and accounted for in electrified vehicle design. In order to meet the aggressive development schedules of the automotive industry, electrified powertrain models are often employed. The development of a temperature-dependent battery model with an accompanying vehicle model would greatly enable model based design and rapid prototyping efforts.

This paper empirically determines the performance characteristics of an A123 lithium iron-phosphate battery, re-parameterizes the battery model of a vehicle powertrain model, and estimates the electric range of the modeled vehicle at various temperatures. The battery and vehicle models will allow future development of cold-weather operational strategies. As expected the vehicle range is found to be far lower with a cold battery back. This effect is seen to be much more pronounced in the aggressive US06 drive cycle where the all-electric range was found to be 44% lower at -20°C than at 25°C. Also it was found that there was minimal impact of temperature on range above 25°C,

Acknowledgments

First and foremost, I thank God for our wonderfully complex universe; for the faculty and facility to unravel its mysteries; and for Jesus Christ, by whom all my work is worth the while.

My education and development has been shaped tremendously by the dedication, encouragement, and guidance of Dr. Michael Fowler. Throughout my undergraduate and graduate career, he constantly provided the opportunities that allowed me to discover and nurture my love for engineering and design. For this I am deeply grateful. His patience and support throughout the preparation of this thesis is also greatly appreciated.

The University of Waterloo Alternative Fuels Team has been for me a place of much laughter, frustration, delight, and coffee. I have learned a great deal from this highly motivated and passionate group; and I will always remember fondly our struggles and triumphs together. I would like to acknowledge Dr. Roydon Fraser's outstanding dedication to the team and for always keeping us on the right track.

To my housemates Jonathan Lin, Jorge Quan, Alan Mak, and Joses Wong, thank you for many excellent conversations, hot food on the stove, and solidarity as fellow graduate students. To the group that met in our house weekly, thank you for your warmth and friendship.

Thank you to my family, Patrick, Cecilia, and Rebecca Lo, who have been an unwavering bastion of love, support and encouragement throughout my university career and in all my endeavours.

Finally, thank you Sophie, for always cheering me on with a smile.

Table of Contents

List of Figures

List of Tables

List of Equations

1 Objective

The objective of this project is to contribute to the model based design process of designing a plug-in hybrid electric vehicle (PHEV) powertrain considering battery performance based on temperature. Thus this project involves:

- Expanding a simple battery model to include the effects of temperature on battery performance, using experimental data collected for the battery chemistry under consideration;
- Modeling a powertrain over typical drive cycles for a specific vehicle platform; and,
- Modeling the powertrain over typical drive cycles at different temperatures to demonstrate cold and hot start performance on the electric range.

The model will also be parameterized for a specific battery and chemistry currently being used at the University of Waterloo. Direction for further model development and adaptation for different chemistries is given. The University of Waterloo Alternative Fuels Team (UWAFT) is designing a plug-in hybrid electric vehicle (PHEV) as part of EcoCAR2, a North American collegiate automotive engineering competition. The goal of this project is to produce a temperature dependent battery model suitable for software-in-the-loop (SIL) and real-time hardware-in-the-loop (HIL) simulation based on this specific vehicle platform. The expanded model will accelerate the development of battery pack thermal management and cold-weather start control strategies. The author of this work contributed to the model based design process of the UWAFT team with the overall selection and sizing of the powertrain components, and the initial development of a powertrain model and control system primarily through the use of vehicle modeling in Autonomie software, and translation that model to a dSpace software-in-the-loop (SIL) environment.

2 Introduction

In 2007, there were nearly 20 million vehicles on Canadian roads, traveling some 332 billion kilometres using 31.6 billion litres of gasoline and 11 billion litres of diesel fuel. Of these totals, 19 million vehicles were light duty vehicles, which include cars, vans, SUVs, and pickup trucks. Light duty vehicles accounted for 300 billion kilometres traveled and 31.3 billion litres of gasoline consumed [**1**]. Road transportation is one of the largest sources of greenhouse gases (GHG) in Canada and contributes significantly to urban air quality problems [**2**]. By displacing gasoline usage through the adoption of alternative fuels and propulsion technologies, Canadian GHG emissions can be significantly lowered and urban air quality increased. Vehicles using alternative fuels and powertrains are available, but their current market penetration is low, primarily a result of high cost and low consumer acceptability at this time.

Electrified vehicles achieve improvements in fuel consumption in different ways depending on the size and capability of their electrical energy storage system (ESS). "Mild" hybrids enable quick engine "stop-start" capability that allows the engine to turn off during idling. Hybrid electric vehicles (HEVs) have limited electric traction capabilities, such as at low speed or peak power events. Plug-in hybrid electric vehicles (PHEVs) can be charged using grid electricity and can operate electric-only for a limited range. An internal combustion engine (ICE) or fuel cell primary power system is required to extend the range of the PHEV. Lastly, battery electric vehicles (BEVs) are purely electric and do not contain an ICE or any other range extending technology.

Although PHEVs and BEVs can achieve "zero-emissions" at the tailpipe when operated in an all-electric mode, they are instead responsible for extra emissions at the power generation station, since they are charged using grid electricity. Their impact is therefore highly dependent on the cleanliness of the local power mix, when they are charged, as well as their market share.

Overall, Canada has a clean power mix, especially in Ontario. The distribution is shown in Figure 1. Hydro, nuclear, and wind account for 75% of the country's power generation. Coal, natural gas, and oil power generation accounts for the remainder.

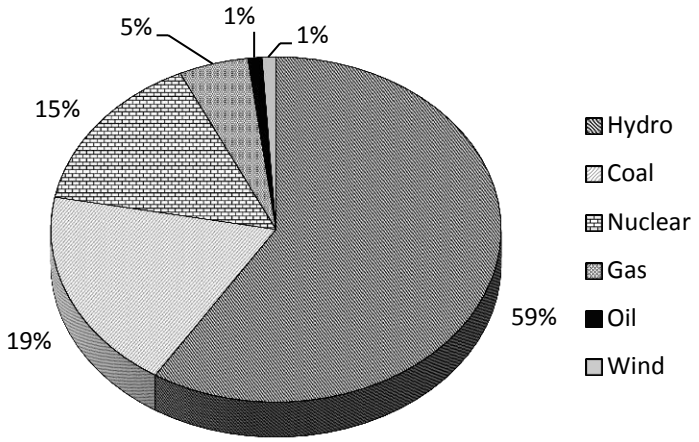

Figure 1 - Canada's electric power mix by fuel (2007) [3**]**

The adoption of electrified vehicles is generally expected to increase through 2020, but estimates vary widely beyond this due to the varying assumptions and models used for prediction [**4**]. Factors that will encourage the adoption of PHEVs in the marketplace include the decreased availability of petroleum resources due to natural resource depletion, geopolitical factors, and other drivers of increased petroleum prices. The challenges that PHEVs must overcome include high battery costs; range limitations; charging time limitations; battery durability; competition from improvements in conventional ICE powertrains; competition from other alternative fuels such as compressed natural gas and hydrogen; and yet-unproven real world reliability and durability.

The design and operation of electrified vehicles, revolves around its on-board energy storage system (ESS). Electrical energy may be stored in a variety of ways: electrochemically in a battery; chemically as hydrogen which is transformed via fuel cell; mechanically in a flywheel; or electrostatically in a capacitor bank. Research is actively being pursued in each of these technologies, but batteries are currently seen as the most suitable solution for most vehicle electrification applications.

A battery enables several important fuel conserving features of HEVs and PHEVs:

1. Recovery of vehicle kinetic energy through regenerative braking;
2. More frequent operation of ICE in its high efficiency regions by acting as a buffer between the power produced by the ICE and the powertrain load requirements (i.e. torque demands);
3. Downsizing of ICE by utilizing battery energy for a power split to meet powertrain load, which also reduces weight.

Since BEVs do not contain an ICE, it consumes no on-board fuel at all, but regenerative braking is still a critical feature in conserving electric energy.

Lithium-ion batteries have become the dominant choice for PHEVs and BEVs today. Nickel-metal hydride batteries are still attractive for HEV applications due to their lower cost, but lithium-ion batteries are quickly eroding this position. Lithium ion batteries are more compact and are suitable for a greater variety of vehicles [**5**]. This work focuses on lithium-ion chemistries.

Batteries used in PHEV and BEV applications must perform under very demanding conditions. Some of the critical criteria to evaluate a battery against include: battery capacity; maximum charge and discharge rate; energy density; power density; cycle life; and calendar life.

The battery capacity required is determined by the usage profile of the application and the desired time between charges. Battery capacity refers to the total accessible amount of energy that may be stored, and is expressed in watt-hours (Wh) or amp-hours (Ah). The greater the capacity, the further a PHEV can travel without using any gasoline. Care must be taken to correctly interpret manufacturers' published capacity specifications. Amp-hour capacities are based on a discharge at a specific C-rate and may change at other C-rates. A rate of 1C is equivalent to the current at which the battery would be fully discharged in one hour. The SAE standard currently prescribes a C/20 rate for determining battery capacity. Capacities expressed in watt-hours may be given as the simple product of a battery's amp-hour capacity and its nominal voltage.

Charge rate refers to the amount of power that may be used to charge the battery and is given in watts (W) or kilowatts (kW). A high maximum charge rate allows for more aggressive regenerative braking and faster charging of the battery.

Discharge rate refers to the amount of power that the battery may discharge, and is given in watts (W) or kilowatts (kw). High discharge rate capability allows the vehicle to accelerate quickly and improves the vehicle's grade-climbing ability.

Energy density refers to the energy that a battery can store per unit volume or mass, and is typically expressed in $kWh.kg^{-1}$ or $kWh.L^{-1}$. In PHEVs and BEVs, space is very limited, so a high energy density by volume will allow the vehicle to store more energy and have a greater "all electric" range. A high energy density by mass allows the vehicle to be lighter, decreasing energy consumption and improving efficiency.

Power density refers to the power that a battery can deliver per unit volume or mass, and is typically expressed in $kW.kg^{-1}$ or $kW.L^{-1}$. Higher power density enables a vehicle to achieve higher acceleration and dynamic performance.

Cycle life refers to the number of times that a battery may be charged and discharged before it degrades past the point of usefulness. Assuming that a vehicle battery is drained and recharged once each day, the battery must have a cycle life of over 3600 cycles to meet a10 year service life.

Calendar life refers to the elapsed time before a battery degrades past the point of usefulness. A vehicle battery is idle most of the time, so degradation due to age must also be taken into account.

2.1 Fuel economy

Rising petroleum costs, political pressure, and public environmental consciousness are all driving factors to reducing the consumption of fossil fuels. One measure of how efficiently a vehicle uses fuel is its fuel economy, which is expressed in the USA as miles per gallon (mpg). In most other countries express the metric as litres per 100 kilometers ($L.100^{-1}km^{-1}$) and is referred to as fuel consumption. Fuel economy is determined by subjecting a vehicle to different drive cycles on a dynamometer. The drive cycles imitate city and highway speed profiles and yield significantly different results. In North America, every vehicle has a separate "city" and "highway" fuel economy. The drive cycles used to determine fuel economy is discussed in greater detail in Section 3.2.1.

Increasing vehicle fuel economy usually involves either improving the efficiency the ICE operation, lowering the weight or drag of the vehicle, or increasing powertrain efficiency through vehicle electrification. Figure 2 compares the city and highway cycle powertrain efficiency of all 2011 model year vehicle sold in the USA. Diesel engines have traditionally been more efficient than gasoline engines due to their lean operation and higher combustion temperature, but technologies such as turbochargers and gasoline direct injection (GDI) have nearly eliminated any difference in efficiency. Hybrid vehicles hold no advantage against conventional ICE powertrains on the highway, but are significantly more efficient in the city.

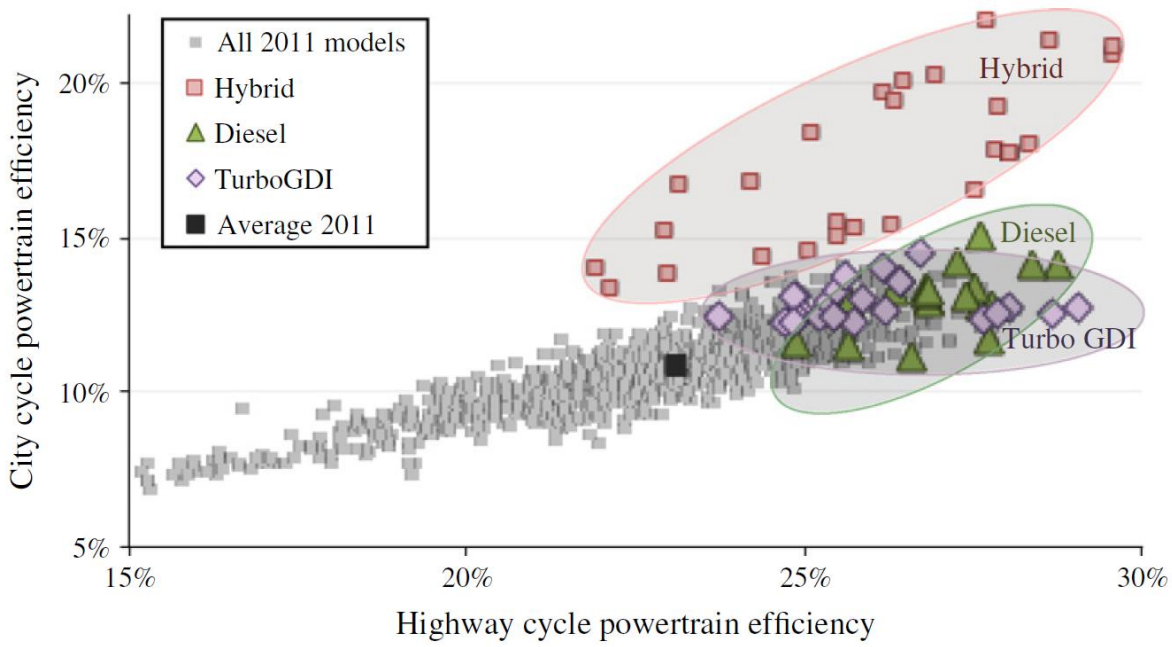

Figure 2 – City and highway powertrain efficiencies of 2011 model year vehicles in the USA [6]

The relationship between powertrain efficiency and fuel economy is clearly shown in Figure 3. Again, gasoline vehicles with turbochargers and GDI perform very similarly to diesels. Hybrids show an improvement in both powertrain efficiency and fuel consumption. The most efficient vehicles, both in their powertrains and their energy consumption, are the plug-in and fuel cell vehicles, which only use 25-50% of the energy of their ICE counterparts. Fuel cell vehicles such as the Honda Clarity FCX and Mercedes Benz F-Cell are currently extremely limited in availability, but PHEVs such as the Chevrolet Volt and BEVs such as the Nissan Leaf and Smart Fortwo are available in volume.

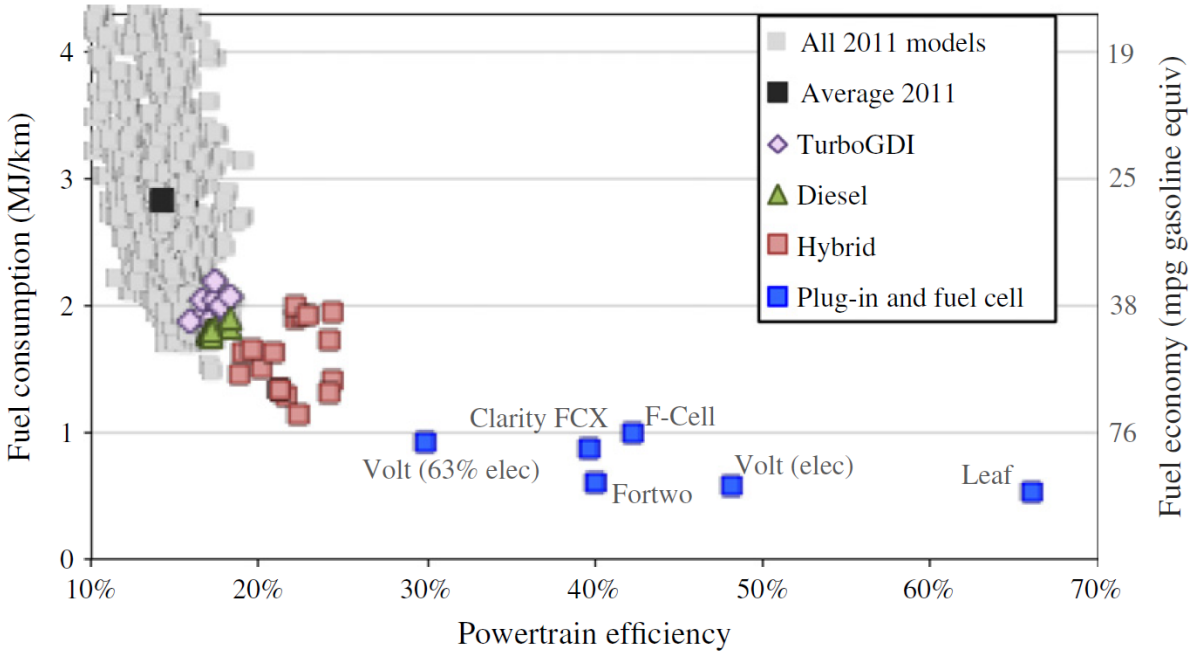

Figure 3 – Fuel consumption and powertrain efficiency of 2011 model year vehicles in the USA [6]

3 Background and Literature Review

The electrification of vehicles brings new layers of complexity in the design and optimization of vehicle powertrains. At the design stage, component sizing of the internal combustion engine, electrochemical energy storage system, motors, and generators must be delicately balanced to minimize weight and cost, maximize efficiency and fuel economy, and achieve dynamic performance targets.

3.1 Vehicle Technologies

3.1.1 Conventional Vehicles

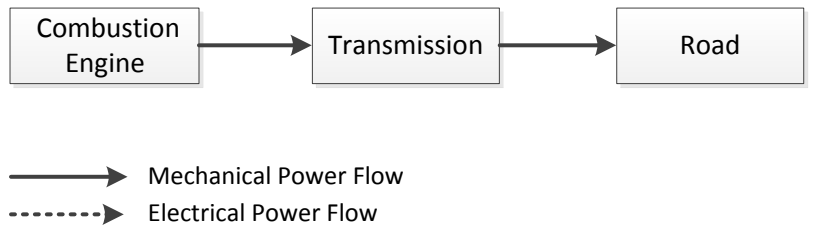

Figure 4- Energy flow in a conventional vehicle with an internal combustion engine

Most automobiles today utilize liquid fossil fuels such as gasoline and diesel as their primary energy source. To propel the vehicle, chemical energy of the fuel is first converted to mechanical energy through combustion in an internal combustion engine (ICE). Mechanical energy is sent through various mechanical linkages to the vehicle's transmission, final drive, axles, wheels, and finally to the road.

Due to losses in the powertrain, only about 10-20% of the fuel energy makes it to the road [**6**]. The large majority of the energy is lost as heat in the internal combustion engine. A typical gasoline ICE today has a most efficient operating point of 30-40%. Diesel ICEs may have maximum efficiencies upwards of 45% [**7**]. However, these efficiencies are not usually obtained in practise as the dynamic nature of real world operation pushes the engine into its less efficient operating regions much of the time.

Alternative combustion fuels such as compressed natural gas (CNG), liquefied petroleum gas (LPG), ethanol, and biodiesel have been adopted to varying degrees. Compared to gasoline and diesel, these fuels are less polluting, and they may be produced domestically or from renewable resources [**8**].

3.1.2 Battery Electric Vehicles

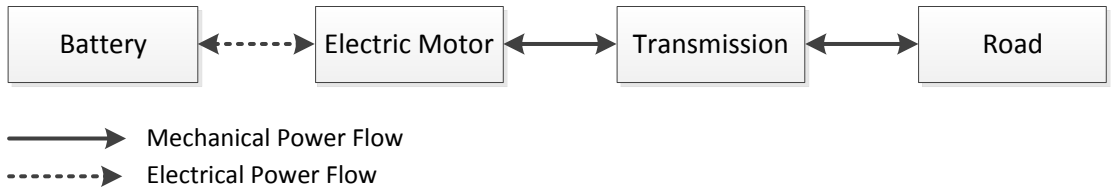

Figure 5 – Energy flow in a battery electric vehicle

In a battery electric vehicle (BEV), the primary energy source is a large battery pack which is charged using electricity from the grid. To propel the vehicle, DC electrical energy from the battery is converted to mechanical energy through an electric motor, which travels through the vehicle's transmission, final drive, axles, and wheels to meet the road load.

EVs are advantageous because they are very efficient and have zero emissions. For example, the commercially available Nissan LEAF has a powertrain efficiency in excess of 65% (refer to Figure 3). However, due to the energy storage limitations of today's battery technology, the range of EVs is much less than that of conventional or hybrid electric vehicles.

3.1.3 Hybrid Electric Vehicles (HEV)

As a combination of conventional and electric vehicles, hybrid electric vehicles achieve propulsion through both an internal combustion engine and an electric motor. A battery supplements engine power and allows the engine to operate in a more efficient region, thereby improving fuel economy. Depending on the configuration of the ICE, generator, electric motor(s), and battery pack, different hybrid electric architectures may be defined. Each architecture is

differentiated by the energy pathway by which the ICE and battery delivers power to the road. The main architectures are described below.

Series Hybrid

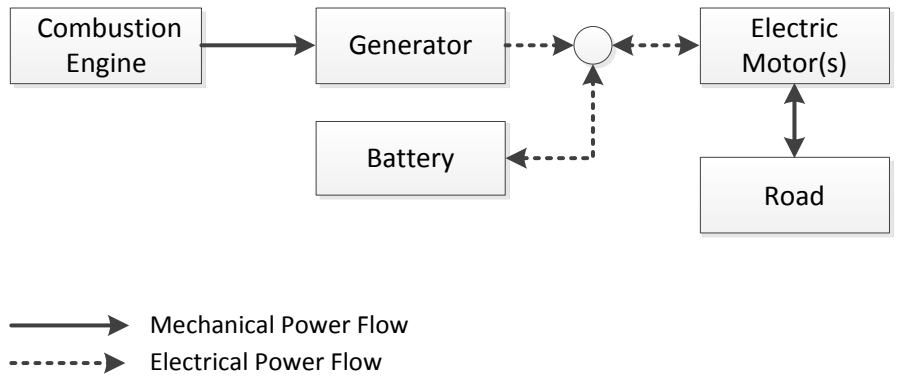

Figure 6 – Energy flow in a series hybrid electric vehicle

In a series architecture, all traction power is converted from electricity [**9**]. One popular way to conceptualize this architecture is to say that the ICE provides mechanical energy to the generator, which produces electricity to charge a battery, which in turn drives an electric motor to propel the vehicle [**10**], [**11**]. The two energy sources of a series hybrid are thus in series. While convenient, this explanation is misleading. The engine/generator is not electrically isolated from the motors by the battery. It would be more accurate to describe the series architecture as one where the summation of power from the two energy sources is realized on an electrical node from which the traction motors draw energy. Typically, this electrical node is a high-voltage DC bus [**12**].

The main advantage of the series architecture is that the ICE is mechanically decoupled from the road load. The ICE can therefore be controlled to always operate in its narrow, most efficient operating region. Flexibility in the physical placement of the genset within the vehicle is also greater than in other architectures. In vehicles with more than one traction motor, torque distribution strategies can be employed for a design that is both efficient and powerful.

Although the ICE is maximally efficient in a series hybrid, a penalty is incurred in the rest of the powertrain due to the large number of energy conversions required between the ICE and the road. All components must be sized for the full power of the powertrain, which increases weight and cost [**9**].

Parallel Hybrid

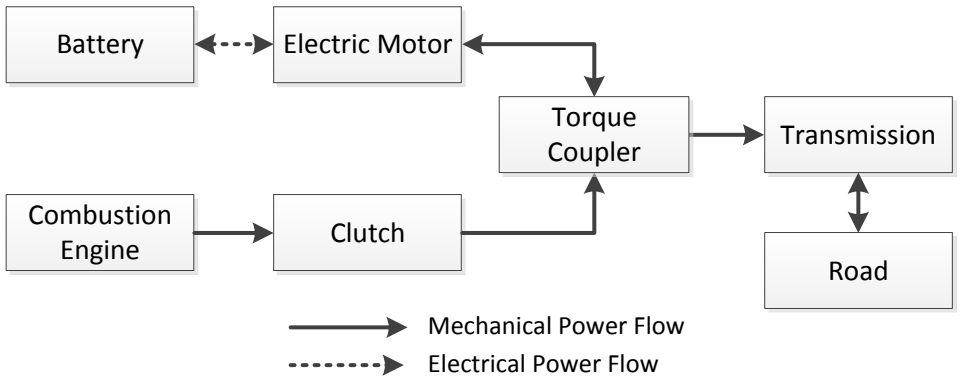

Figure 7 – Energy flow in a parallel hybrid electric vehicle (Adapted from [13**])**

In a parallel architecture, power from the ICE and battery are mechanically combined using a torque coupler. The connection between the ICE and the torque coupler is typically clutched. When the clutch is disengaged, the vehicle can be propelled using the battery alone, allowing for electric only, zero emissions operation. Three further operating modes can be achieved with the clutch engaged. First, the vehicle can be propelled using the ICE only by demanding no torque from the electric motor and letting it free-spin. Secondly, the two energy sources can simultaneously provide power to the transmission. Lastly, the ICE can be used to charge the battery by providing power in excess of the road load. The electric motor acts as a generator and charges the battery.

Parallel HEVs are advantageous in several ways. Compared to series HEVs, they require one less electric motor and a smaller engine and electric motors can be used without diminishing dynamic performance. As a result, cost and weight are reduced. Parallel HEVs are also incur fewer powertrain losses than series HEVs since there are fewer energy conversion steps.

The main disadvantage of the parallel architecture is that the ICE cannot always operate in its most efficient region, since the ICE speed is linked to vehicle speed through a mechanical connection. The parallel architecture is also not well suited where some all-electric range is required as it would require upsizing the electric motor and battery.

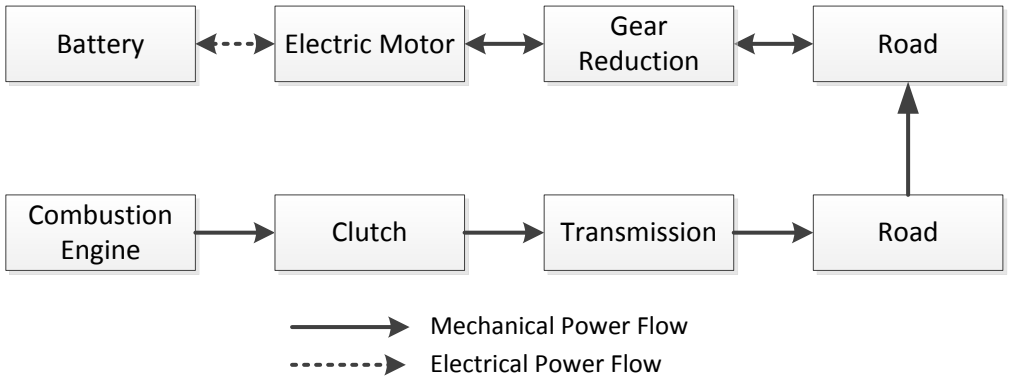

Figure 8 – Energy flow in a parallel-through-the-road hybrid electric vehicle

"Parallel Through the Road" (PTTR) is a variant of the parallel architecture in which the ICE and electric motor drive different axles of the vehicle. The torque coupling unit between the ICE and electric motor can therefore be removed, further reducing the weight, cost, and complexity of the parallel architecture. In order to charge the battery using the ICE, power is transferred through the road, from one axle to the other.

Though simple and inexpensive, PTTR architectures are inefficient due to the large losses of transferring energy through the road.

Split-parallel Hybrid

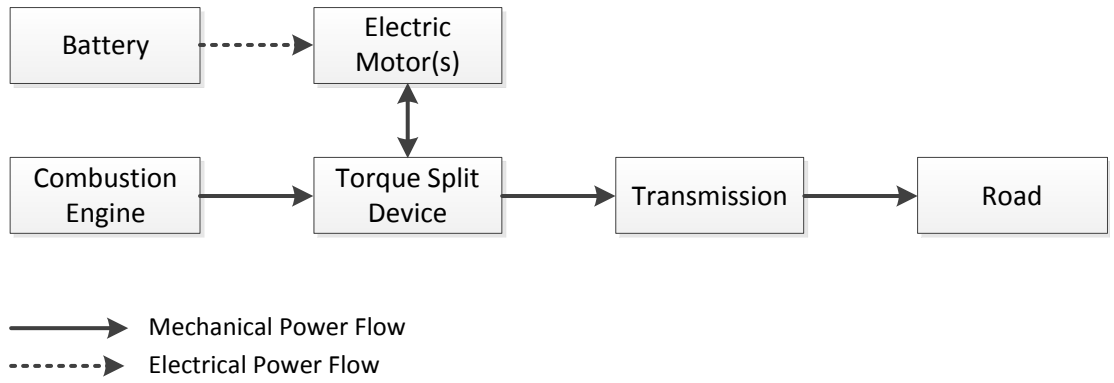

Figure 9 – Energy flow in series-parallel hybrid electric vehicle

The series-parallel architecture, also known as a split-parallel or power-split architecture, is a combination of the series and parallel architectures. Like a series HEV, the engine may be always operated in its highly efficient region. Like a parallel HEV, the ICE is able to provide torque to the wheels via mechanical linkages, without first converting to electricity. The series-parallel architecture's ability to both have maximally efficient ICE operation as well as a mechanical energy pathway from the ICE to the road load is due to a sophisticated torque splitting device.

There are several approaches to torque split devices for series-parallel applications. One method utilizes a planetary gear set, as shown in Figure 10 [**12**]. The ring gear is coupled to the first electric motor (EM1) and the transmission shaft. Vehicle speed is thus determined by the speed of the ring gear. The planet gears, held together by the carrier, are connected to the ICE, and the sun gear is connected to a second electric motor (EM2). The carrier speed is therefore a weighted average of the EM1 and EM2 speeds. EM1 speed is fixed by vehicle speed, but by varying EM2 speed, the speed of the carrier and ICE can be freely controlled, allowing the ICE to always operate efficiently. All electric operation is possible by controlling EM1 and EM2 such that the carrier speed is zero. The battery is charged either during regenerative braking events or by transferring power from the ICE through the sun gear to EM2, which acts as a generator [**14**].

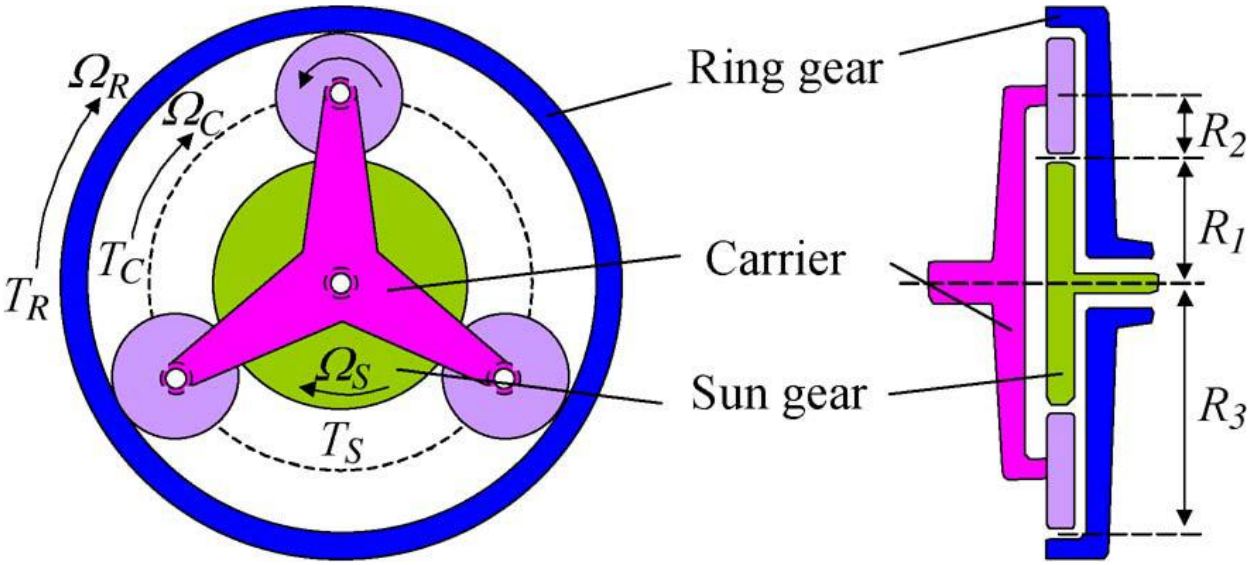

Figure 10 – Planetary gear set used in series-parallel HEVs [15**]**

3.1.4 Plug in Hybrid Electric Vehicles (PHEV)

PHEVs achieve excellent fuel economy by storing energy from the electric grid in the battery pack. The stored energy displaces the fossil fuel that would ha. Since the battery can be charged externally, PHEVs have two distinct modes of operation – charge depleting and charge sustaining. The charge depleting strategy is executed when the battery is at a high SOC. If the battery pack and electric motors are sufficiently large, a vehicle may have an all-electric charge depleting strategy, in which the battery exclusively supplies the entirety of the vehicle's tractive load. The engine remains off and the vehicle is, in essence, an EV. Series and split-parallel hybrids are the most amenable to this type of charge depleting operation. In vehicles where the battery pack and electric motors are smaller, an all-electric charge depleting strategy would result in a significant reduction in vehicle performance. A blended charge-depleting strategy in which engine use is permitted at opportune moments and at high efficiency points is more suitable.

Once the battery SOC reaches its minimum threshold, the PHEV enters its charge sustaining mode of operation. The net energy in or out of the battery is zero, and the vehicle behaves as an HEV would. The transition between charge depleting and charge sustaining regimes is shown in Figure 11.

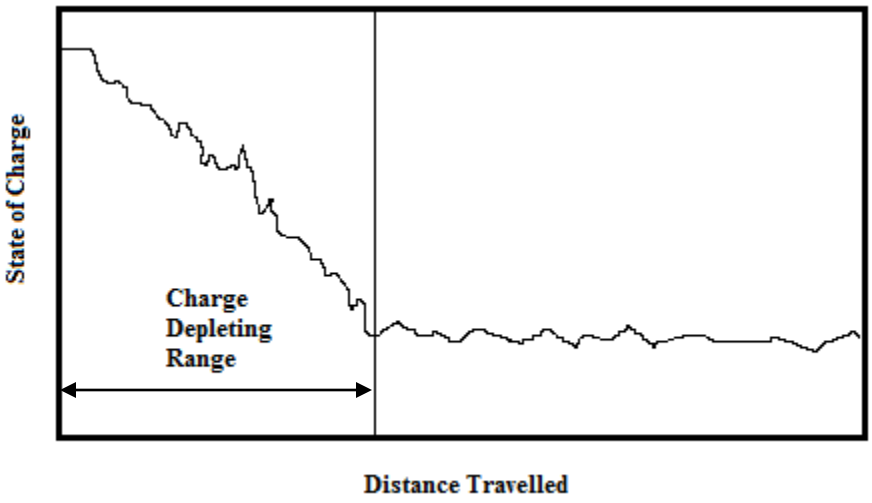

Figure 11 – Battery SOC during charge depleting and charge sustaining operation of PHEVs

3.2 Assessment of Fuel Economy

3.2.1 Drive Cycles

Driving characteristics such as the frequency and intensity of acceleration and deceleration events, vehicle speed, idling time, engine temperature, and accessory power demand have significant impacts on the energy consumption rate of a vehicle. During low speed urban driving, frequent acceleration, deceleration, and idling events typically result in a relatively high rate of energy consumption per distance traveled. When cruising at highway speeds, changes in speed are fewer, but greater aerodynamic drag must be overcome. At speeds above 100 km per hour, rolling resistance increases non-linearly [**16**].

The United States Environmental Protection Agency (EPA) currently prescribes a combination of five different drive cycles to evaluate the fuel economy of all new vehicles sold in the United States. Three of these evaluate fuel economy in urban and highway conditions. The other two deal specifically with the use of air conditioning and cold-start operation, but since there was insufficient information to meaningfully simulate air conditioning loads and cold-start behaviour, they are excluded from this work.

The Urban Dynamometer Drive Schedule (UDDS) simulates low-speed city driving, with relatively gentle acceleration and deceleration events. The drive cycle covers 7.45 miles and lasts 1369 seconds. Distance is expressed in miles as to be consistent with the U.S. based procedure. Vehicle speed generally stays below 40mph, with frequent stops.

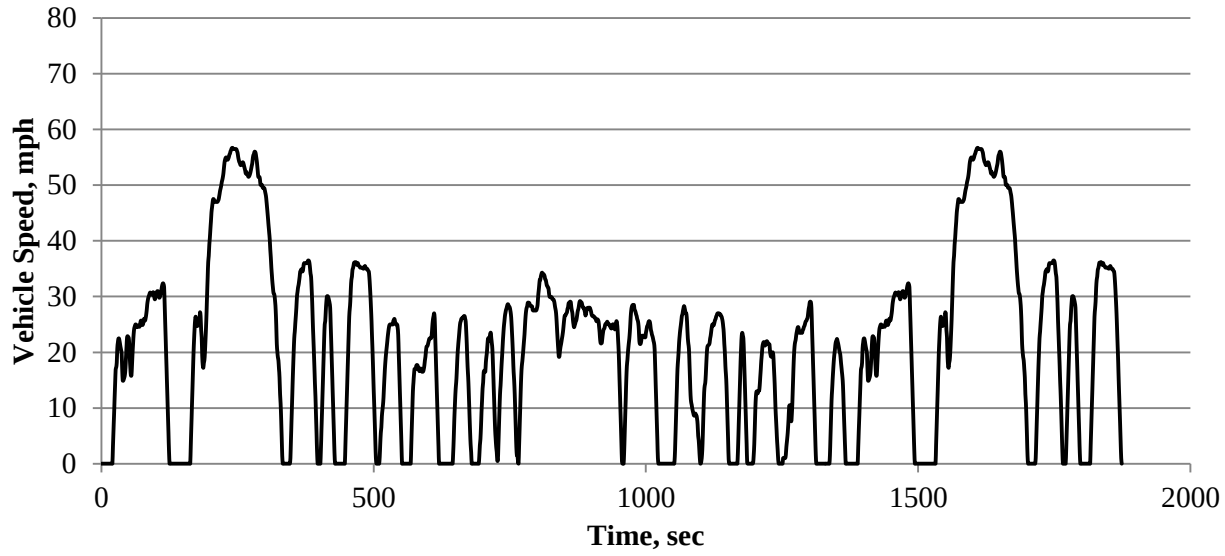

Figure 12 – Speed trace of the Federal Test Procedure (FTP) [17]

The HWFET cycle simulates highway driving below 60mph. The cycle covers 10.26 miles and lasts 765 seconds. In contrast to the UDDS, the vehicle does not come to a stop at any time during the HWFET cycle.

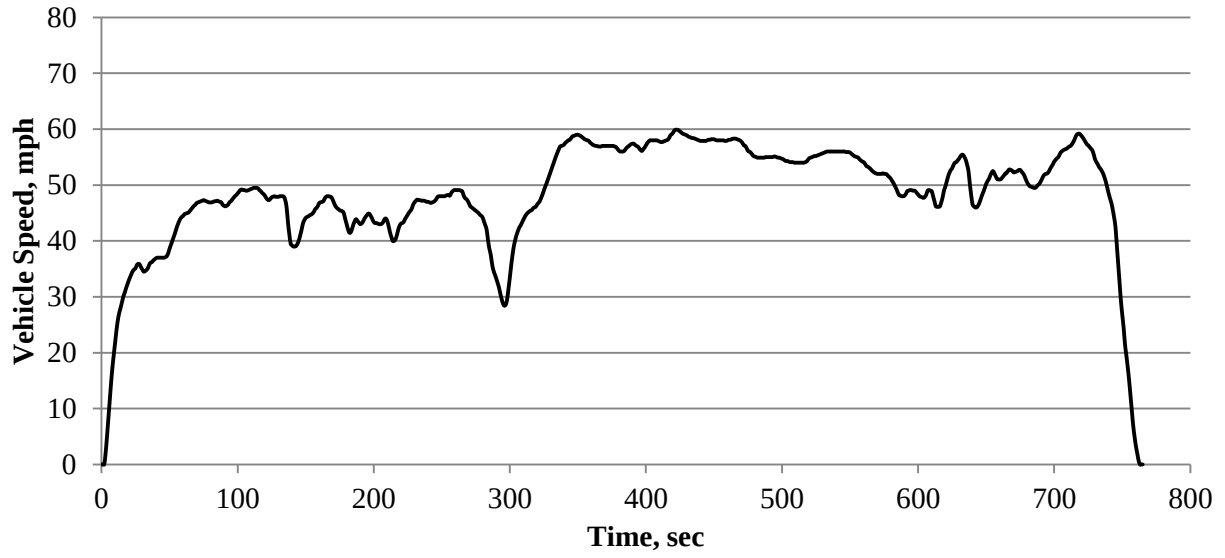

Figure 13 – Speed trace for the Highway Fuel Economy Driving Schedule (HWFET) [17]

The US06 is an aggressive profile with high rates of acceleration and deceleration, as well as higher speed. The US06 contains both city and highway portions. It covers a distance of 8.01 miles and lasts 596 seconds.

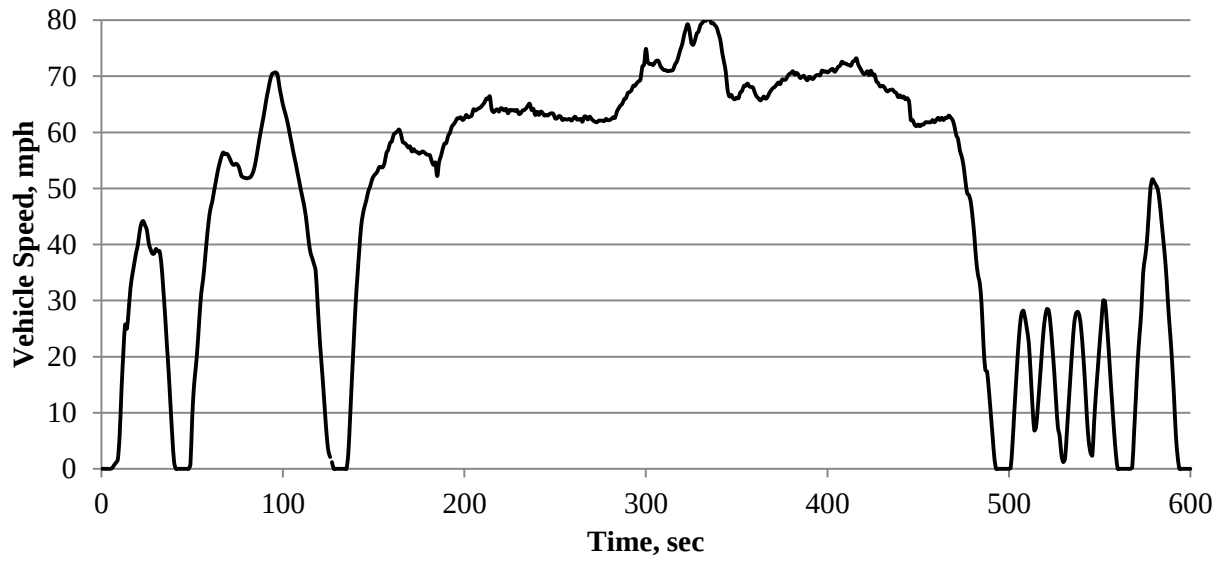

Figure 14 – Speed trace for the US06 Drive Cycle [17**]**

3.3 Model Based Design

Broadly, model based design refers to the use of a mathematical or empirical model of a system as an aid during the engineering design process. Spurred by accelerated development cycles and the need to meet stringent regulatory standards, model based design has become widely used in the development and validation of vehicle technologies. Virtual models save time and money by reducing the need to build physical prototypes. Designs can be iterated quickly and evaluated against the project requirements. Alternative designs can be easily investigated, and existing designs can be optimized.

Powertrain models have been increasingly important in vehicle component sizing [**18**,**19**], the advancement of vehicle control strategies [**20**,**21**,**22**,**23**], and fuel economy estimation [**24**,**18**].
A hybrid vehicle powertrain model typically includes the following items at a minimum:

- Fuel conversion device (e.g., ICE or fuel cell);
- Electric motor(s)/generator; and,
- Electrical energy storage device (e.g., battery, ultracapacitors).

Models may also consider, to varying degrees of fidelity: clutches, gearboxes, torque-split devices, catalytic converters, rolling resistances, aerodynamic drag, ambient temperature, and other components or environmental conditions of interest.

3.4 Modeling Software Structure

Hybrid vehicle powertrain models may causal or non-causal. In non-causal models, the vehicle speed is defined and powertrain component operating points are calculated in a backwards fashion. The desired vehicle speed is set and the necessary powertrain component operating points are determined. Because calculations begin at the wheels and propagate back to the energy source such as the engine or battery, non-causal models are often called “backward-facing” models. Accordingly, causal models start at the energy source and propagate through to the

wheels to arrive at vehicle speed, and are known as “forward-facing” models. Typically, causal models include a “driver”. That is, a controller attempts to meet the desired vehicle speed profile by manipulating a vehicle throttle.

Three major powertrain simulation tools that have been developed are ADVISOR and Autonomie, and AVL CRUISE. ADVISOR is a backward-facing model which is not well suited for simulating the transient behaviour of powertrain components and is not conducive to developing vehicle control strategies. Autonomie is a forward-facing simulator which allows for transient behaviour simulation through the use of a driver model as previously discussed. AVL CRUISE is similar to Autonomie, but comes with a less extensive model library than Autonomie.

In this work, the Autonomie software is used to perform powertrain energy simulations. It was favoured because of its modularity, large library of models and its highly configurable nature. Resources and support from UWAFT and the EcoCAR2 competition could also be leveraged, since Autonomie was also used for the competition.

Although the models in Autonomie are open-source and allow for unlimited configurability, one major limitation is the simplicity of the models. For example:

- Battery models did not evaluate time-variant phenomena such as ionic diffusion;
- Voltage dynamics such as bus capacitance is not evaluated; and,
- No consideration for component operating temperature.

3.5 Lithium Ion Batteries

3.5.1 Background

Lithium ion batteries are a relatively new battery technology currently undergoing immense growth and development. They have already become the preferred battery type for applications requiring high energy densities and light weight, such as portable media players and smartphones. There is also a shift in the expanding hybrid vehicle market towards lithium chemistries and away from NiMH batteries. In 2009, rechargeable lithium-ion batteries accounted for 11% of the $16.4 billion total US battery demand and is expected to be the fastest growing chemistry type through 2012. [**25**] The 2008 European lithium rechargeable market was similarly sized at $1.62 billion and is expected to grow to $1.76 billion by 2015 [**26**]. Notable deployments of li-ion batteries in the automotive market include the Chevrolet Volt, which is a range-extending electric vehicle (EREV), and the Nissan Leaf, which is a battery electric vehicle (BEV).

Lithium ion batteries offer advantages over other battery types in several areas. It has a high operating voltage of 3-5 volts, depending on the specific chemistry. This allows for an equivalent power operation at a lower current draw and the battery will last longer on a single charge. It has a high energy density, so lithium ion batteries are lightweight and compact. Unlike NiCad and older NiMH batteries, Li-ion batteries do not exhibit any memory effect, and they have long shelf lives. Additionally, they are capable of high discharge rates with high reversibility and good charge retention.

3.5.2 Chemistry

Common to all lithium-ion battery types is that the electrodes are made of lithium intercalation compounds, and lithium ions (Li^+) travel between the two as the battery cycles. Intercalation is a reversible process in which a species (Li^+, in this case), is inserted into a host with only minimal structural changes in the host. [**27**]

As with any galvanic cell, the two electrodes are separated from each other by an ionically conductive but electrically insulating medium. In a fully charged li-ion battery, the lithium ions are all intercalated into the anode and move through the electrolyte to the cathode during discharge. The mechanism is shown in Figure 15.

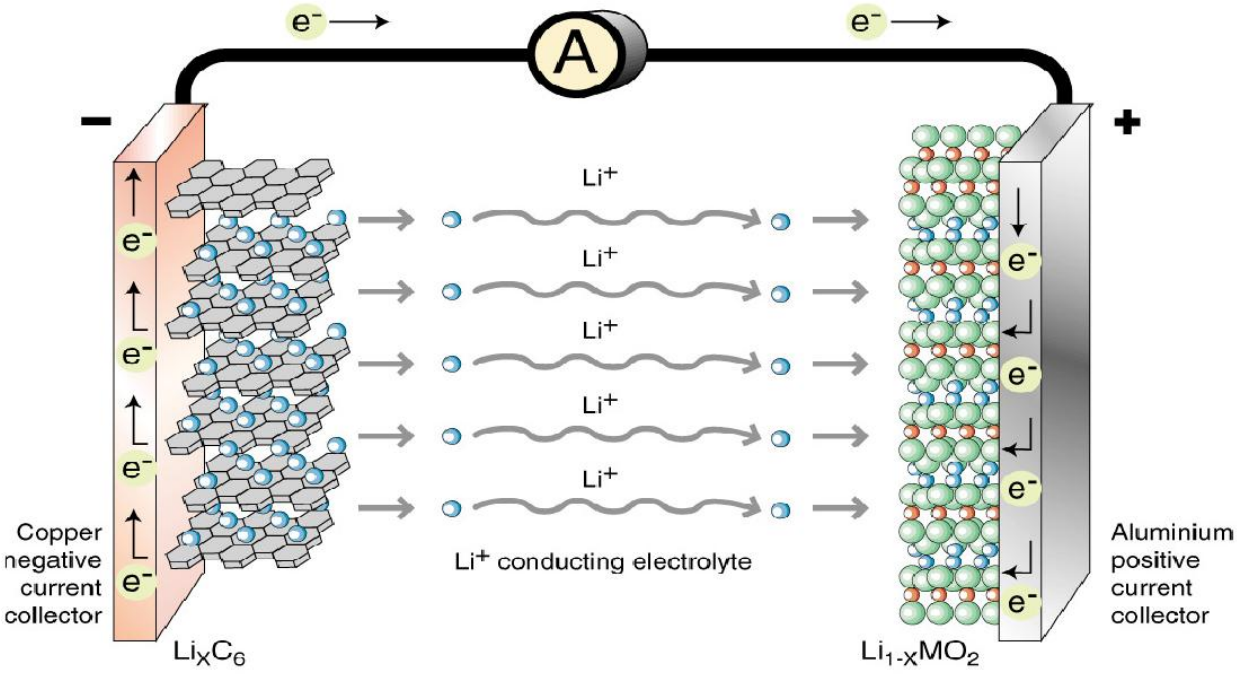

Figure 15 – Diagram of overall lithium-ion battery discharge mechanism [28**]**

For a graphite/metal oxide cell, the half-cell and overall reactions are as follows [**27**]:

Anode: $C + xLi^+ + xe^- \underset{\text{discharge}}{\overset{\text{charge}}{\rightleftharpoons}} Li_xC$

Cathode: $LiMO_2 \underset{\text{discharge}}{\overset{\text{charge}}{\rightleftharpoons}} Li_{1-x}MO_2 + xLi^+ + xe^-$

Overall: $LiMO_2 + C \underset{\text{discharge}}{\overset{\text{charge}}{\rightleftharpoons}} Li_xC + Li_{1-x}MO_2$

where C is a carbonaceous material, commonly graphite, and $LiMO_2$ is a lithium metal oxide.

During the initial charge-discharge cycles of a new battery, carbonaceous anodes react with the organic solvent electrolyte. The products include Li_2CO_3, ethylene, lithium alkyl carbonate and lithium alkoxide, some of which precipitate to form what is known as the solid electrolyte interface (SEI). This layer is critical to the stability of the anode and stops undesired reactions between the anode and the electrolyte. The quality of the SEI is also important to the performance and longevity of the battery. A thin, uniform layer that is conductive to lithium ions and insulating to electrons is most desirable. Additives such as vinylene carbonate, propylene sulphite and fluoroethylene carbonate, when used in conjunction with the right battery chemistry, can favourably influence SEI formation, improving SEI stability and increasing cycle life [**29**].

3.5.3 Cathode

Cathode materials are usually a metal oxide capable of intercalating lithium ions. It is important for the cathode to be able to hold large amounts of lithium without significant change in structure, be a good electrical conductor and diffusor of lithium ions, have good chemical and electrochemical stability with the electrolyte, and be of low cost. [**27**] The rate capability and thermal stability of the battery is also largely dependent on the cathode material [**30**].

Among cathode materials, $LiCoO_2$ is the most commonly used [**31**]. Lithium ions are intercalated between sheets of CoO_2 in a layered structure as shown in Figure 16. The theoretical specific capacity of $LiCoO_2$ is 274 $mAh.g^{-1}$, but an anisotropic structural change occurs at $Li_{0.5}CoO_2$, so the realizable capacity is limited to about 140-160$mAh.g^{-1}$ [**32**,**33**,**34**,**35**]. Coatings such as $AlPO_4$ have been developed to improve capacity retention and thermal stability [**30**]. $LiCoO_2$ has good discharge capacity; 136 $mAh.g^{-1}$ at a 5C rate has been demonstrated with multiwalled CNT augmented cathodes [**35**]. However, despite the attractive electrical properties of $LiCoO_2$ cathodes, cobalt is relatively expensive compared to other transition metals such as manganese and iron.

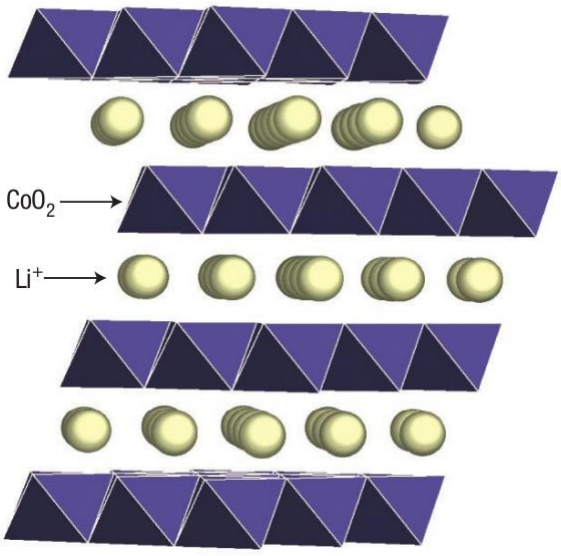

Figure 16 – Layered Structure of $LiCoO_2$ [36**]**

$LiMn_2O_4$ is a promising cathode material with a cubic spinel structure, shown inFigure 17. It has a theoretical specific capacity of 148 $mAh.g^{-1}$. Current designs achieve between 115 and 130 $mAh.g^{-1}$ at modest discharge rates of 1C or less [**37**,**38**,**39**]. A rate of 1C represents the current at which the battery would be depleted in exactly one hour. $LiMn_2O_4$ nanowire cathodes have been demonstrated to have excellent high power capabilities of 107 and 102 $mAh.g^{-1}$ at 5C and 10C, respectively and with virtually no capacity loss after 100 cycles. Other transition metals such as Ni, Co, and Fe can also be added to $LiMn_2O_4$ in varying amounts to increase capacity and improve capacity retention during cycling [**31**].

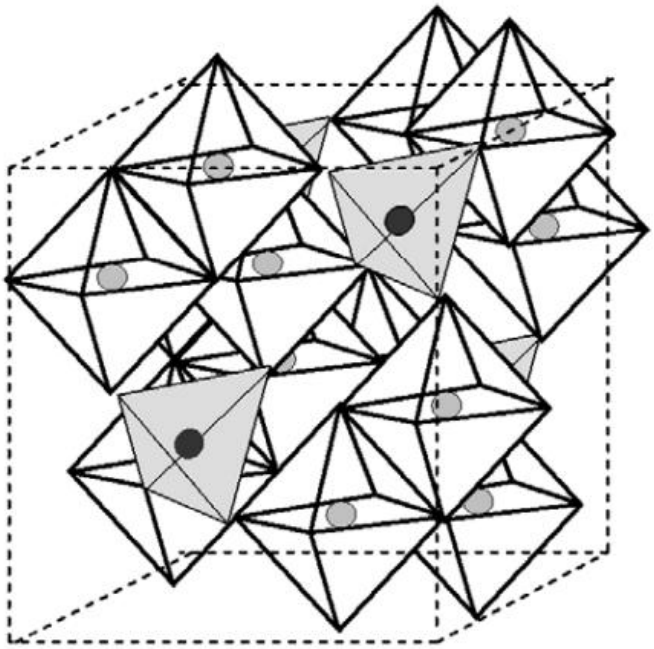

Figure 17 – Cubic crystal structure of $LiMn_2O_4$. The corners of each tetrahedral and octahedral are oxygen atoms. [40**]**

$LiFePO_4$ is one of the most recent cathode materials to be introduced. Its olivine structure, shown in Figure 18, is very different from the layered and spinel structures of other lithium ion chemistries, and its intercalation mechanism is also different, involving phase changes. It has a theoretical specific capacity of $170mAh.g^{-1}$, a figure which has been approached by recent advances [**41**]. A $LiFePO_4$/C composite material with a nano-carbon wire network has been shown to have excellent high rate performance, achieving 129 $mAh.g^{-1}$ at a 10C rate and retaining over 90% of its capacity after 400 cycles at 10C [**42**]. $LiFePO_4$ has the added advantage of being inexpensive and environmentally friendly.

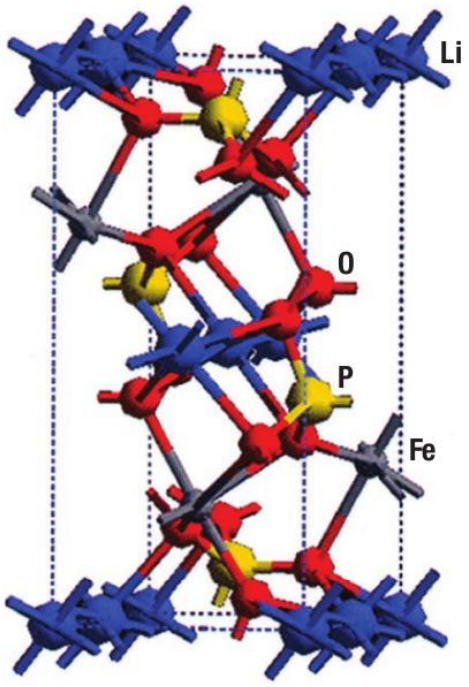

Figure 18 – Olivine structure of $LiFePO_4$ [43]

3.5.4 Anode

Anode materials are typically carbonaceous in nature. Similarly to the cathode, it is important for the anode to be able to hold large amounts of lithium without significant change in structure, be a good electrical and ionic conductor, have good chemical and electrochemical stability with the electrolyte, and be of low cost.

The most common anode material in lithium ion batteries today is graphite, stacked in layers as depicted in Figure 15. It undergoes a reversible lithium-intercalation reaction -from 0 to 0.2 V vs Li/Li^+ and is favoured for its small volume change during lithiation and delithiation [**44**]. High coulombic efficiencies of over 95% have been achieved with graphite anodes, but they have a relatively low theoretical specific capacity of 372 $mAh.g^{-1}$ [**45**]. Although this is already higher than the specific capacity of the commonly used cathode materials, higher specific capacity anodes are still desirable because they contribute to a lower overall battery density.

Among carbonaceous materials, carbon nanotubes (CNTs) are the most promising materials being developed. Purified CNTs of the single walled variety can reversibly intercalate lithium ions with a maximum composition of Li1.7C6, equivalent to 632 $mAh.g^{-1}$. Etching can increase the reversible capacity to 744 $mAh.g^{-1}$, and capacities as high as 1000 $mAh.g^{-1}$ have been reported using ball milling treatments [**46**]. Multiwalled CNTs have a reported reversible capacity of up to 640 $mAh.g^{-1}$. Although CNTs have high reversible capacities, they also have large irreversible capacities as high as 1488 mAh/g for purified single walled CNTs [**46**]. This lithium, which cannot be cycled, causes growth of SEI and reduces overall capacity. Two major issues that must be solved before CNT anodes can be widely adopted are excessive irreversible capacity and methods of large-scale fabrication. [**29**]

Silicon is the leading alternative anode material to carbon and has been extensively researched. Pure Si anodes alloy readily with lithium and have a huge theoretical capacity of 4200 $mAh.g^{-1}$, but are impractical as they undergo great volumetric changes and thus have poor cycleability. Composite materials have been developed to mitigate the effects of mechanical stresses of lithiation and delithiation. One method is to house the active silicon material in inert matrices made of materials such as C (eg graphite, pitch, CNTs), TiC, SiC, TiN, or Cu/C. The inactive matrix absorbs the mechanical stresses and strains experienced by the active phase, resulting in improved cyclability. Nanowires have also been proposed as an anode material because lithium diffusion occurs only in one dimension and mechanical stresses can be well accommodated. Low cyclability even at small currents and significant irreversible capacities remain challenges in the development of silicon based anodes. [**29**]

3.5.5 Electrolyte

The choice of electrolyte in lithium ion batteries is critical to both performance and safety. The electrolyte is typically a lithium salt dissolved in organic solvents. A good electrolyte must have high ionic conductivity, low reactivity with other cell components, low toxicity a large window of electrochemical voltage stability (0-5V), and be thermally stable [**27**].

Typically, in liquid electrolytes for lithium ion batteries, a mixture of alkyl carbonates such as ethylene carbonate (EC), dimethyl carbonate (DMC), diethyl carbonate (DEC), and ethyl-methyl carbonate (EMC) is used with $LiPF_6$ as the dissolved lithium salt. EC is a necessary component for adequate SEI growth. Many lithium salts are possible, but it is difficult to find one that is chemically stable, safe, and forms a high conductivity solution. $LiPF_6$ offers the best compromise between these criteria and has been the long-time standard in lithium ion batteries. Some of the well known salts and their major disadvantages are shown in Table **1** [**47**].

Table 1 **- Well known lithium salts for use in electrolytes and their major disadvantages**

Salt	**Disadvantages**
$LiAsF_6$	Toxic
$LiClO_4$	Thermal runaway leading to explosion
$LiBF_4$	Interferes with anode passivation
$LiSO_3CF_3$	Low Conductivity
$LiN(SO_2CF_3)_2$	Corrodes aluminum cathode current collector
$LIC(SO_2CF_3)_3$	Corrodes aluminum cathode current collector
$LiPF_6$	Thermally decomposes to HF and PF_3O, deteriorates both anode and cathode

The main objective of electrolyte development has been to improve the thermal operating range of lithium ion batteries. Current batteries rapidly deteriorate above 60°C. High operating temperatures are very desirable in high discharge applications where the amount of cooling available is limited, such as on electric vehicles.

Certain boronate salts have been found to improve thermal stability, particularly an unsubstituted five member ring salt known as LiBOB. Cells using this salt were successfully cycled at 60°C without degradation, but the salt is difficult to prepare. [**48**] A combination of $LiPF_6$ + $LiPF_3(CF_2CF_3)_3$ salts have also been proposed which maintain cyclability even after 100 cycles at 80C with moderate capacity loss. [**47**]

LiBOB has been investigated as an additive to standard $LiPF_6$ based electrolytes and was observed to stabilize the SEI, reduce degradation of cathode materials and improve overcharge tolerance [**49**].

Ionic liquids have also been proposed as an alternative to alkyl solvents as they are generally good flame retardants and have low heats of reaction. In addition to enhanced safety, ionic liquids have very high ion concentrations, so transport kinetics are favourable. However, ionic liquids are expensive and do not tend to facilitate SEI formation, so they are only stable at lower voltages. [**48**]

4 Experimental

4.1 Batteries

In this work, A123 Systems AMP20-M1-HD-A lithium ion prismatic pouch cells, shown in Figure 19, are tested. The cell specifications are given in Table 2. Two cells were tested – one from a batch supplied by General Motors, and the other from an aftermarket source. The two connections made to each tab of the cell connect to the power source/sink of the battery cycler and cycler's voltage sensing module.

Figure 19 - Commercial 20Ah $LiFePO_4$/graphite prismatic battery manufactured by A123 Systems

Table 2 - A123 Systems AMP20-M1-HD-A Battery Specifications

Cathode Material	$LiFePO_4$
Anode Material	Graphite
Electrolyte	Carbonate based
Rated Capacity (Ah)	20 (minimum 19.6)
Dimensions (mm)	7.25 x 160 x 227
Nominal Voltage (V)	3.3

4.2 Test Apparatus

The test bench used for cell characterization is shown in Figure 20. The four main pieces of equipment are the battery cycler, thermal chamber, bus boxes, and thermal data collection system. Each of these components is described in detail below.

Figure 20 - Battery cycling test bench

4.2.1 **Battery Cycler**

A Maccor 4200 battery cycler, shown in Figure 21, is used to charge and discharge the batteries. It comprises of 16 channels, each capable of delivering ±15A and ±5V. Channels may be combined in groups of 2, 4, or 8 to increase current capability to a maximum of 120A. Voltage, however, remains limited to ±5V. Current is accurate to ±7.5mA per channel, and voltage measurements is accurate to ±1mV. Both are reported with 16-bit resolution.

The cycler is controlled through a manufacturer-supplied computer interface, where test procedures are defined and data is collected. Procedures must have a minimum step time of 10ms, which is suitable for highly dynamic current profiles such as drive cycles. The smallest sampling time for data collection is also 10ms.

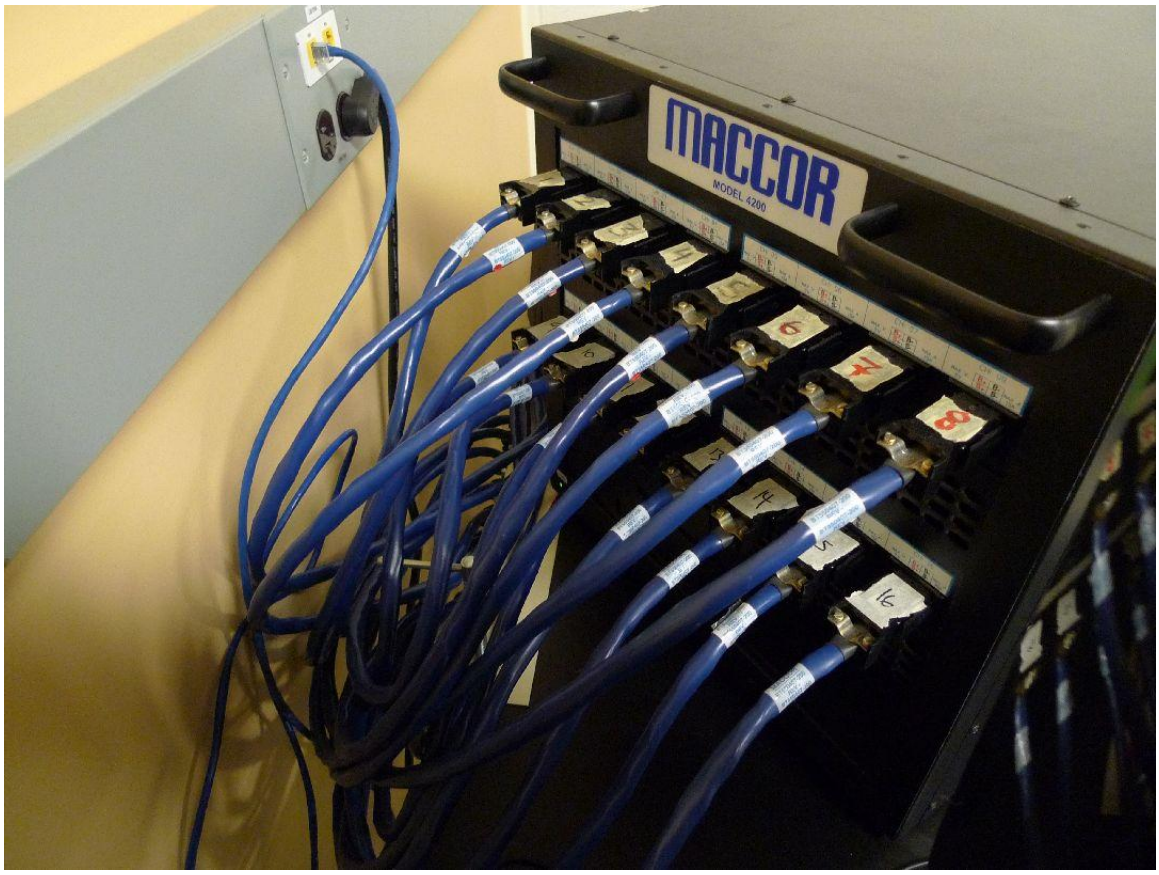

Figure 21 - Maccor 4200 Battery Cycler

4.2.2 Bus Boxes

In order to combine channels on the battery cycler for high current cycling, the terminals of the same polarity must be electrically connected. Two bus boxes were prepared, both sized to accommodate up to 8 channels and 120A. Copper bus bars act as current collectors and two lengths of 1AWG cable connects each bus box to the battery. An electrical schematic of the system is shown in Figure 22.

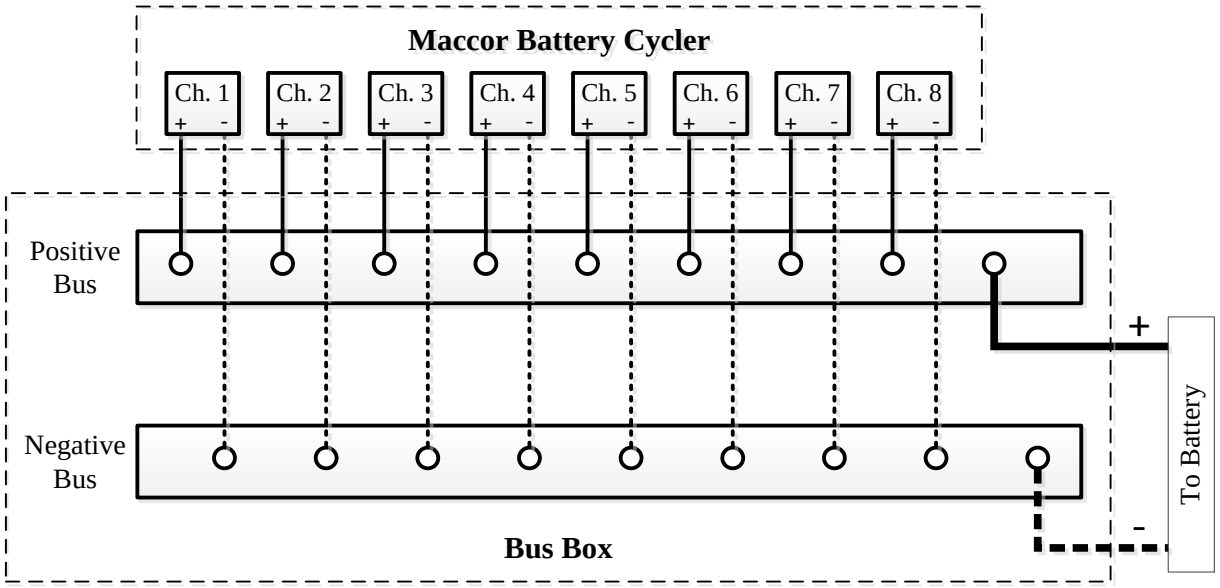

Figure 22 – Combined channel electrical schematic

4.2.3 Thermal Chamber

A Cincinnati Sub Zero (CSZ) MC-3 thermal chamber is used to subject the battery to different ambient temperatures. It is capable of simulating temperatures from -65ºC to +190ºC. A porthole on either side of the chamber allows passage of wires and cables. Two adjustable racks inside the chamber aid with battery positioning and cable routing. Non-conductive material is placed between the batteries and the metal racks to avoid battery shorts. The setup is shown in Figure 23.

Figure 23 - Picture of battery setup inside thermal chamber

4.2.4 FieldPoint

To collect oven and battery temperature, the National Instruments FieldPoint system is employed. Each of the two thermocouple sensor modules can accommodate up to eight thermocouples and has a 16-bit resolution. A custom LabView interface was created to log data.

Thermocouples suitable for use with the FieldPoint system were made in-house. At the time of data collection, only eight thermocouples were available. Two were used to measure oven temperature, and six were used to collect the surface temperature of one of the batteries. The layout of the thermocouples on the battery surface is shown in Figure 24.

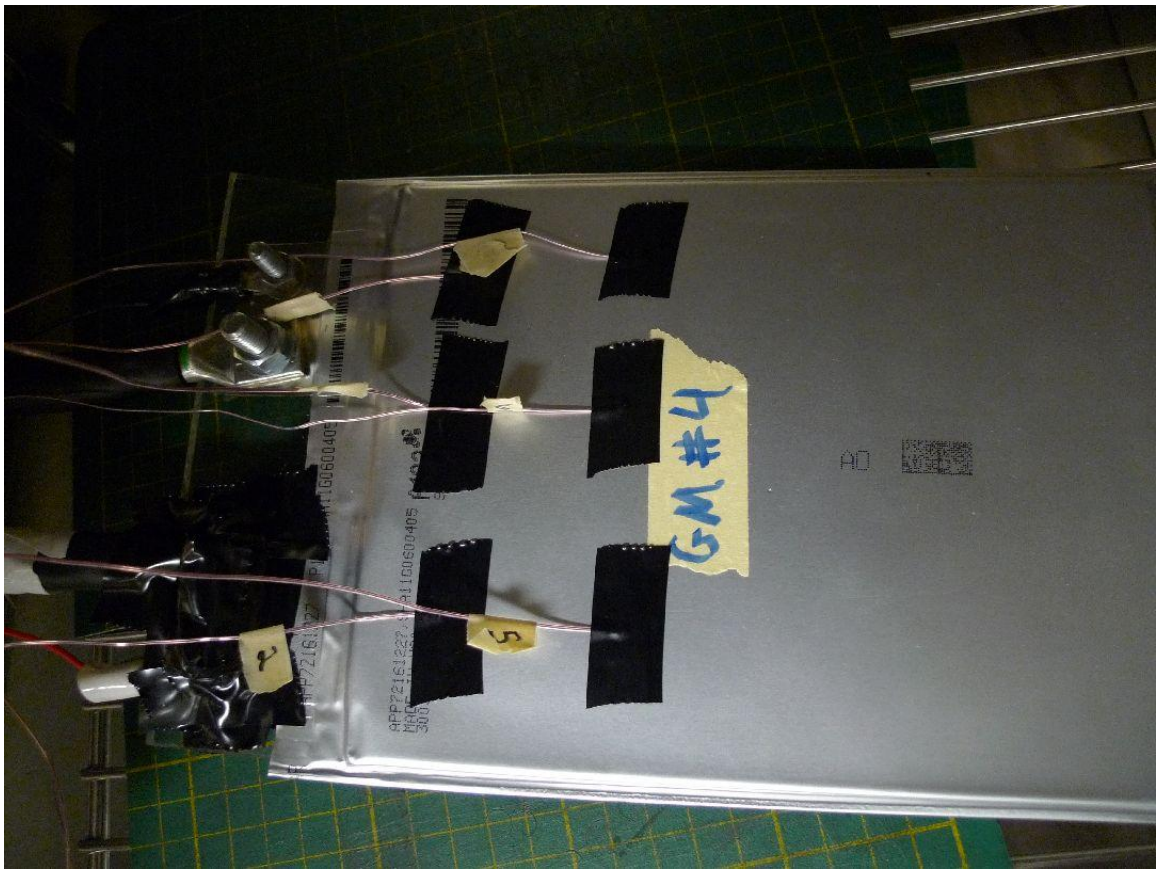

Figure 24 - Thermocouple arrangement on battery

4.3 Test Procedures

In order to elucidate the effects of temperature on battery performance, a defined set of battery tests are performed at the following temperatures: -20°C, -10°C, 0°C, 10°C, 25°C, 35°C, and 45°C. Data from constant current cycling and hybrid pulse power characterization (HPPC) tests provide data to parameterize the model, and three drive cycles (UDDS, HWFET, and US06) are used for validation.

4.3.1 Constant Current Cycling

One constant current cycle consists of a single charge to 100% SOC, followed by a discharge to 0% SOC. Charge events are performed using the constant-current, constant-voltage (CCCV) method. The battery is charged at the desired current until cell voltage reaches 3.60V, after which the battery is held at 3.60V until cell current falls to C/20. The battery is considered to have reached 100% SOC at this point. For the 20Ah cells used in this work, the cut-off current is 1A. Discharge events begin with a fully charged battery and end when cell voltage reaches 2.0V, at which point the battery is considered to have reached 0% SOC. There is no constant voltage step during discharge.

Constant current cycling was carried out at five different C-rates: C/5, C/2, 1C, 2C, and 5C, corresponding to currents of 4A, 10A, 20A, 40A, and 100A, respectively.

There is currently no universally accepted definition for cell capacity. In this work, cell capacity is taken to be a function of temperature and current, and is defined as the energy that can be discharged at a constant current after charging the battery using the CCCV method described above. Total internal resistance can also be observed from constant current cycling as a lumped value which includes ohmic, charge transfer, and diffusion effects.

4.3.2 Hybrid Pulse Power Characterization Test

The hybrid pulse power characterization (HPPC) is first described in a battery testing manual prepared by the Idaho National Laboratory [**50**] and is used in this work with minor modifications. The test begins by fully charging the battery using the CCCV charging method described above. The constant current portion is carried out at 20A and the constant voltage portion at 3.60V with a cut-off at 1A. After reaching 100% SOC, the battery is allowed to rest for 2 hours, and then it is discharged to 95% SOC at 20A. After another 2 hour rest, the battery is subjected to a 120A discharge pulse for 10 seconds, followed by a 40 second rest and a charge pulse at 120A for 10 seconds. The cycler is constrained to not allow battery voltages below 2V or above 3.6V. Immediately after the first set of high current pulses, the battery is discharged to 90% SOC, then rested for 2 hours and subjected to the high current pulses again. The pulse profiles are performed at the following SOCs: 95%, 90%, 85%, 75%, 65%, 55%, 45%, 35%, 25%, 15%, 10%, 5%. Finally, the battery is discharged at 20A until 2V is reached. The overall HPPC current profile is shown in Figure 25. A zoomed view of a single charge and discharge pulse event is shown in Figure 26.

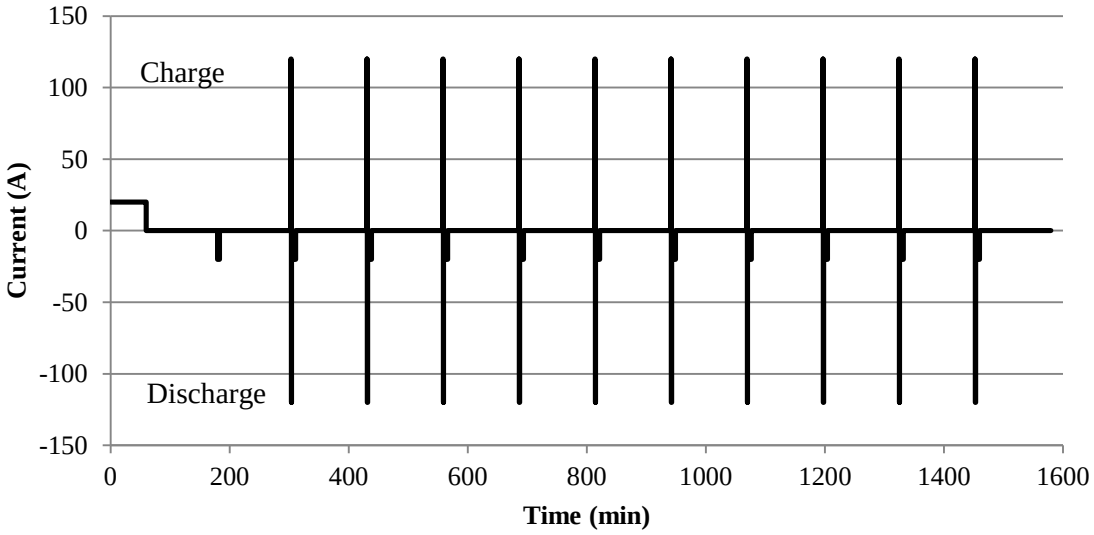

Figure 25 - Overall HPPC Current Profile

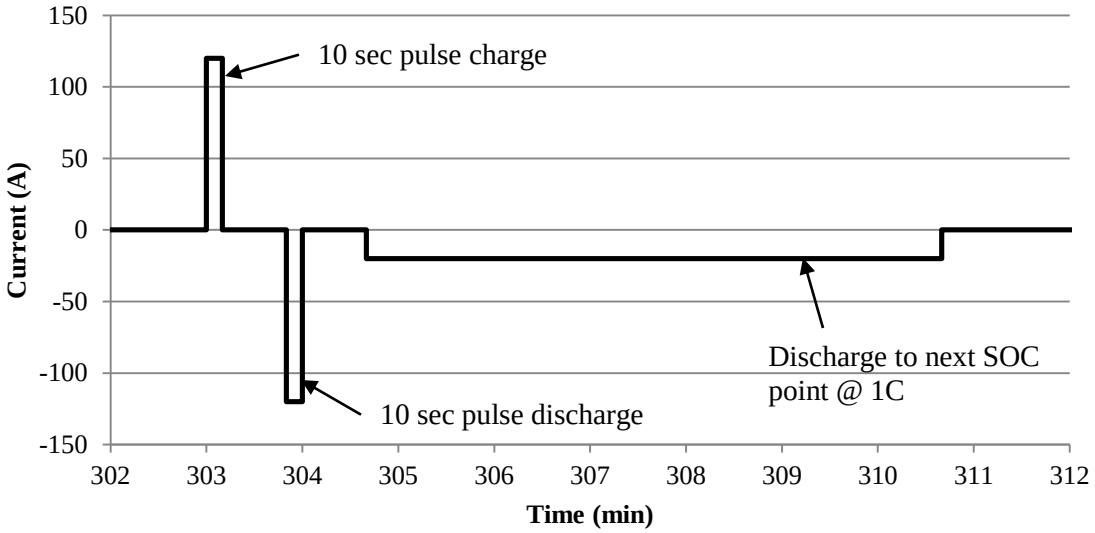

Figure 26 - HPPC Single Pulse Current Profile

The HPPC test is a highly informative procedure. For the purposes of parameterizing the simple battery model found in Autonomie, the HPPC test directly shows the maximum power that the battery is capable of delivering or receiving throughout its SOC range. Internal resistance as a function of SOC can also be obtained. For other equivalent circuit models, parameters for describing time variant behaviour such as diffusion effects can be obtained using techniques such as genetic algorithms [**51**] and particle swarm optimization [**52**].

4.3.3 Drive Cycles

Current profiles for the UDDS, HWFET, and US06 drive cycles were obtained through vehicle simulation in Autonomie and are shown in Figure 27, Figure 28, and Figure 29, respectively. The US06 cycle is much more demanding than the UDDS and HWFET, as expected from the aggressive nature of the US06 cycle. In some instances, the US06 cycle current demand momentarily exceeds the 120A capability of the Maccor battery cycler, so the experimental profile is clipped at 120A.

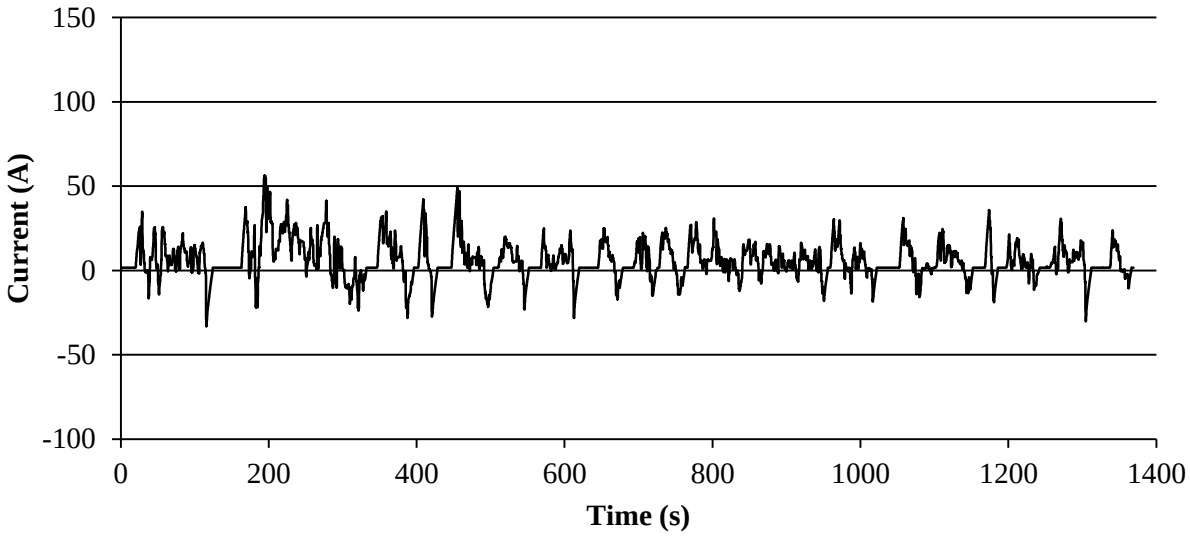

Figure 27 - Urban Dynamometer Driving Schedule current profile for single cell

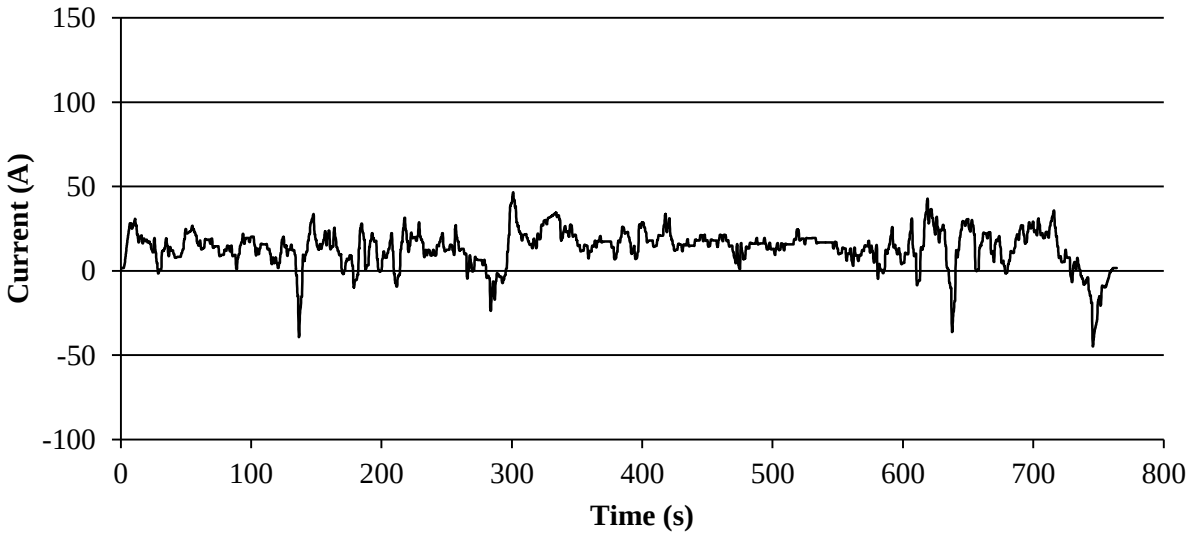

Figure 28 - Highway Fuel Economy Test current profile for single cell

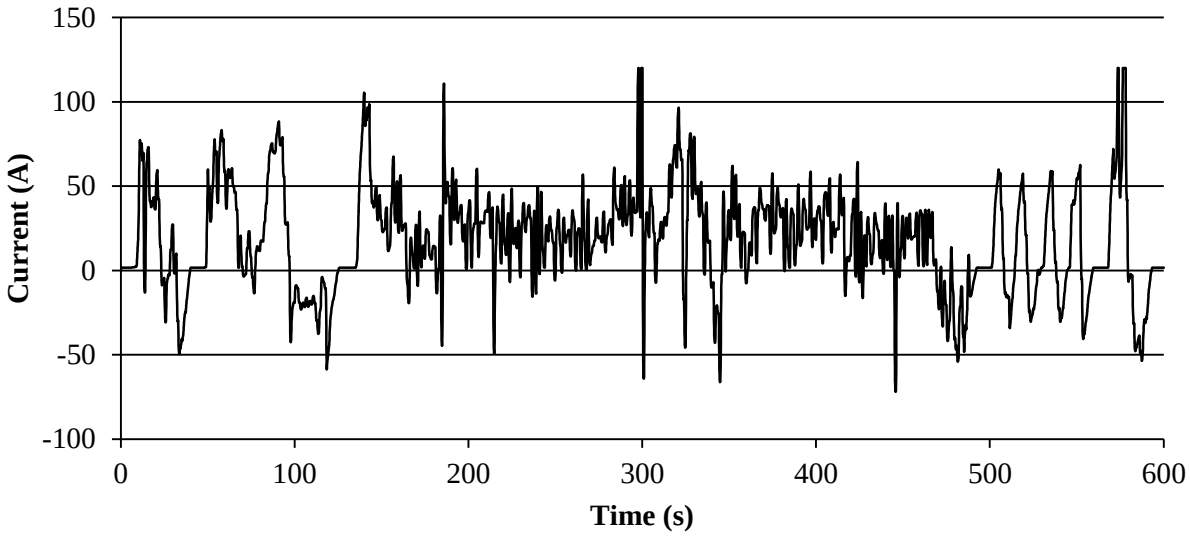

Figure 29 - US06 Drive Cycle current profile for single cell

The primary purpose of the drive cycle profiles is to validate the battery model parameterized from the constant current charge/discharge and HPPC data. Self-heating characteristics of battery may also be observed at a rudimentary level, but further experimentation will need to be performed to derive any thermal parameters for the cells. Such things are left for future works.

5 Battery Model

Battery state estimation plays an important role in the model-based design and operation of electrified vehicles. At the design stage, good voltage prediction helps estimate vehicle range, charge and discharge power capability (Wang et al. [**53**] refers to this as "state of power", or SOP), and powertrain efficiency. In operation, real-time estimation of battery SOC, state of health (SOH), and SOP are needed in order to intelligently manage the battery and optimize its efficiency and longevity. This work focuses on modeling the voltage response of li-ion batteries for model based design applications.

Broadly, there are two types of battery models. Physics-based electrochemical models describe the fundamental thermodynamics, intra-particle diffusion phenomena, and reaction kinetics that occur within the battery. Though highly detailed, these models are typically complex and require many parameters. Differential equations are often involved, leading to lengthy computation times and possible convergence issues which are ill suited for the accelerated nature of model based design. However, these fundamental electrochemical models are favoured in battery design applications, where the impact of any change in the cathode, anode, electrolyte, and separator properties need to be well understood.

Equivalent circuit models are the preferred method for predicting overall battery behaviour. These models utilize components such as resistors, capacitors, and voltage sources arranged in an electric circuit to mimic the voltage response of a battery, given a current profile. The parameters used by the physics-based models to describe the thermodynamic and electrochemical phenomena inside the battery are lumped as resistance and capacitance values.

The R_{int} model, depicted in Figure 30, is one of the simplest models and is used in Autonomie. Open circuit voltage, V_{OC}, is represented by an ideal voltage source. Total internal resistance for charging and discharging are given by R_{charge} and $R_{discharge}$ respectively. V_{batt} is the resultant battery potential. At a minimum, VOC, $R_{discharge}$, and R_{charge} are dependent on SOC. This work extends the model to also include the effects of temperature.

The R_{int} model can be parameterized directly from experimental data and is computationally very efficient since no differential equations need to be evaluated. However, it is unable to simulate transient or time-variant behaviour.

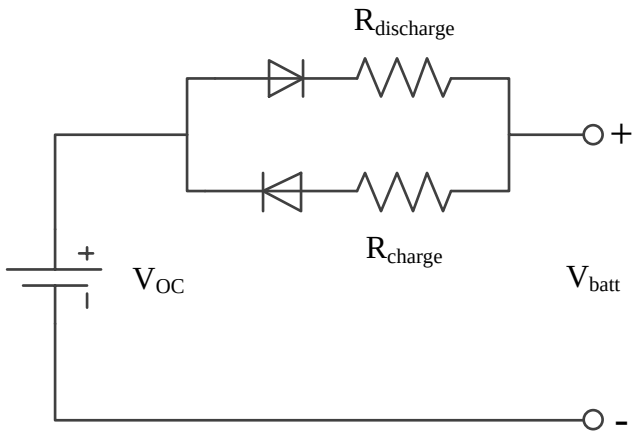

Figure 30 - Schematic diagram of R_{int} model used in Autonomie

The single RC circuit model, alternately known as the Thevenin, R-RC or first-order RC model, is shown in Figure 31. It improves upon the R_{int} model by adding a resistive-capacitive element. Total battery resistance is represented as a combination of charge transfer (R_{ct}), ohmic (R_{ohm}), and diffusion (C_{diff}) resistances. The capacitive element allows the model to emulate time dependent and transient behaviour.

In the R-RC model, it is not easy to determine the resistance and capacitance values directly from experimental data. Instead, parameter estimation methods such as genetic algorithms [**51**], multi-swarm particle swarm optimization [**52**], or least squares curve fitting [**54**] are employed to fit the model to experimental HPPC or similar data. Huria et al [**55**] suggest that this type of model is sufficient for most industrial applications. Hu [**52**] and He [**51**] compared many different equivalent circuit models and found that the R-RC model performs well despite its simplicity.

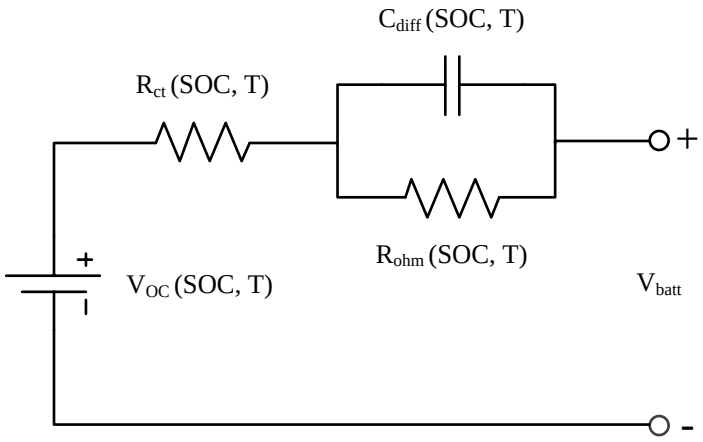

Figure 31 – Equivalent circuit diagram for the single RC battery model

The dual RC circuit model, also known as the dual polarization or second-order RC model, adds a second RC element to the single RC circuit model and is shown in Figure 32. The second RC element provides greater resolution of transient behaviour by separating activation polarization and concentration polarization effects [**51**]. Activation polarization refers to the voltage drop required to drive a chemical reaction, and concentration polarization refers to the voltage drop caused by the formation of concentration gradients within the battery.

Parameterizing the dual RC model is similar to the single RC model – the same parameter estimation algorithms can be used, but computational cost will be higher due to the additional variables. The dual RC model has been found to be slightly more accurate than the single RC model, and both are suitable for system level battery modeling [**51**] [**52**] [**55**]. Higher order RC models are possible, but are typically not employed because the extra computational cost is not worth the marginal increase in fidelity.

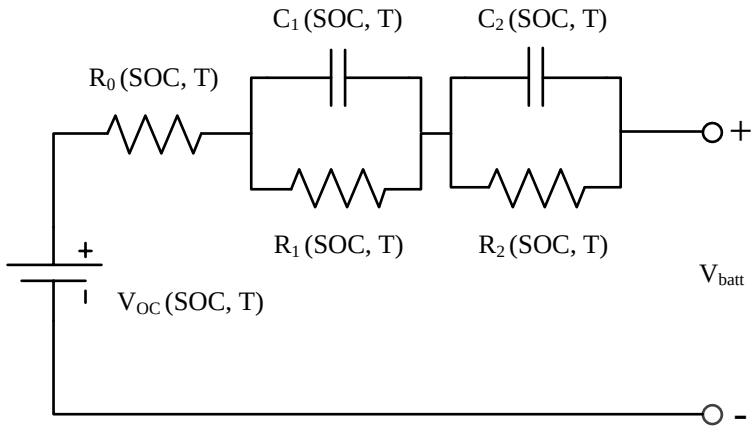

Figure 32 - Equivalent circuit diagram for the dual RC battery model

6 Vehicle Model

In order to approximate a battery current profile for a drive cycle, a vehicle model is required. Many PHEV architectures are possible, and the choice of architecture and powertrain components will impact the current profile generated. This work draws upon the author's involvement in University of Waterloo Alternative Fuel Team's (UWAFT) vehicle architecture and component selection process in order to obtain a vehicle model of maximum fidelity. Through UWAFT, manufacturer-supplied vehicle and component data is available, allowing for a well parameterized vehicle model that does not require many assumptions to be made. Additionally, opportunities for model validation and further refinement are expected within one or two years as UWAFT integrates the PHEV powertrain.

6.1 Baseline Vehicle

The EcoCAR2 competition utilizes the 2013 Chevrolet Malibu as the base vehicle. It is a mid-size sedan powered by a 2.4 litre gasoline engine producing 169 horsepower.

6.2 Proposed Architectures

Three vehicle architectures were identified for consideration: A fuel cell PHEV, a parallel through the road PHEV, and an all-wheel drive (AWD) series PHEV. For each architecture, major powertrain components were specified and manufacturer data used to parameterize a vehicle model where information was available. Default models were otherwise used. Each architecture was evaluated based on a number of criteria including all-electric range, fuel economy, acceleration time, vehicle weight, overall greenhouse gas emissions. In order to make a final decision, factors unrelated to vehicle performance were also considered, such as the availability and cost of components; and the internal objectives of the team.

6.2.1 Fuel Cell PHEV

Instead of an internal combustion engine, the fuel cell PHEV architecture uses a proton exchange membrane (PEM) fuel cell. Gaseous hydrogen is fed into the fuel cell, where it is converted into electrical energy and used to meet the vehicle load. Fuel cells are inherently more efficient than combustion engines, and since the fuel cell directly outputs electricity, the architecture does not incur the additional efficiency loss of converting mechanical energy to electrical energy of an engine-generator system. UWAFT's past experience with fuel cells has shown that the efficiency curve of a fuel cell is fairly flat over a wide power range, so the fuel cell is well suited to automotive applications where a wide range of operation is necessary. One of the major drawbacks of the fuel cell architecture is the large size of the hydrogen storage tanks and often limited vehicle range.

The structure of the Autonomie model used to evaluate this powertrain is shown in Figure 33. The major powertrain components are listed in Table 3.

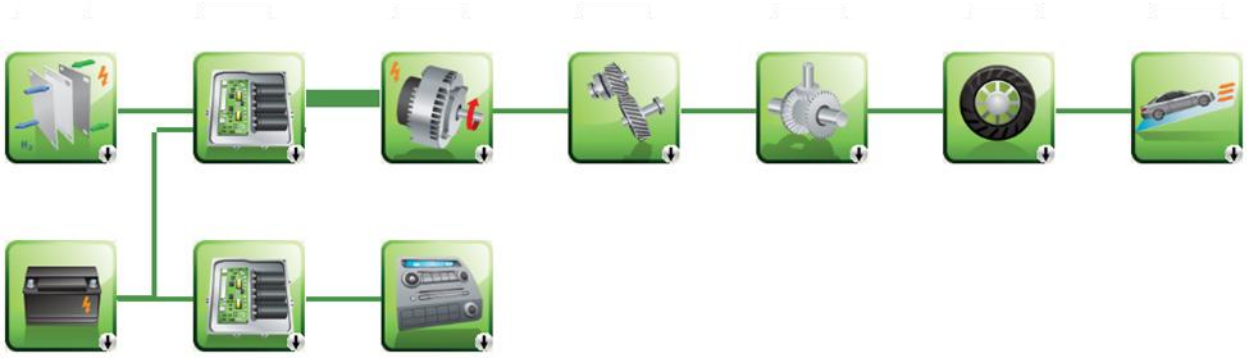

Figure 33 - Autonomie model structure for a fuel cell PHEV architecture

Table 3 - Major powertrain components for proposed fuel cell PHEV architecture

Component	Vendor	Details
Fuel Cell	Hydrogenics	66kW peak
Motor	UQM	145kW peak
Transmission	Borg Warner	Gear ratio of 7.17 between motor and wheel
Battery	A123	19.7 kWh @ 346V

6.2.2 Parallel Through the Road PHEV

The parallel through the road PHEV concept utilized an E85 compatible engine to drive the front wheels and an electric motor to drive the rear wheels. No direct connection between the engine and the battery exists, so the only way to charge the battery during vehicle operation is to apply a negative torque at the rear motor while the engine is driving the vehicle forward. The rear motor is thus resists the forward pull of the engine and translating that effort into electrical energy for the battery. The greatest strength of this architecture is in its simplicity and relatively few additional components, which allows for a lightweight design. Vehicle power output is also high due to having both an engine and an electric motor. However, energy transfer from the engine to the battery is inefficient, and available power is significantly reduced during all electric operation.

The structure of the Autonomie model used to evaluate this powertrain is shown in Figure 34. The major powertrain components are listed in Table 4.

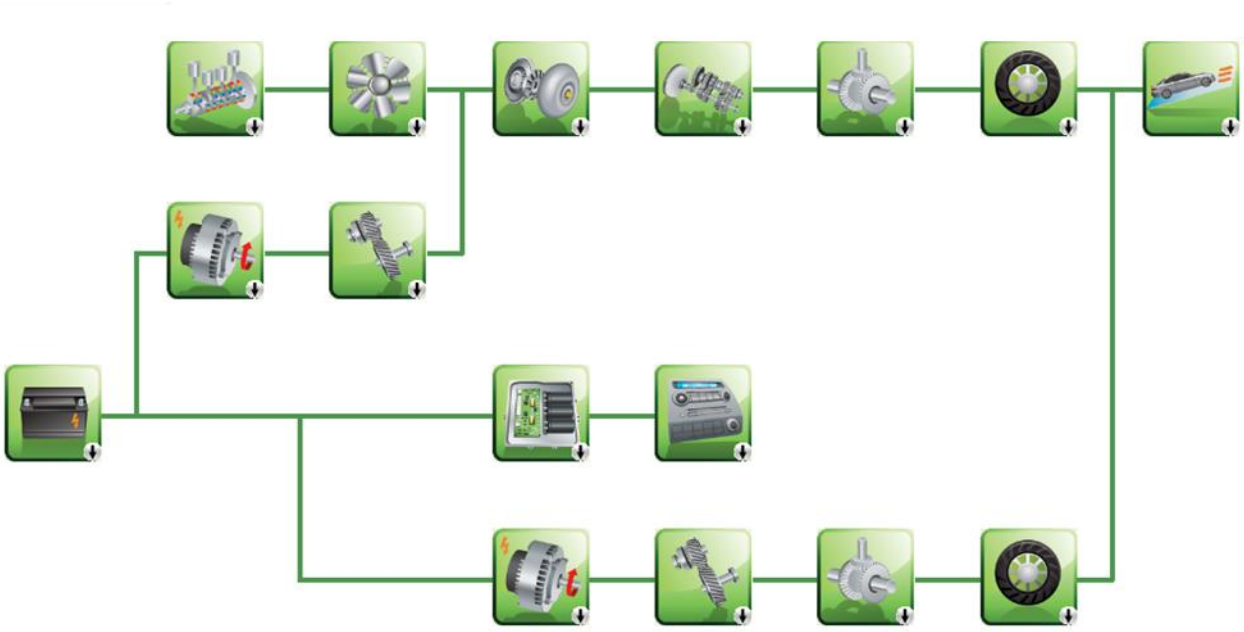

Figure 34 - Autonomie model structure for a PTTR PHEV architecture

Table 4 - Major powertrain components for proposed parallel through the road PHEV architecture

Component	Vendor	Details
Engine	GM	2.4L, E85 compatible
Front Transmission	GM	Stock transmission
Rear Transmission	Borg Warner	Gear ratio of 8.76 between motor and wheel
Battery	A123	19.7 kWh @ 346V
Motor	TM4	103 kW peak

6.2.3 All-wheel Drive Series PHEV

Two electric traction motors are utilized in this architecture – one drives the front axle and the other drives the rear axle. In a series architecture, there is no mechanical connection between the engine and the wheels, so a generator is required to translate the engine's mechanical energy output to electrical energy for the traction motors. The decoupling of the engine from the wheels allows the engine to always be operated in its most efficient point of operations, and the two traction motors enables innovation in torque splitting strategies and controls development. The disadvantage of this architecture is the additional weight, cost, size, and controls complexity of having two motors and a generator.

A simplified Autonomie model was used to evaluate this architecture, shown in Figure 35. There was no prebuilt model for a series architecture utilizing two motors, so a single motor model was used and the power scaled accordingly. Since both motors are identical, the simplification should not have a significant impact on model fidelity. The major powertrain components are described in Table 5.

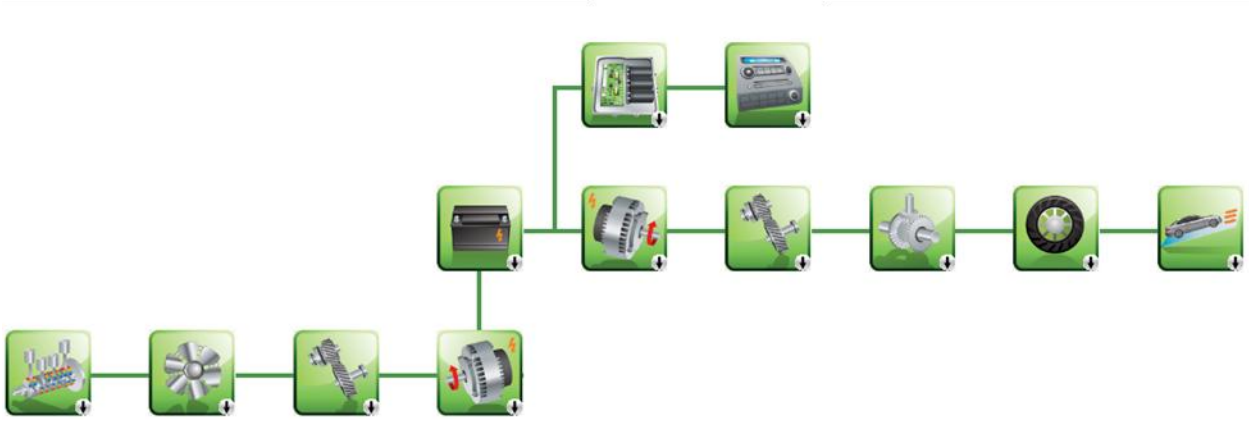

Figure 35 - Simplified Autonomie model structure for E85 AWD PHEV architecture

Table 5 - Major powertrain components for proposed AWD series PHEV architecture

Component	Vendor	Details
Engine	GM	2.4L, E85 compatible
Generator	TM4	103 kW peak power
Battery	A123	19.7 kWh @ 346V
Front Motor	TM4	103 kW peak
Rear Motor	TM4	103 kW peak
Front Transmission	Borg Warner	Gear ratio of 8.76 between motor and wheel
Rear Transmission	Borg Warner	Gear ratio of 8.76 between motor and wheel

6.3 Architecture Comparison

Simulations were carried out for the baseline vehicle and the three proposed architectures. Comparisons were made between the dynamic performance; vehicle weight; fuel and energy consumption; petroleum energy use; and greenhouse gas emission of each vehicle. The results of the simulations are shown in Table 6

Table 6 - Vehicle Technical Specifications for stock and proposed vehicle architectures

VTS Specification	Production 2013 Malibu	E85 Series PHEV, AWD	Parallel Through the Road with BAS	Fuel Cell PHEV
Acceleration 0-60 mph	8.2s	7.1s	6.4s	7.7s
Acceleration 50-70 mph	8.0s	4s	3.1s	4.4s
Vehicle Top Speed	N/A	140 km h^{-1}	>140 km h^{-1}	137.9 km h^{-1}
Vehicle Weight	<2250 kg	2075 kg	1915 kg	2038 kg
Steady State Power for 3.5% Grade	N/A	34.3 kW	32.9 kW	33.9 kW
Charge-Depleting Range	N/A	55 km	68.8 km	64 km
Charge-Depleting Fuel Consumption	N/A	0 L 100^{-1} km^{-1}	0 L 100^{-1} km^{-1}	0 kg 100^{-1} km^{-1}
Charge-Sustaining Fuel Consumption	N/A	11.9 L E85 100^{-1} km^{-1}	11.6 L E85 100^{-1} km^{-1}	1.33 kg H_2 100^{-1} km^{-1}
UF-Weighted Fuel Energy Consumption	787 Wh.km^{-1} [8.83lge 100^{-1} km^{-1}]	321 Wh.km^{-1} [3.6 lge 100^{-1} km^{-1}]	242 Wh.km^{-1} [2.6 lge 100^{-1} km^{-1}]	170 Wh.km^{-1} [1.9 lge 100^{-1} km^{-1}]
UF-Weighted AC Electric Energy Consumption	N/A	132 Wh km^{-1}	139 Wh km^{-1}	160 Wh km^{-1}
UF-Weighted Total Energy Consumption	787 Wh km^{-1}	453 Wh km^{-1}	402 Wh km^{-1}	330 Wh km^{-1}
UF-Weighted WTW Petroleum Energy Use	774 Wh km^{-1}	106 Wh km^{-1}	81 Wh km^{-1}	7.1 Wh km^{-1}
UF-Weighted WTW GHG Emissions	253 g km^{-1}	169.3 g km^{-1}	153 g km^{-1}	170 g km^{-1}

lge = litres of gasoline equivalent (by energy)

The three proposed architectures are all more powerful and more energy efficient than the stock vehicle. However, some of the benefit of the increased efficiency is offset by the additional mass from the battery and electric motors. The proposed architectures also displace a significant amount of well-to-wheel (WTW) petroleum usage and greenhouse gas emissions. One trade-off that was made was to improve acceleration at the cost of vehicle top speed.

The fuel cell PHEV architecture is the most energy efficient due to the high efficiency of the fuel cell, UQM motor, and having fewer energy conversions. Fuel cells inherently have zero emissions, so it is also the least polluting of all at the tailpipe. It is the slowest of the three options, but is still quicker to accelerate than the production Malibu. Although this architecture has very low petroleum energy usage, it has high ‘wheel to well’ (WTW) greenhouse gas (GHG) emissions due to the processes involved with manufacturing hydrogen. Competition rules assume that hydrogen is produced using a coal-dominant power mix which is mostly characteristic of the

United States. Hydrogen production in Canada through electrolysis would yield substantially less GHG emissions due to its clean power mix.

The parallel through the road PHEV architecture is the quickest to accelerate of the three due to its light weight and direct mechanical linkage between the engine and wheel. The same reasons also results in better fuel economy; and lower petroleum energy use and greenhouse gas emissions. However, its power is limited in all-electric operation due to the single, 103kW motor available for traction.

The all-wheel drive series PHEV is heavy and has the highest fuel consumption. It has more regenerative braking than the parallel through the road architecture due to the presence of an electric motor at the front as well as the back. The potential for regenerative braking is greater at the front of the vehicle because vehicle weight is shifted towards the front during a deceleration event. Petroleum energy use is high in the series architecture, and greenhouse gas emissions are on par with the fuel cell architecture.

In addition to the quantitative simulation results, a number of qualitative factors also influenced vehicle architecture selection, including the cost and availability of fuel and components, potential for post-competition uses for the vehicle, and UWAFT's experience with the architecture. A comparison of the three proposed architectures is shown in Table 7

Table 7 - Qualitative factors for selecting vehicle architecture

	Favourability		
Qualitative Factors	**Fuel Cell**	**PTTR**	**AWD Series**
Component cost	Med	Low	High
Component availability	Med	High	High
Fuel availability	Low	Med	Med
Post-competition potential for research	High	Low	High
Post-competition potential as team vehicle	Low	High	High
Team technical experience	High	Low	Low

The fuel cell architecture is attractive because UWAFT has worked with fuel cells extensively in the past, and the vehicle would become a fertile platform for research in its post-competition life.

However, complex maintenance and low availability of fuel would not allow the vehicle to be used as an every-day team vehicle.

In contrast, the parallel through the road architecture is relatively simple to build and maintain economically. The engine would be capable of accepting regular gasoline as well as E85 and would make an excellent general purpose team vehicle. However, UWAFT has had little recent experience dealing with combustion engines the architecture yields limited research opportunities.

The series architecture is costly, but the resultant vehicle becomes both a usable team vehicle and a rich platform upon which research can be conducted. Research interests in the vehicle include battery SOC management, torque splitting algorithms, and vehicle control strategies.

6.4 Selected architecture and refined model setup

The AWD series PHEV architecture was selected as the final vehicle architecture for its propensity for software and control strategy optimization and post-competition usefulness as a team vehicle and as a research platform. Component availability was also a key factor. Once the architecture selection was finalized, a greater amount of component became available from manufacturers and the Autonomie model was refined.

Autonomie does not group components into subsystems, but the vehicle may be better understood if separated into four sections:

1. The Engine / Generator System, which converts fuel energy to electrical energy;
2. The A123 battery, which manages the high voltage bus voltage. It interfaces with all other subsystems;
3. The 12V System converts electricity from the high voltage bus to 12V and supplies the vehicle accessories with power; and,

4. The Motor / Traction System converts electrical energy into mechanical energy to propel the vehicle.

The Autonomie powertrain model for the baseline vehicle is shown in Figure 36, followed by a description of each model component.

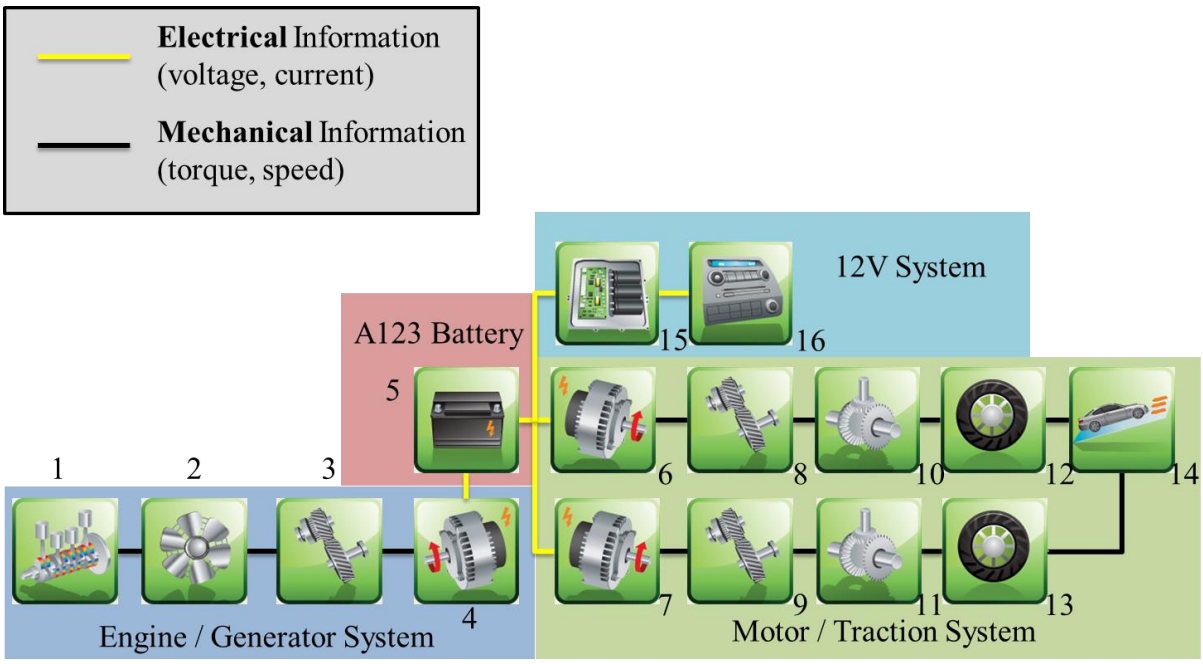

Figure 36 - Autonomie model layout for UWAFT's proposed E85 PHEV Chevrolet Malibu

1. **Engine** – The General Motors LE9 is a Flex-Fuel engine capable of running on gasoline containing up to 85% ethanol. It has a peak power of 130kW (175hp). Efficiency maps and other model parameters were provided by General Motors.

2. **Mechanical Accessory** – Typically, accessories directly driven by the engine such as alternators and A/C compressors are represented here and subtracted from the engine output power. In this PHEV architecture, 12V power comes instead from the high voltage battery, and the A/C compressor will be electric, so there are no losses from mechanical

accessories.

3. **Torque Coupling** – The engine is most efficient at high torque and medium speeds (2800 rpm to 4000 rpm), while the generator is most efficient at moderate torque and high speeds (6000 rpm to 9000 rpm). A gear ratio of 1:2.3 was thus chosen to achieve good overlap of the engine and generator's high efficiency regions.

4. **Generator** – To convert the mechanical energy from the engine to electrical energy that can be used by the motors and battery, a 105kW generator from TM4 is used. The generator is identical to the front and rear motors, but operated in reverse.

5. **High Voltage Battery** – The main electrochemical energy storage device is a 19.7 kWh, 346V battery pack containing A123 Systems prismatic $LiFePO_4$ cells. By default, Autonomie uses the R_{int} type model described in Section 5. The selection of the A123 Cells was based principally on component availability, and the sizing of the battery pack will be discussed below in Section 6.5.

6. **Motor (Front)** – The vehicle's tractive power is delivered by two permanent magnet motors from TM4, each rated at 105kW. The motors have a maximum speed of 11500 rpm. Inverter losses were accounted for in the data provided by TM4, so they did not need to be modeled separately.

7. **Motor (Rear)** – The rear motor is identical to the front motor

8. **Torque Coupling (Front)** – Conventional vehicles use multi-speed gearboxes to maximize the performance and engine operating efficiency, but since electric motors are much more efficient then ICEs over their entire operating range, a single speed gearbox typically suffices. A GKN eAxle unit, which contains the single fixed gear reduction as well as a differential, connects the front motor to the front axle and has a combined gear ratio of 7.47:1.

9. **Torque Coupling (Rear)** – The GKN eTransmission unit chosen to couple the rear motor to the axle via a fixed 9.59:1 gear ratio and, like the eAxle, includes a differential. The eTransmission also includes a park lock system (PLS).

10. **Final Drive (Front)** – The gear ratio and losses associated with a differential or other final drive may be modeled separately from the transmission or fixed gear reduction, but since the data available for the GKN eAxle and eTransmission units already account for losses from the differential, the final drive model does not simulate any losses.

11. **Final Drive (Rear)** – See Final Drive (Front)

12. **Wheel (Front)** – The Chevrolet Malibu comes with 17" wheels and is modeled using Autonomie's model for 235-55R17 tires.

13. **Wheel (Rear)** – See Wheel (Front).

14. **Chassis** – The vehicle is estimated to weight approximately 2075kg, with a 50/50 weight distribution.

15. **DC/DC Converter** – 12V power is supplied from the high voltage electrical bus, so a DC/DC converter is required to bridge the two voltages. This component had not been selected at the time of vehicle modeling, so an overall efficiency of 90% was assumed.

16. **Electrical Accessories** – Based on prior experience within UWAFT, the average load of the 12V system was estimated to be 1.5kW.

6.5 Battery Pack Sizing

One of the key components of the vehicle powertrain is the battery pack. The capacity of the on board battery pack has a significant impact on the all-electric range and fuel economy of the vehicle. If the vehicle control strategy does not allow the engine or fuel cell to be used during all electric operation, the size of the battery pack will also affect the acceleration of the vehicle.

EcoCAR2 teams were presented with four possible configurations for their battery packs, which are summarized in Table 8.

Table 8 - Comparison of battery pack configuration options

Config.	Cells in series (per module)	Parallel strings (per module)	Number of modules	Total # of cells	Nominal Voltage (V)	Nominal Capacity (kWh)
6x15s2p	15	2	6	180	297	11.3
7x15s2p	15	2	7	210	346	13.2
6x15s3p	15	3	6	270	297	16.9
7x15s3p	15	3	7	315	346	19.7

A greater store of electrical energy is expected to improve the all-electric range and fuel economy of the vehicle. Parametric studies were performed on each of the vehicles to see the effects of battery pack configuration on fuel economy and all-electric (or charge depleting) range.

The fuel consumption and charge depleting range for an E85 AWD PHEV is shown in Figure 37. All-electric ranges vary from 33.7km to 55.7km and fuel consumption varies from 7.4L 100^{-1} km^{-1} (5.2lge 100^{-1} km^{-1}) to 5.3L 100^{-1} km^{-1} (3.7lge 100^{-1} km^{-1}), respectively. Litres gasoline equivalent (lge) is a unit used when comparing the consumption rate of fuels with different energy densities. For EcoCAR2, E85 and gasoline are considered to have a volumetric energy density of 6.265kWh L^{-1} and 8.895kWh L^{-1}, respectively. Thus, the energy of 1L of E85 may be expressed as 0.7043lge.

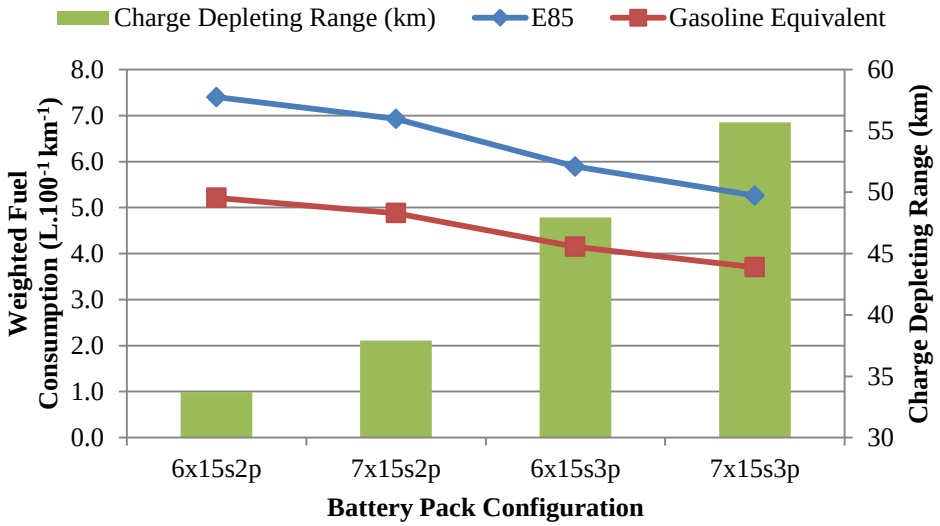

Figure 37 - Weighted fuel consumption and all-electric range of an E85 AWD PHEV as battery pack configuration is varied

The fuel consumption and charge depleting range for an E85 PTTR PHEV is shown in Figure 38. All-electric ranges vary from 38.27km to 68.84km and fuel consumption varies from 5.90L 100^{-1} km^{-1} (4.15lge 100^{-1} km^{-1}) to 3.86L 100^{-1} km^{-1} (2.72lge $100^{-1}km^{-1}$), respectively.

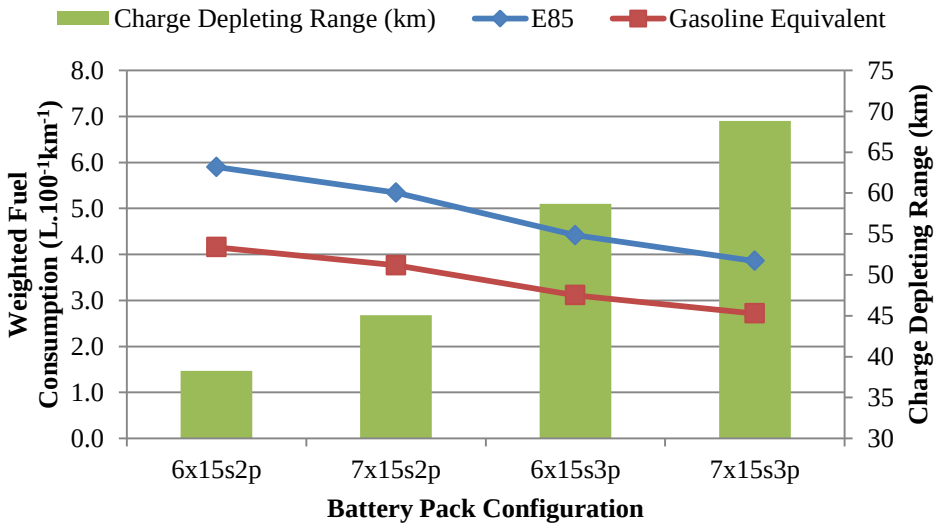

Figure 38 - Weighted fuel consumption and all-electric range of an E85 PTTR PHEV as battery pack configuration is varied

The fuel consumption and charge depleting range for a Fuel Cell PHEV is shown in Figure 39. All-electric ranges vary from 36.5km to 64.1km and fuel consumption varies from 0.75kg $100^{-1}km^{-1}$ (2.81lge $100^{-1}km^{-1}$) to 0.51kg $100^{-1}km^{-1}$ (1.91lge $100^{-1}km^{-1}$), respectively.

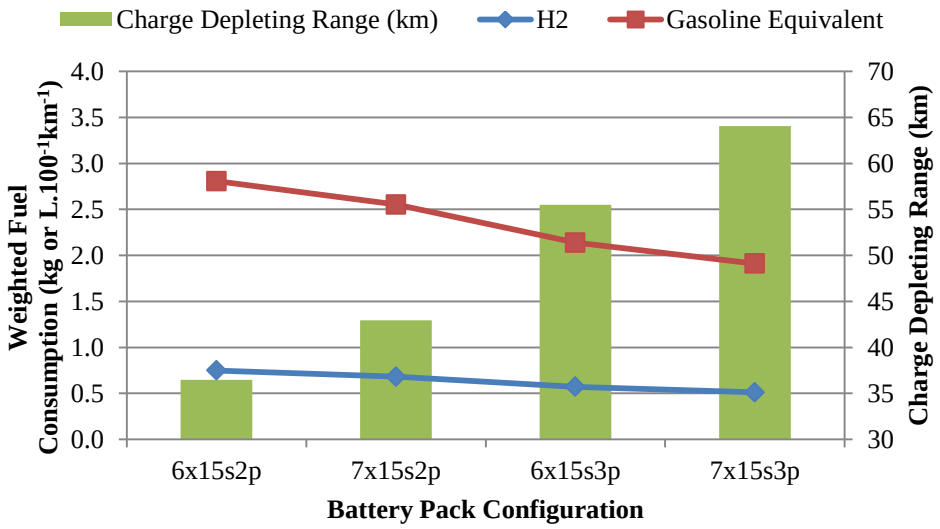

Figure 39 - Weighted fuel consumption and all-electric range of an Fuel Cell PHEV as battery pack configuration is varied

In all cases, the higher capacity battery pack configurations result in a significantly longer all-electric range and a lower fuel consumption. From a fuel consumption and consumer acceptability perspective, choosing the largest battery pack available is the clear choice.

Selecting a large battery pack is also advantageous because of its higher continuous power output. The vehicle with a larger battery pack is more competent in hill climbing and towing situations. However, a larger battery pack will generate comparatively more heat. A cooling system that can move the heat away from the battery pack is therefore required. The solution devised by UWAFT is to use liquid cooled plates on the sides of the battery modules [**56**]. The concept is illustrated in Figure 40.

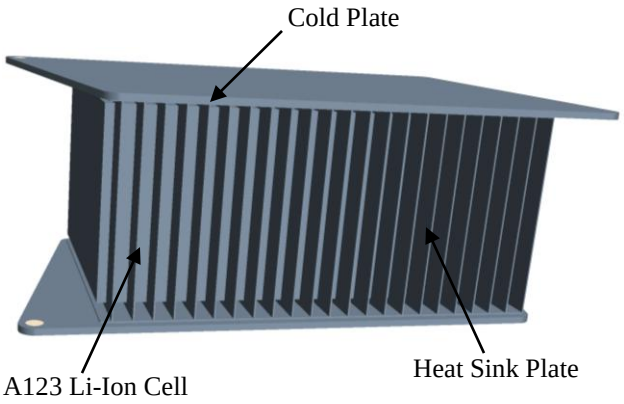

Figure 40 - Battery module cooling system [56**]**

CFD simulations were carried out to estimate the temperature rise of the battery module under a worst-cast scenario consisting of the following:

- 120A continuous current draw;
- Battery internal resistance for 15% SOC; and
- Inlet coolant temperature of 40°C

The steady-state temperature distribution for four stacked modules are shown in Figure 41. Even under a very demanding scenario, the maximum temperature reached at any point was 48.0°C. Since temperature did not exceed the maximum allowable operating temperature of 50°C, confidence is high that the cooling system will be adequate under all vehicle operating conditions.

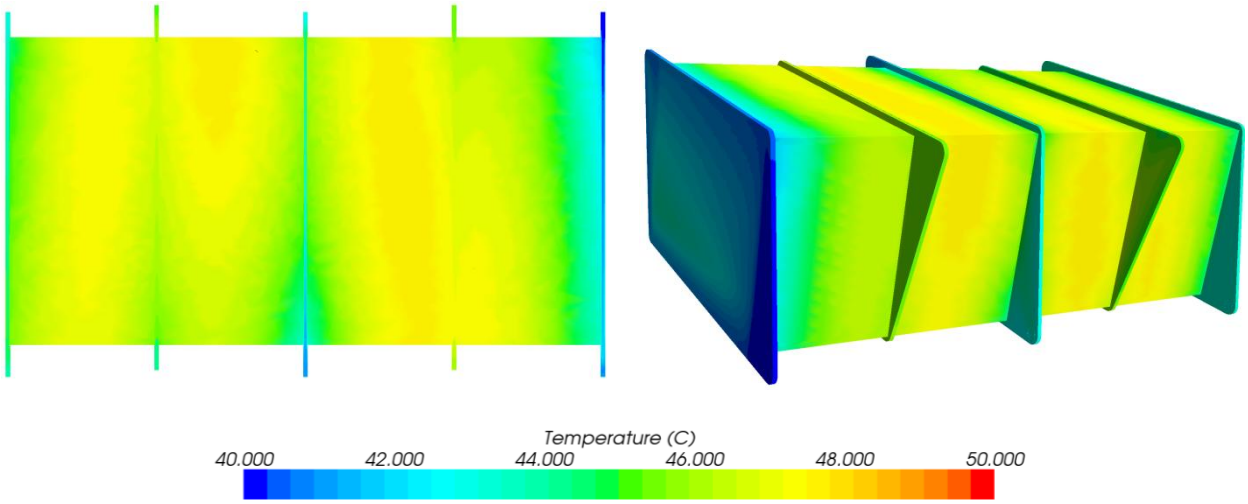

Figure 41 - Surface temperature distribution under maximum continuous current draw (120A) [56**]**

7 Analysis and Discussion

7.1 Capacity

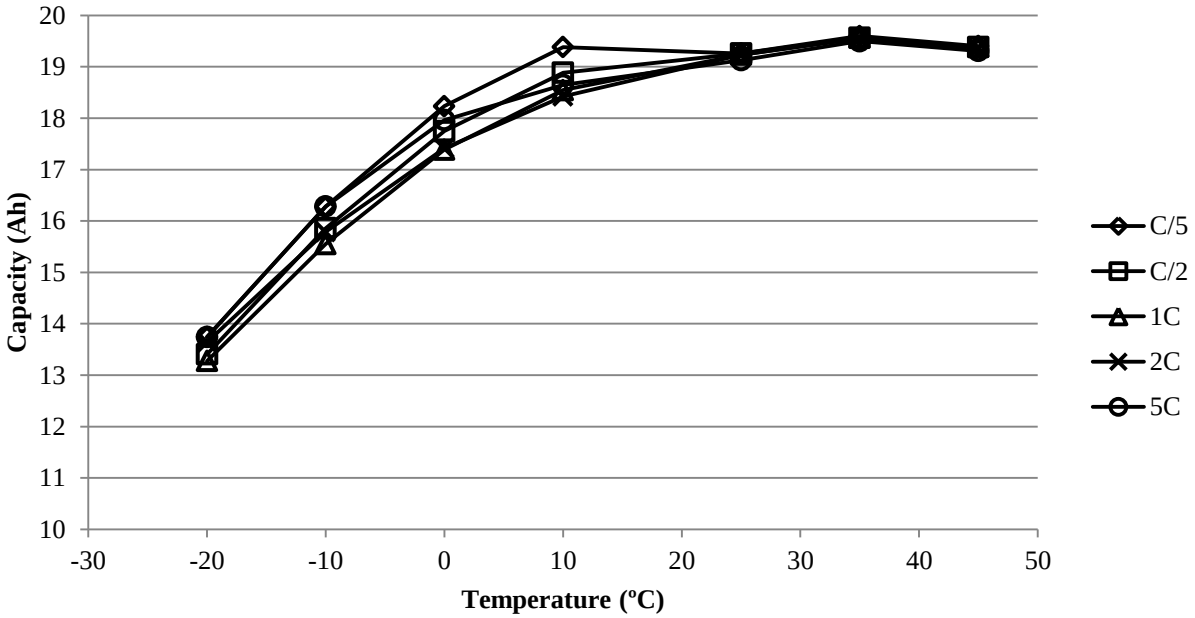

Figure 42 - Battery capacity at various discharge rates and temperatures. Data is shown for a single cell as collected experimentally described in the earlier section.

Battery capacity as a function of temperature for five different current rates is given in Figure 42. At room temperatures and above, capacity is unaffected by both temperature and discharge rate. The capacity of the battery at room temperature, 19.234Ah, may be taken as the total capacity of the battery. The apparent capacity of the battery changes significantly at temperatures of 10°C and below. At -20°C, the apparent capacity of the battery is only 70% of its total capacity. At temperatures of 10°C and below, higher discharge rates should also slightly reduce apparent capacity, although this trend is obscured by self-heating of the battery. At lower temperatures, high current rates cause the battery temperature to rise due to self-heating and the apparent capacity increases. It is for this reason that the 2C and 5C capacities at low temperature are higher than the 1C capacities.

The capacities obtained using a 1C discharge rate was chosen to represent battery capacity in the model. For numerical values used in the vehicle model for cell capacity, refer to Table A1.

7.2 Open Circuit Voltage

At each temperature, V_{OC} was determined from HPPC data for the following SOC: 0%, 5%, 10%, 15%, 25%, 35%, 45%, 55%, 65%, 75%, 85%, 90%, 95%, 100%. SOC is scaled to the 1C discharge capacity discussed in Section 7.1. The resultant V_{OC} curves are shown in Figure 43. Expectedly, the curves are very flat at moderate SOCs, with sharp increases and decreases at very high and very low SOCs, respectively. As temperature decreases, the sharp changes in V_{OC} are less pronounced, most likely because during capacity determination, the increased internal resistance at low temperatures caused the test to reach its end condition before the electrodes reached their extreme states of lithiation or de-lithiation. A low-current test method would be able to better characterize V_{OC} behaviour in the extreme SOC ranges, especially at low temperatures, but would result in lengthier experiments. Fortunately, hybrid vehicles operate at moderate SOCs, so rigorous investigation of the battery's extreme SOC behaviour is not critical for this work.

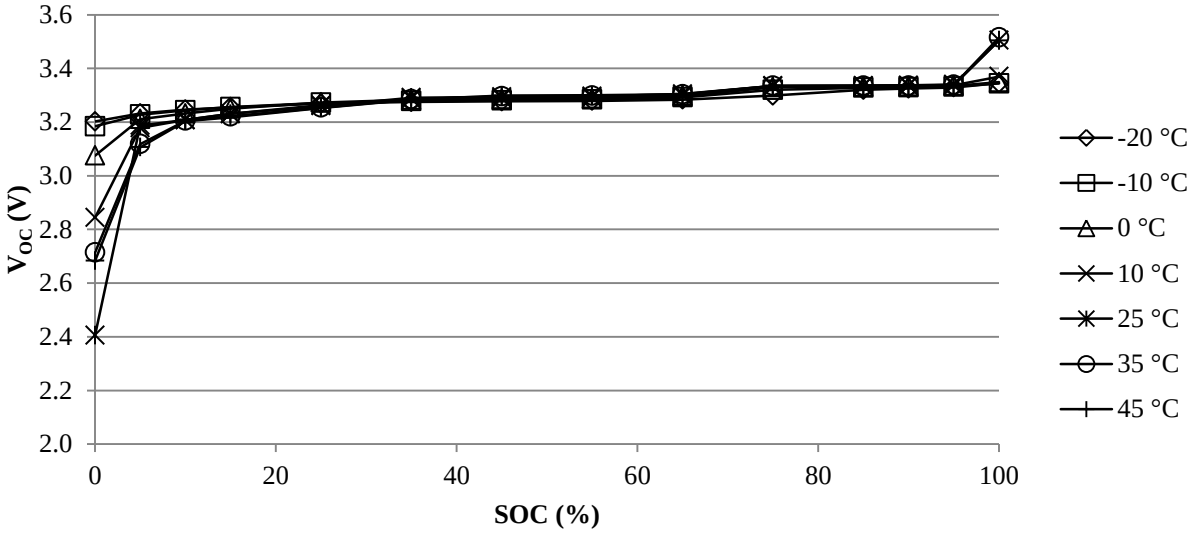

Figure 43 - Open circuit voltage curves for temperatures from -20ºC to 45ºC

At moderate SOCs, V_{OC} is very similar across all temperatures and exhibits a small amount of dependence on temperature. As seen in Figure 44 and Figure 44, V_{OC} rises slightly with temperature; the difference between V_{OC} at -20°C and 45°C is about 20mV.

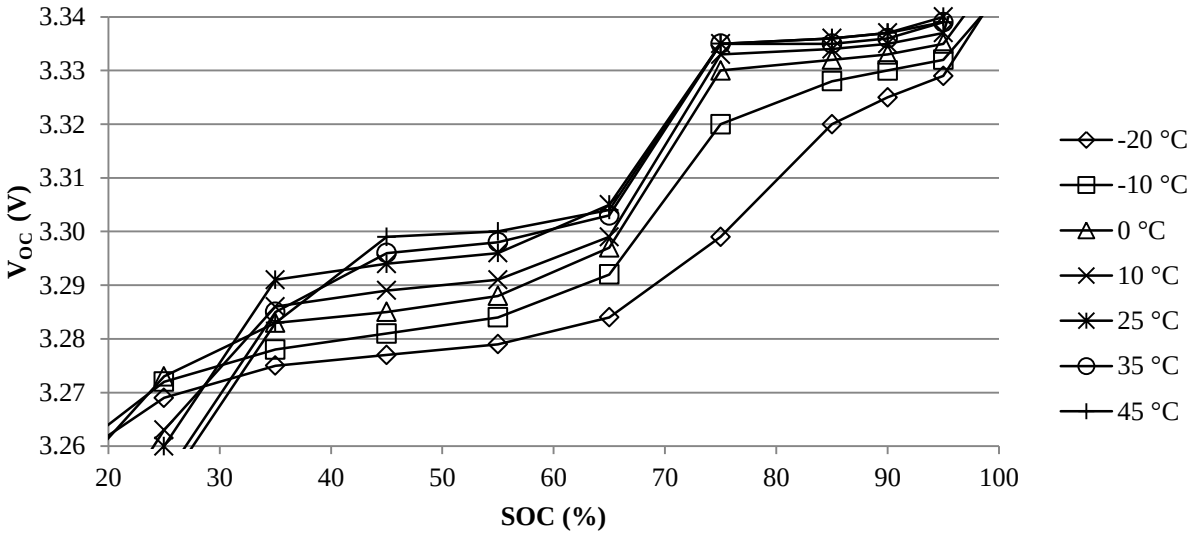

Figure 44 – Close-up of open circuit voltage curves from 20% to 100% SOC

The numerical values for the VOC lookup tables used in the vehicle model are shown in Table A2.

7.3 Internal Resistance

The battery model only considers internal resistance to be a function of temperature, SOC, and whether the battery is being charged or discharged, so it is incapable of accounting for any path dependent phenomena. However, voltage response, and therefore the apparent internal resistance of the battery, is strongly path dependent. Choosing a representative value for internal resistance is critical for model accuracy.

Internal resistance is determined from constant current cycling or HPPC data using Equation 1 and Equation 2.

$$R_{dis} * I = (V_{OC} - V) \quad \text{Equation 1}$$

$$R_{chg} * I = (V - V_{OC}) \quad \text{Equation 2}$$

where R_{dis} , R_{chg} is the discharge and charge resistance of the battery, respectively

V_{OC} is the open circuit voltage of the battery;

V is the measured battery voltage; and,

I is the measured battery current.

7.3.1 Constant Current Resistance

Calculated internal resistances derived from constant current discharging and charging are shown in Figure 45 and Figure 46, respectively. Each plot represents the resistances found at one current rate for different temperatures and SOCs.

For the cell under study, discharge resistances are lowest at high SOC, rises slightly through the middle SOC range, and increases sharply at low SOC. The rate of discharge also impacts the observed internal resistance. For high current discharge cycles at low temperature, internal resistance appears to first decrease, then increase again as the battery empties. This is likely due

to the self-heating of the battery during cycling. As the battery heats due to internal losses, internal resistance is depressed through the moderate SOC range and rises again due to the diffusion and mass transfer effects characteristic of the low SOC region.

Charge resistances are lowest at low SOC, does not change significantly throughout the moderate SOC range, and rises sharply at high SOC. At low temperatures, an increase in internal resistance is observed at a lower SOC, but the self-heating effects seen during the low temperature discharge profiles are not observed. This is likely because the constant voltage portion of the charge profile is reached earlier at low temperatures, so the high currents required to generate significant amounts of heat cannot be sustained.

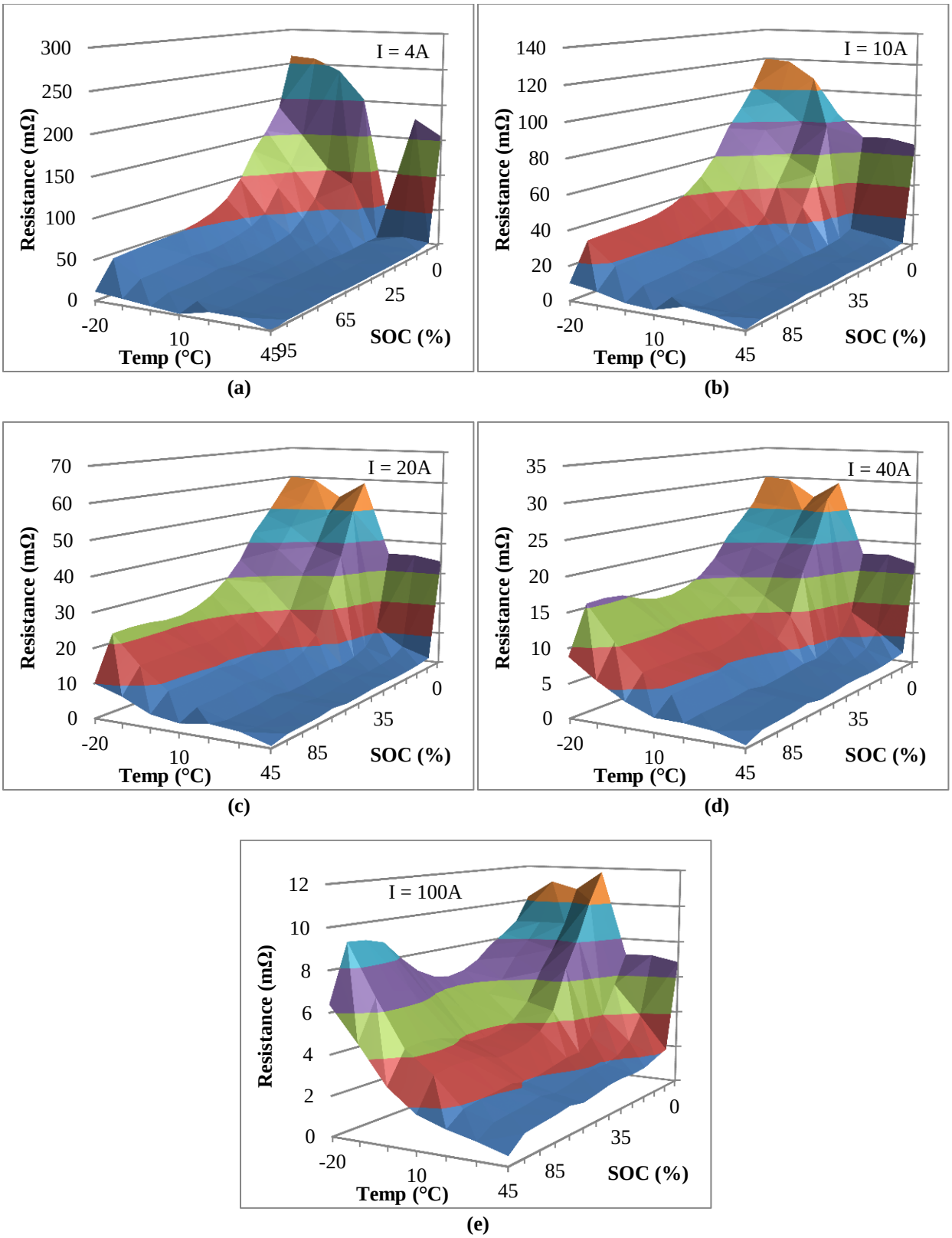

Figure 45 – Constant current discharge resistances as a function of SOC and ambient temperature for C rates of (a) C/5 (4A); (b) C/2 (10A); (c) C/1 (20A); (d) 2C (40A); (e) 5C (100A)

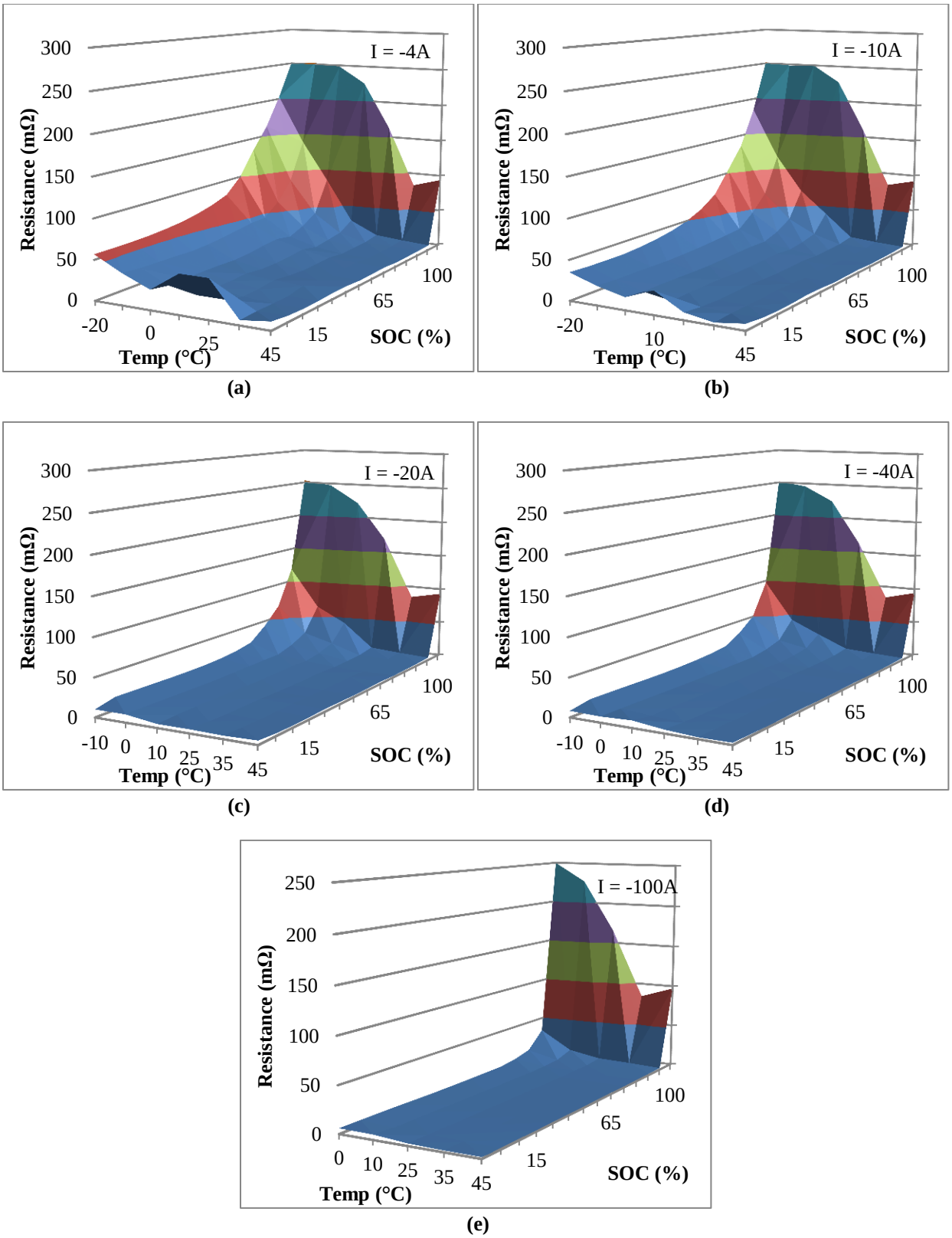

Figure 46 – Constant current charge resistances as a function of SOC and ambient temperature for C rates of (a) C/5 (4A); (b) C/2 (10A); (c) C/1 (20A); (d) 2C (40A); (e) 5C (100A)

7.3.2 HPPC

The discharge and charge resistances calculated from HPPC data are shown in Figure 47 and Figure 48, respectively. Consistent with the results obtained from constant current cycling, temperature and SOC are observed to strongly influence internal resistance. Resistance values derived from HPPC data is significantly lower than the resistance values found using constant current data.

Discharge resistance is highest at low temperatures and low SOC. Since pulses were not performed at 0% and 100% SOC, no resistance values are available at these extremes. Resistances are only known for SOCs between 5% and 95%. For the purposes of vehicle modeling, battery resistance at 0% and 100% SOC are assumed to be the same as the resistances at 5% and 95% SOC, respectively. This will not have a significant impact on model accuracy since the internal resistance at 100% and 95% SOC are expected to be similar, and the vehicle will never operate below 5% SOC. Numerical values for the HPPC-derived discharge resistances used in the vehicle model is given in Table A3.

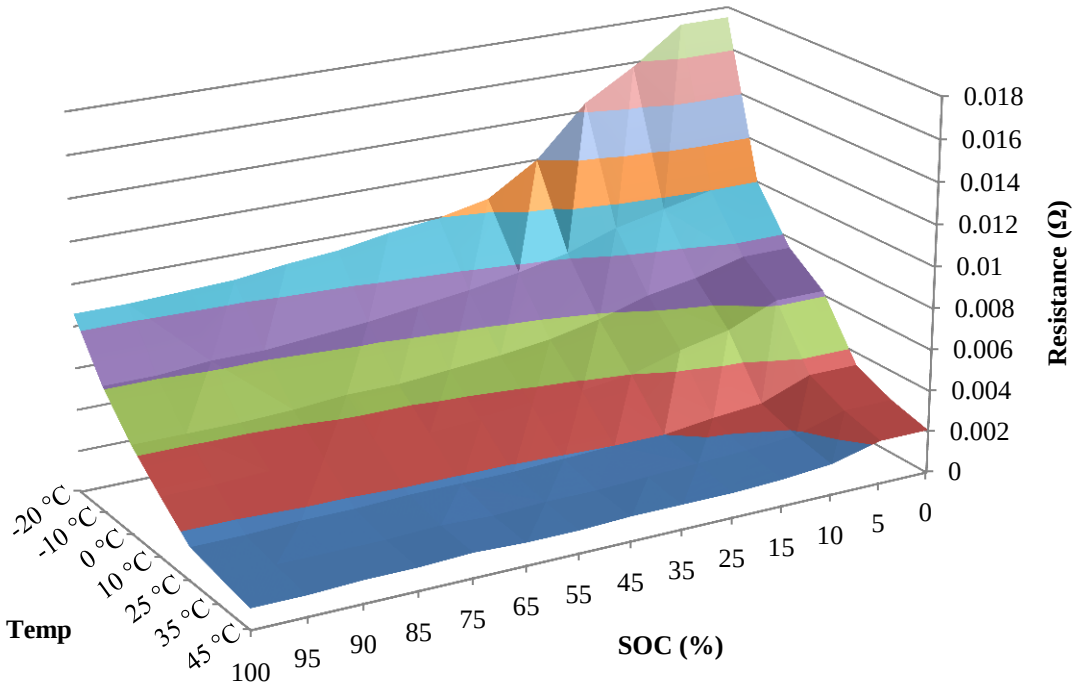

Figure 47 - Discharge resistances obtained from HPPC testing for various temperatures

Using the HPPC method, charge resistance is observed to be mainly a function of temperature. Internal resistance increases non-linearly with temperature. At low temperatures, internal resistance also increases slightly with SOC. In contrast with the constant current based results, no sharp increase in internal resistance is observed at high SOCs. Again, no data is available for 0% and 100% SOC, so they are assumed to be the same as the resistances at 5% and 95% SOC, respectively. Numerical values for the HPPC-derived charge resistances used for vehicle simulation is given in Table A4.

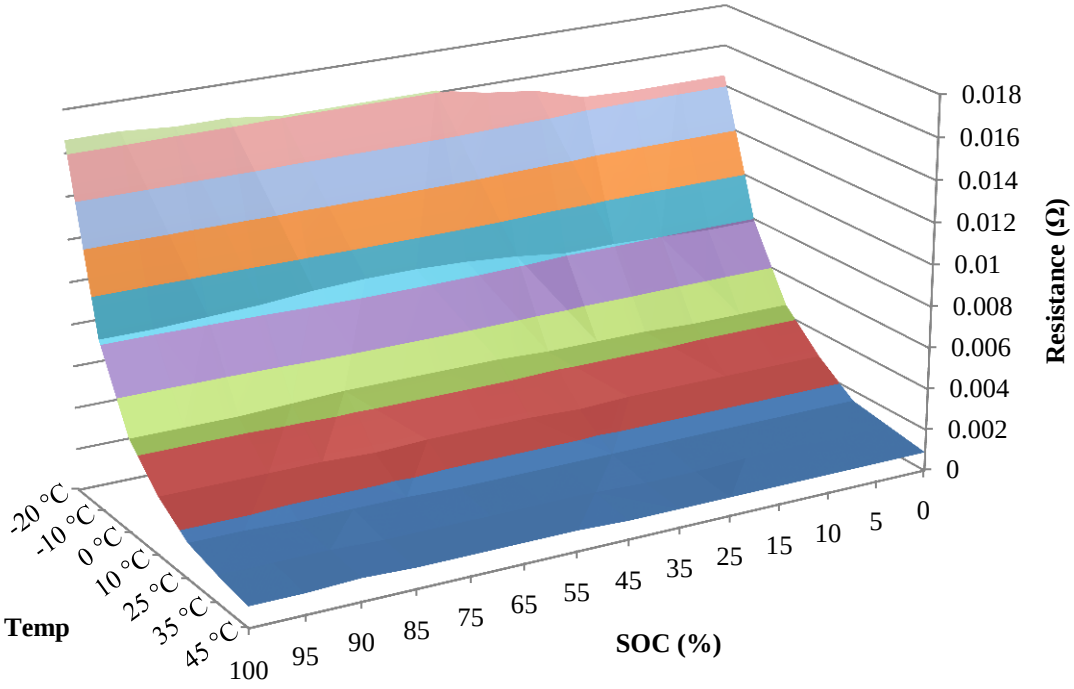

Figure 48 - Charge resistances obtained from HPPC testing for various temperatures

7.4 Power Capacity

Using HPPC data, the maximum power that can be charged to or discharged from the battery is determined for SOCs ranging from 5% to 95% and temperatures ranging from -20°C to 45°C. The maximum power is defined as the power that can be applied to the battery without violating some predetermined voltage limits. For this work, a lower limit of 2.0V and an upper limit of 3.6V were chosen in order to remain consistent with other tests. In practice, maximum allowable power may be less due to design considerations such as battery longevity and operational voltages of other system components connected to the battery.

Because of the time-variant and non-linear resistance characteristics of a battery at current, power capacity should be given for a specified length of time. Thus, maximum power is properly expressed as the maximum power that may be sustained for a length of time. Since the dynamic nature of a vehicle causes the battery to switch between charging and discharging events fairly often, the maximum power that could be delivered for 10 seconds was found, as prescribed by the HPPC test procedure. Since high power events such as acceleration to highway speed typically takes less than 10 seconds, this is an appropriate duration..

Due to the limitations of the Maccor cycler, the maximum 10-second discharge power could only be observed for SOC values between 5% and 25% at -20°C. For charging, the maximum 10-second power was observable for temperatures of 10°C and below. Predictably, discharge performance is poorest at low SOC and low temperatures, and charge performance is poorest at high SOC and low temperature. It is expected that discharge performance would be best at high SOC and high temperatures, and charge performance would be best at low SOC and high temperature.

Although charge resistances are generally lower than discharge resistances (refer to Section 7.3.2), the low minimum allowable voltage used in the HPPC test method results in a greater discharge power capacity than charge power capacity for the cases where the true maximum power could be observed.

Since equipment limitations precluded direct observation of maximum charge and discharge powers at the higher temperatures, these values were estimated using the HPPC-derived resistances. The maximum allowable 10-second charge power and discharge power at each SOC and temperature was found using Equation 3 and Equation 4, respectively.

$$P_{T,SOC}^{chg,max} = \frac{3.6 - V_{OC(T,SOC)}}{R_{T,SOC}^{chg}} * 3.6 \qquad \text{Equation 3}$$

$$P_{T,SOC}^{dis,max} = \frac{2.0 + V_{OC(T,SOC)}}{R_{T,SOC}^{dis}} * 2.0 \qquad \text{Equation 4}$$

where $P_{T,SOC}^{chg,max}$ is the maximum 10-second charge power for some T and SOC, in W

$P_{T,SOC}^{dis,max}$ is the maximum 10-second discharge power for some T and SOC, in W

$V_{OC(T,SOC)}$ is the battery open circuit voltage at some T and SOC, in V

$R_{T,SOC}^{chg}$ is the charge resistance at the end of a 10 second HPPC charge pulse at some T and SOC, in Ω

$R_{T,SOC}^{dis}$ is the discharge resistance at the end of a 10 second HPPC charge pulse at some T and SOC, in Ω

The resultant power capability for discharging and charging are shown in Table 9 and Table 10, respectively.

Table 9 - Experimental results for maximum 10-second Discharge Power, Watts

		Temperature, °C						
		-20°C	-10°C	0°C	10°C	25°C	35°C	45°C
SOC (%)	5%	*140.6*	*243.5*	*277.4*	*291.7*	*325.3*	*337.1*	*342.1*
	10%	*157.9*	*253.2*	*288.4*	*310.2*	*348.5*	*357.6*	*363.0*
	15%	*173.9*	*260.6*	*296.0*	*320.3*	*354.1*	*362.3*	*367.2*
	25%	*211.4*	*274.2*	*309.2*	*333.3*	*361.1*	*368.1*	*372.3*
	35%	*241.6*	*283.2*	*317.0*	*341.4*	*366.1*	*372.6*	*376.3*
	45%	*248.9*	*289.2*	*321.7*	*344.7*	*368.1*	*374.8*	*378.7*
	55%	*254.0*	*294.0*	*325.3*	*347.4*	*369.5*	*375.8*	*379.8*
	65%	*259.9*	*298.4*	*328.8*	*350.0*	*370.9*	*377.1*	*381.0*
	75%	*265.4*	*304.6*	*333.5*	*354.3*	*374.1*	*380.0*	*383.6*
	85%	*271.7*	*308.0*	*335.9*	*356.2*	*375.3*	*381.1*	*384.6*
	90%	*273.8*	*309.4*	*337.5*	*357.1*	*376.1*	*381.7*	*385.2*
	95%	*275.8*	*311.6*	*338.7*	*358.5*	*377.0*	*382.4*	*385.9*

* Shaded values indicate that battery cycler limit of 120A was reached. Actual maximum power is higher

Table 10 - Experimental results for maximum 10-second Charge Power, Watts

		Temperature, °C						
		-20°C	-10°C	0°C	10°C	25°C	35°C	45°C
SOC (%)	5%	*-79.9*	*-162.9*	*-314.3*	*-422.3*	*-398.1*	*-392.5*	*-387.6*
	10%	*-77.5*	*-154.2*	*-293.3*	*-425.7*	*-408.1*	*-402.7*	*-399.6*
	15%	*-76.2*	*-148.1*	*-276.7*	*-427.7*	*-409.4*	*-404.0*	*-400.5*
	25%	*-74.1*	*-137.4*	*-253.0*	*-431.0*	*-413.3*	*-407.9*	*-404.7*
	35%	*-72.5*	*-133.3*	*-243.6*	*-411.7*	*-416.1*	*-410.9*	*-407.7*
	45%	*-72.1*	*-132.8*	*-242.2*	*-405.2*	*-417.1*	*-412.2*	*-409.6*
	55%	*-71.8*	*-132.6*	*-240.8*	*-403.7*	*-417.4*	*-412.3*	*-409.6*
	65%	*-72.9*	*-131.7*	*-236.2*	*-396.2*	*-417.8*	*-412.8*	*-409.9*
	75%	*-71.0*	*-124.5*	*-213.8*	*-349.9*	*-421.7*	*-416.5*	*-413.6*
	85%	*-68.9*	*-121.9*	*-212.7*	*-344.6*	*-422.0*	*-416.9*	*-413.9*
	90%	*-68.4*	*-121.7*	*-215.0*	*-343.6*	*-422.1*	*-417.0*	*-413.9*
	95%	*-67.4*	*-122.4*	*-214.4*	*-341.4*	*-422.4*	*-417.3*	*-414.2*

* Shaded values indicate that battery cycler limit of 120A was reached. Actual maximum power is higher

Within the context of EcoCAR2 and the vehicle model used in this work, an additional constraint must be considered. Teams were instructed to adhere to a maximum 10-second rate of 10C as a safety restriction. Including this additional design constraint, the final maximum discharge and charge powers used in the model are shown in Figure 49 and Figure 50, respectively.

Power capacity is inversely related to battery internal resistance, and so the shape of the power capacity surfaces will be reminiscent of the internal resistance surfaces in Section 7.3.2. For discharge, the lowest power capacity is at low temperature and SOC and the highest power capacity is at high temperature and SOC. For charging, power capacity is lowest at low temperatures, and highest at high temperatures.

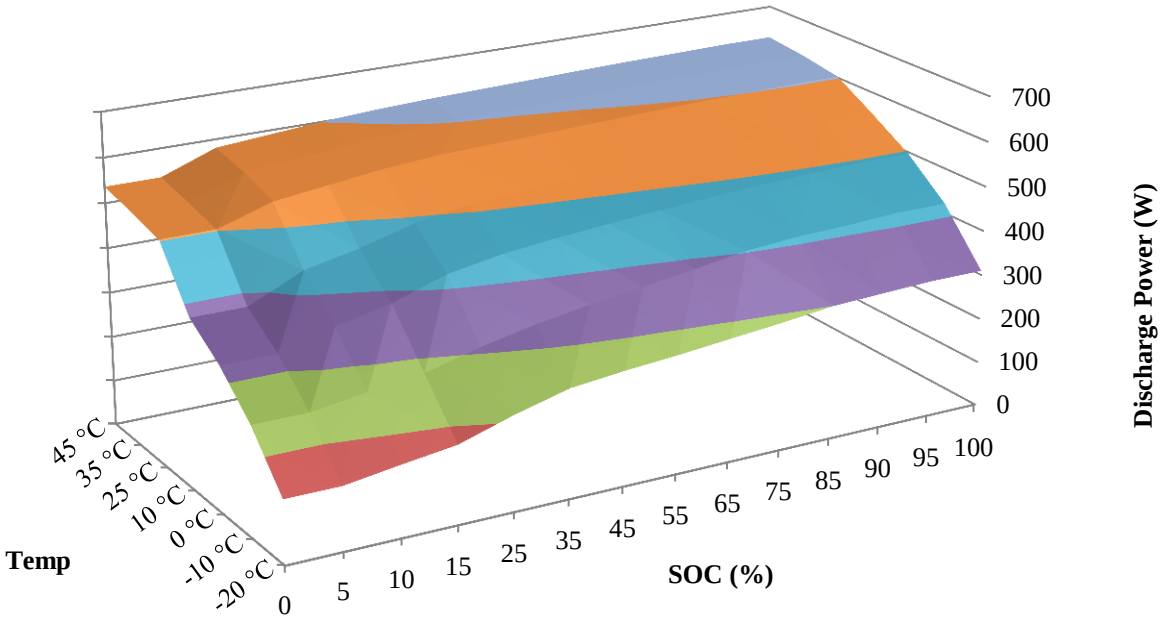

Figure 49- Estimated maximum allowable 10-second discharge power used for vehicle modeling

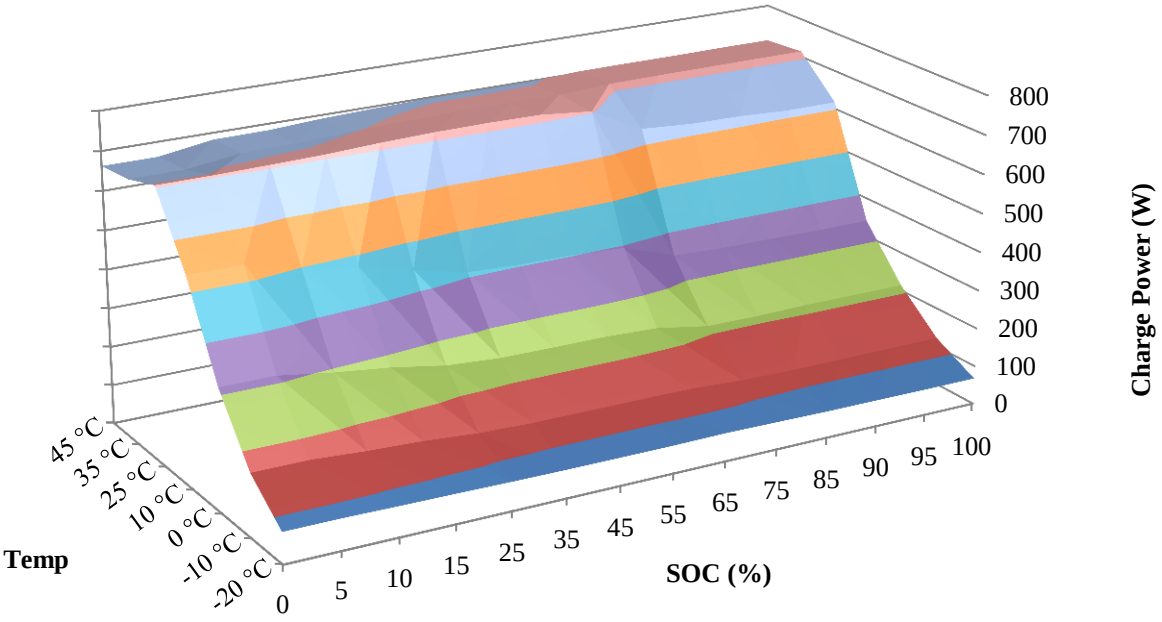

Figure 50 - Estimated maximum allowable 10-second charge power used for vehicle modeling

7.5 Self-Heating

Internal battery resistance results in the generation of heat, which raises the temperature of the battery above ambient conditions. Although the battery was instrumented with thermocouples, one side of the thermocouple was always exposed to ambient conditions. As such, the data collected is useful for making qualitative observations only. Conducting any quantitative thermal analyses on these batteries will require data from more elaborate test apparatus such as a calorimeter or adiabatic jig (both beyond the scope of this work). Detailed thermal analysis of the battery would be desirable for further improving the battery model and simulating thermal loads. The impact of battery self-heating, and the energy requirements for heating or cooling the battery could be simulated.

7.5.1 Constant Current Discharge

Battery surface temperature for constant current discharge profiles are shown in Figure 51. Data is shown for ambient temperatures ranging from -20°C to 45°C and for current rates of C/5, C/2, 1C, 2C, and 5C. Self-heating is most significant at low temperatures and high current rates, which is consistent with the higher internal resistances observed at low temperatures.

At low temperatures, the rate of self-heating is quick at the beginning, slows during the middle SOC range, and accelerates again at the end. As expected, as the internal battery temperature rises, internal resistance decreases. Lower internal resistance reduces heat generation, so the battery temperature does not rise as quickly during the middle SOC region. Finally, as the interior of the cell warm higher current densities are permitted which result in acceleration of the overall heating of the cell.

At higher temperatures, battery temperature rises more linearly, which is consistent with the observation that discharge resistance is not sensitive to temperature or SOC at elevated temperatures.

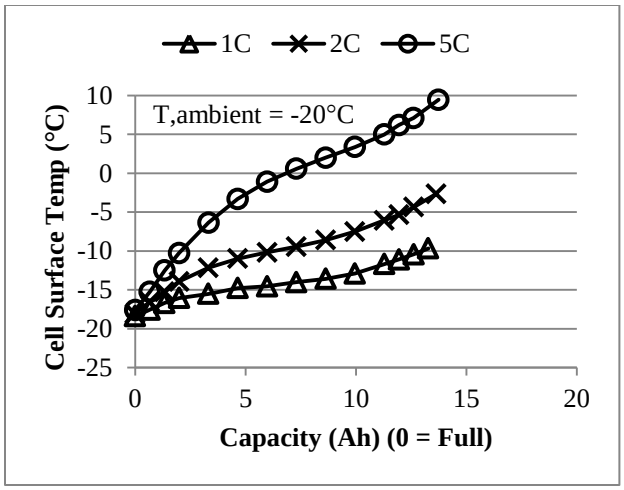
1C
2C
5C
T,ambient = -20°C
Cell Surface Temp (°C)
Capacity (Ah) (0 = Full)

(a)

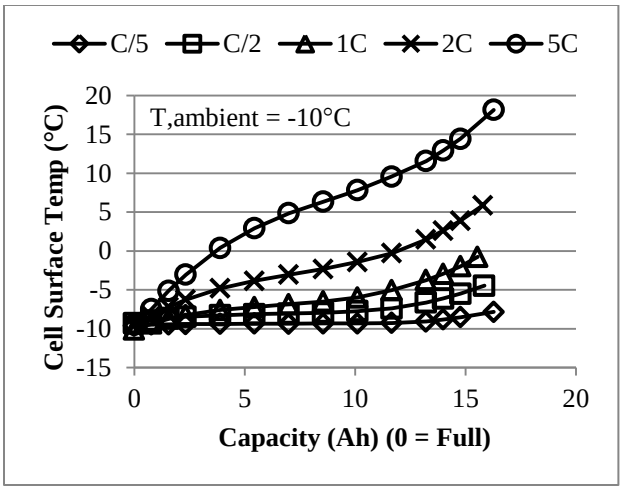
C/5
C/2
1C
2C
5C
T,ambient = -10°C
Cell Surface Temp (°C)
Capacity (Ah) (0 = Full)

(b)

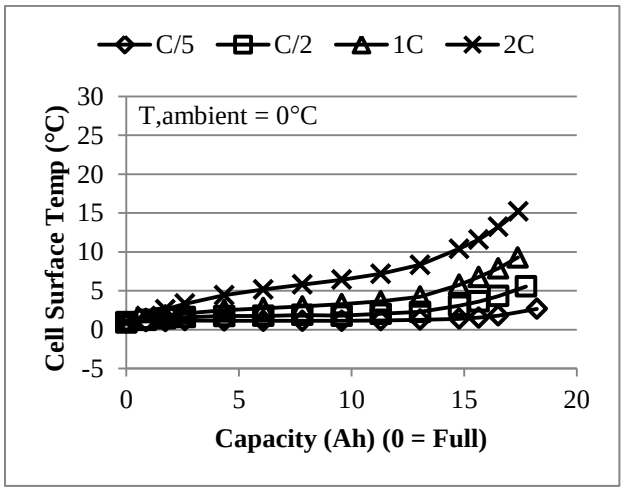
C/5
C/2
1C
2C
T,ambient = 0°C
Cell Surface Temp (°C)
Capacity (Ah) (0 = Full)

(c)

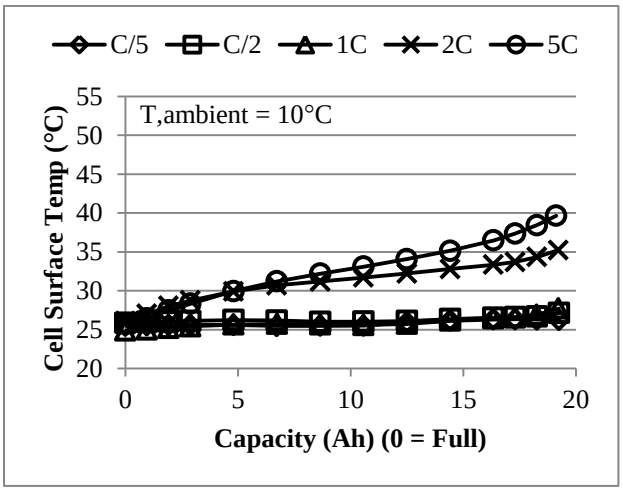
C/5
C/2
1C
2C
5C
T,ambient = 10°C
Cell Surface Temp (°C)
Capacity (Ah) (0 = Full)

(d)

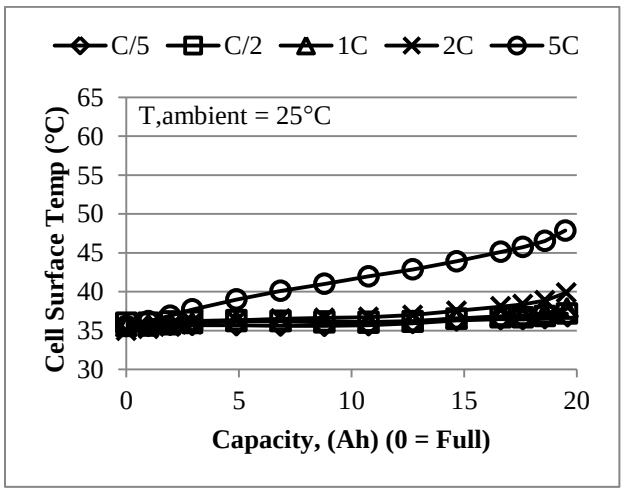
C/5
C/2
1C
2C
5C
T,ambient = 25°C
Cell Surface Temp (°C)
Capacity, (Ah) (0 = Full)

(e)

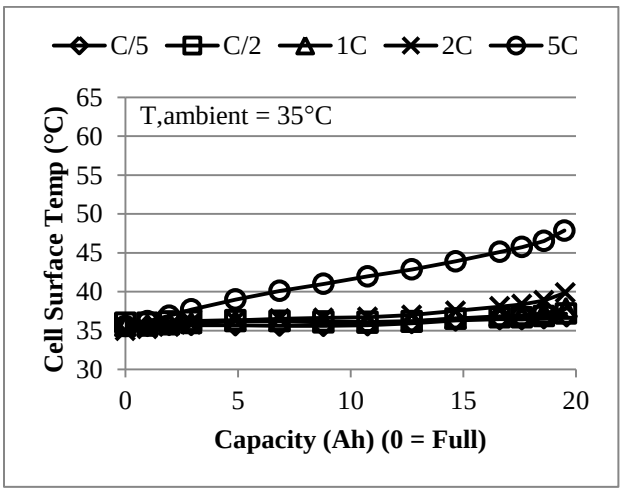
C/5
C/2
1C
2C
5C
T,ambient = 35°C
Cell Surface Temp (°C)
Capacity (Ah) (0 = Full)

(f)

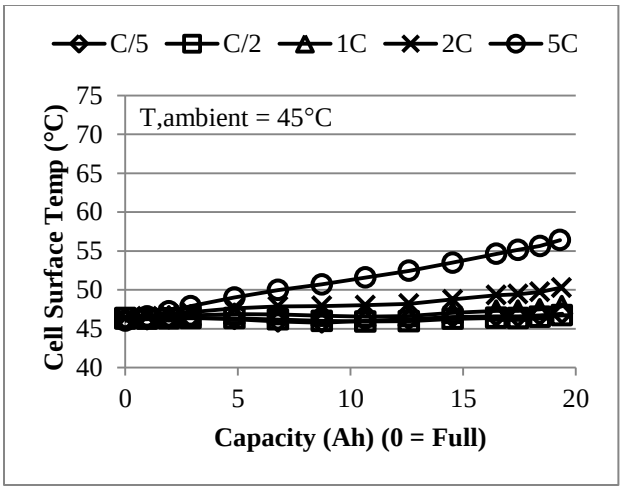

(g)

Figure 51 - Battery surface temperature during constant current discharge under ambient conditions of (a) -20°C; (b) -10°C; (c) 0°C; (d) 10°C; (e) 25°C; (f) 35°C; (g) 45°C

7.5.2 Constant Current Charge

Battery surface temperature for constant current charge profiles are shown in Figure 52. Data is shown for ambient temperatures ranging from -10°C to 45°C and for current rates of C/5, C/2, 1C, 2C, and 5C.

The temperature profile of a battery undergoing a CCCV charge is markedly different than that of a battery under constant current discharge. This is mostly because of the constant voltage portion of the charge cycle, which does not exist in the discharge profile. Characteristic of all the charge profiles is the rise in temperature during the constant current portion of the charge cycle, then fall in battery temperature during the constant voltage stage. The reason that the battery cools during the constant voltage portion of the test is that as current rate falls, less heat is generated; and natural convection moves heat away from the battery.

Interestingly, the largest temperature change is observed at 10°C and a 5C rate. It appears that at 10°C, internal resistance is just great enough that a high current rate can be maintained. At lower temperatures, high internal resistance would cause the battery to quickly hit the upper voltage limit and transition into a constant voltage mode. At higher temperatures, internal resistance is lower, so although a high current is maintained, less heat is generated. In general, charging the battery from 0% SOC to 100% SOC at a 5C charge rate will result in a 10-15°C increase in battery surface temperature. At a 2C charge rate, surface temperature rises by up to 10°C. A temperature change of less than 5°C is typical for slower charge rates.

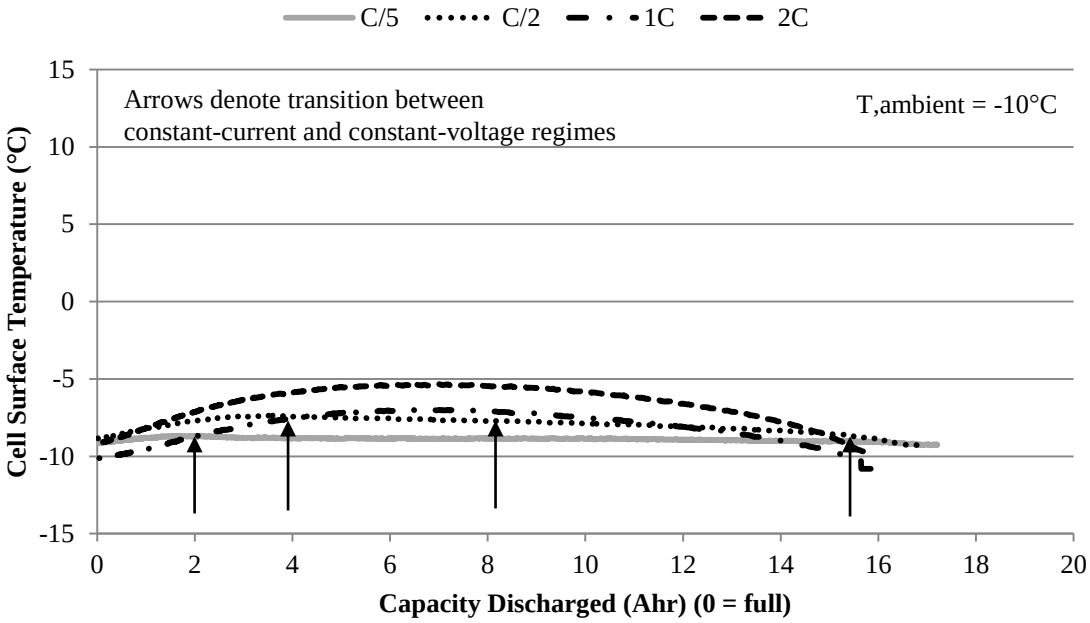
C/5
C/2
1C
2C
Arrows denote transition between
constant-current and constant-voltage regimes
T,ambient = -10°C
Cell Surface Temperature (°C)
15
10
5
0
-5
-10
-15
0
2
4
6
8
10
12
14
16
18
20
Capacity Discharged (Ahr) (0 = full)

(a)

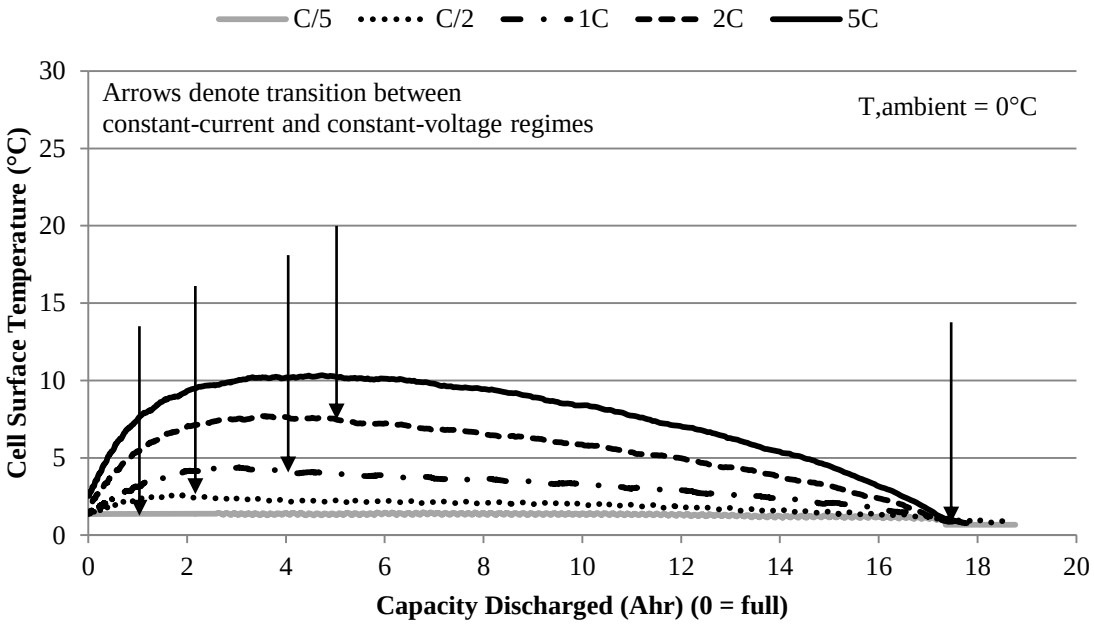
C/5
C/2
1C
2C
5C
Arrows denote transition between
constant-current and constant-voltage regimes
T,ambient = 0°C
Cell Surface Temperature (°C)
30
25
20
15
10
5
0
0
2
4
6
8
10
12
14
16
18
20
Capacity Discharged (Ahr) (0 = full)

(b)

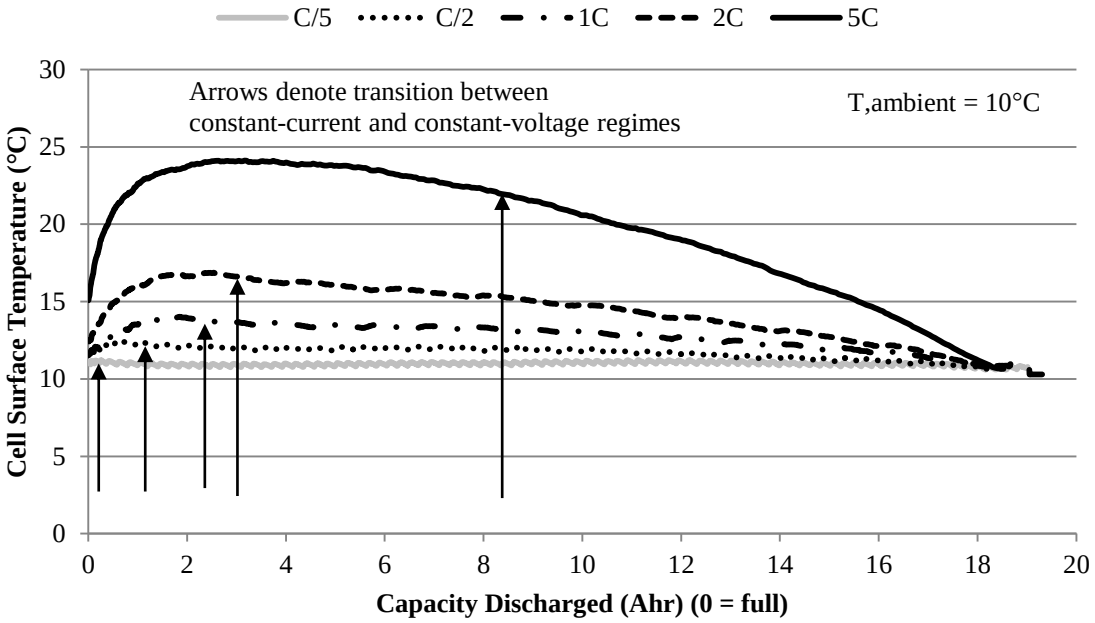
C/5
C/2
1C
2C
5C
Arrows denote transition between
constant-current and constant-voltage regimes
T,ambient = 10°C
Cell Surface Temperature (°C)
Capacity Discharged (Ahr) (0 = full)

(c)

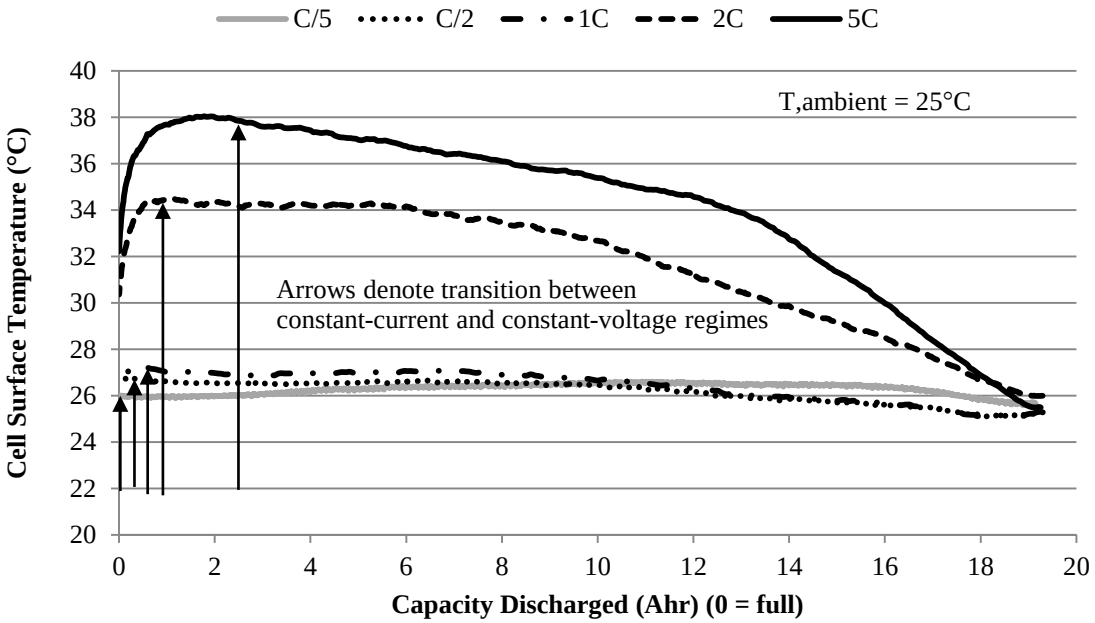
C/5
C/2
1C
2C
5C
T,ambient = 25°C
Arrows denote transition between
constant-current and constant-voltage regimes
Cell Surface Temperature (°C)
Capacity Discharged (Ahr) (0 = full)

(d)

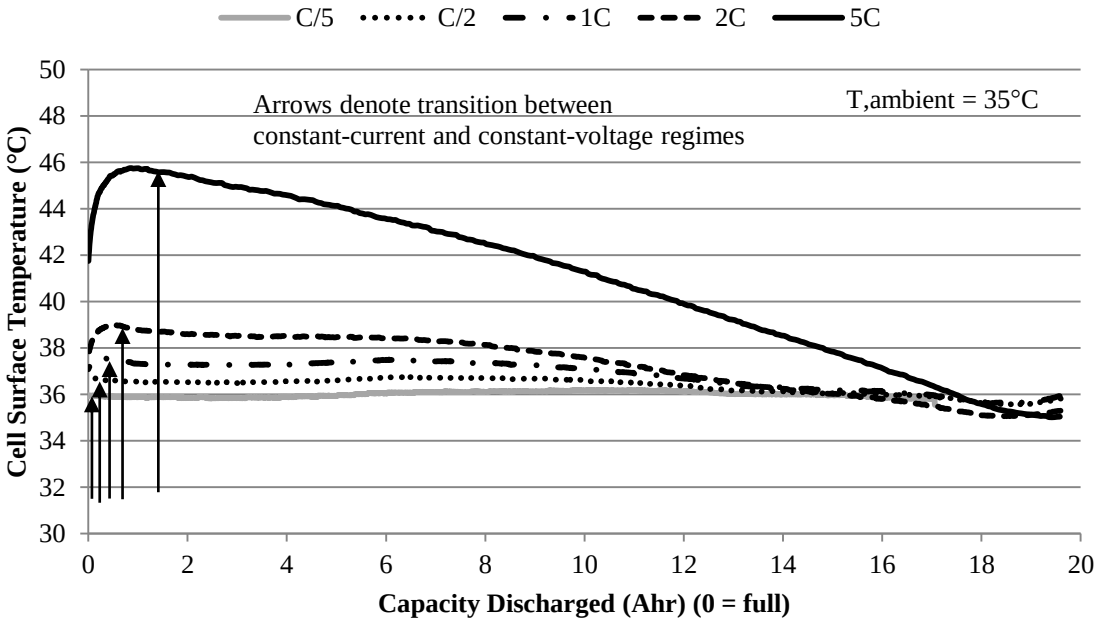

(e)

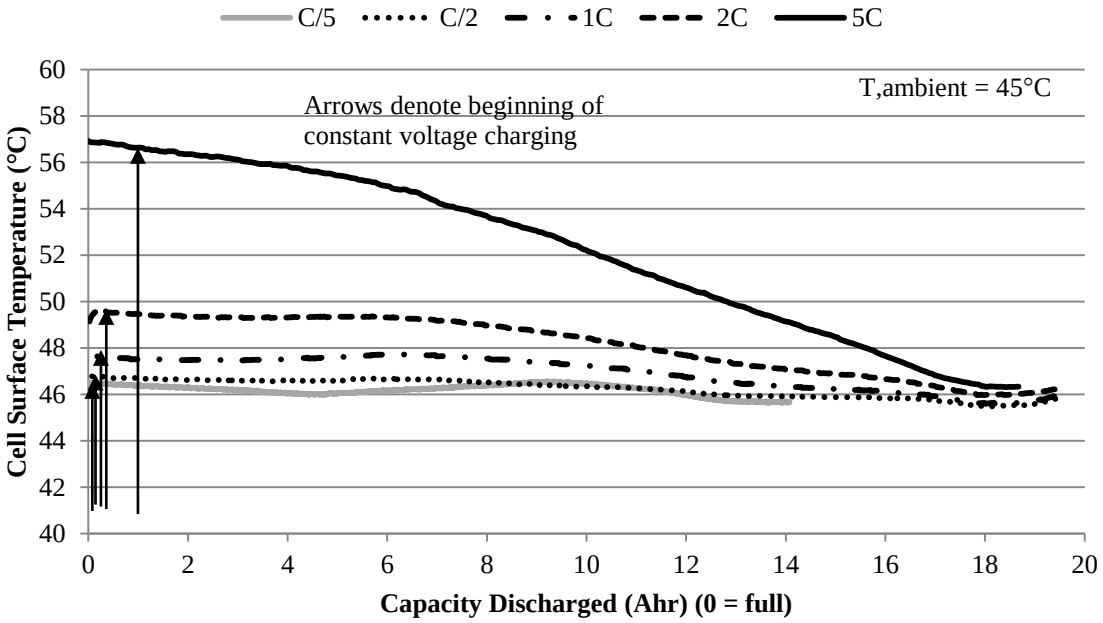

(f)

Figure 52 - Battery surface temperature during constant current charge under ambient conditions of (a) -10°C; (b) 0°C; (c) 10°C; (d) 25°C; (e) 35°C; (f) 45°C

7.6 Model Validation

To validate the accuracy of the battery model, the model was fed the same current profile that was executed experimentally for the UDDS, HWFET, and US06 drive cycles. The modeled voltage response is compared to the experimental values. Error is discussed quantitatively in Section 7.6.4.

7.6.1 Low Temperature Performance

Model performance is generally poor at temperatures of -10°C or less. Modeled performance at -20°C is plotted against experimental values in Figure 53, Figure 54, and Figure 55 for the UDDS, HWFET, and US06 current profiles, respectively. Similar plots for -10°C are shown in Appendix B.

In the UDDS and HWFET profiles, the model tends to over-estimate the battery voltage. The model also does not exhibit the gradual downward trend in battery voltage that is seen experimentally because resistance values in the model are static. At low temperatures, intra-particle diffusion limitations affect battery voltage much more significantly. Diffusion effects are non-linear and time dependent, so the R_{int} model is not well suited for describing the low temperature drive cycle behaviour of $LiFePO_4$ batteries. A model with non-linear components, such as a first- or second-order RC model, would be more capable of expressing low temperature battery behaviour, especially at low SOC.

The model performance for the US06 cycle is significantly better than that of the UDDS and HWFET cycles. This may be because the cycle is more aggressive with short, frequently alternating charge and discharge events.

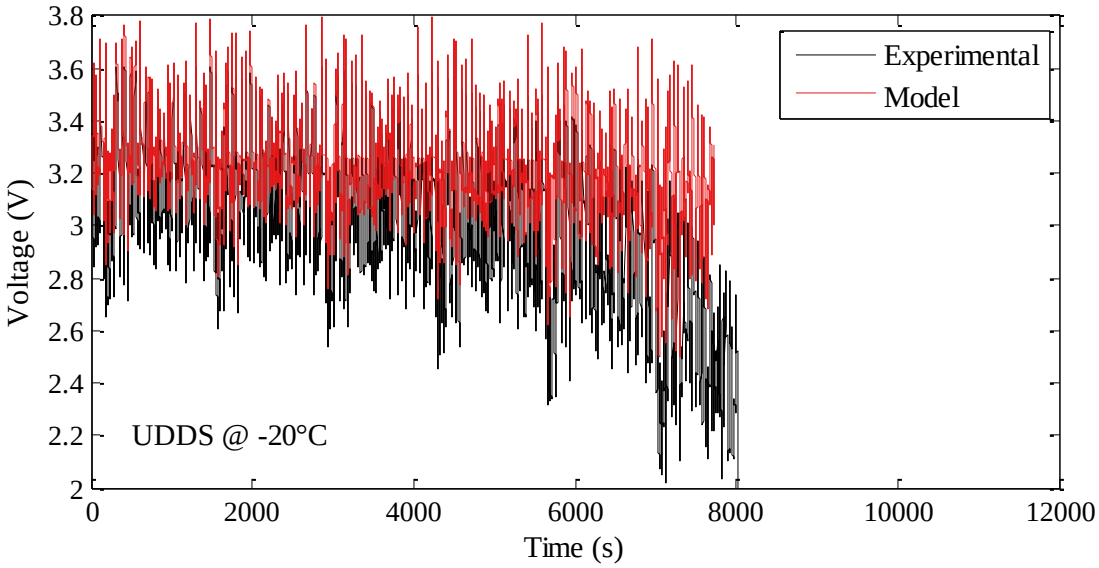

Figure 53 - Experimental vs simulated battery voltage for UDDS current profile at -20°C

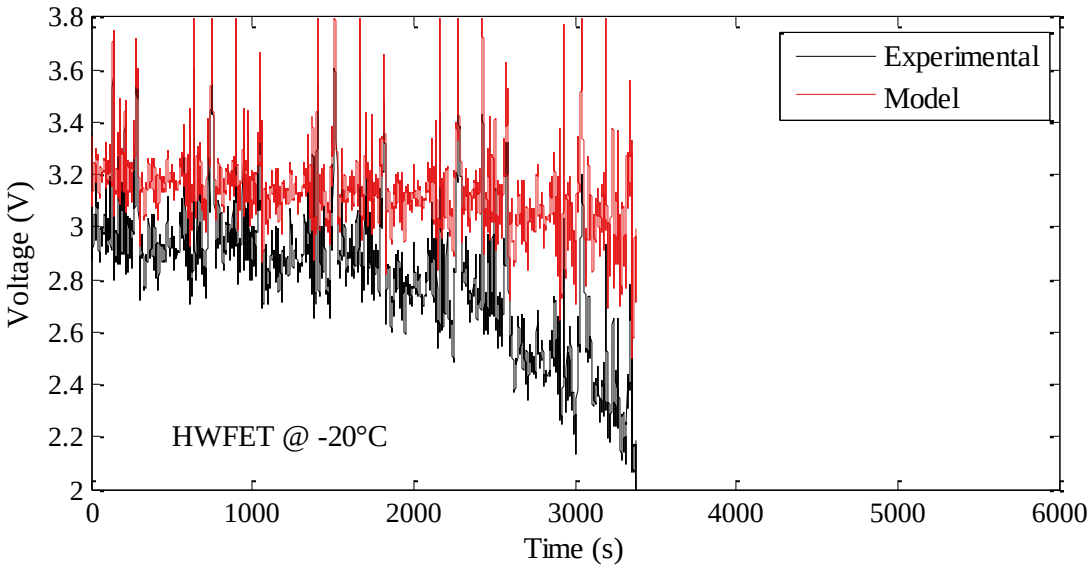

Figure 54 - Experimental vs simulated battery voltage for HWFET current profile at -20°C

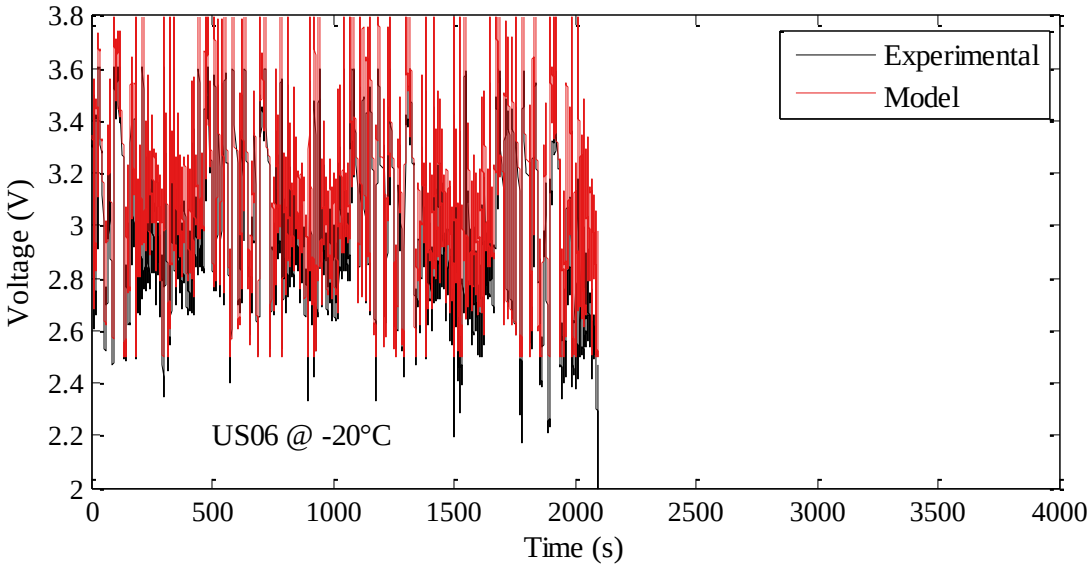

Figure 55 - Experimental vs simulated battery voltage for US06 current profile at -20°C

7.6.2 Moderate Temperature Performance

Model performance improves significantly in the 0°C to 10°C range. Modeled performance at 10°C is plotted against experimental values in Figure 56, Figure 57, and Figure 58 for the UDDS, HWFET, and US06 current profiles, respectively. Similar plots for 0°C are shown in Appendix B

The model still appears to still bias to a slightly higher voltage than the experimental values, but the model aligns with the experimental values well for the most part. Compared to the low temperature results, voltage fluctuations are smaller and overall model accuracy is higher. UDDS cycle model performance is clearly the best of the three. The model overestimates battery voltage over HWFET and US06 cycles at low SOC, but moderate SOC performance is good. Internal resistance is significantly reduced at moderate temperatures compared to low temperatures, demonstrated by the higher average potential values.

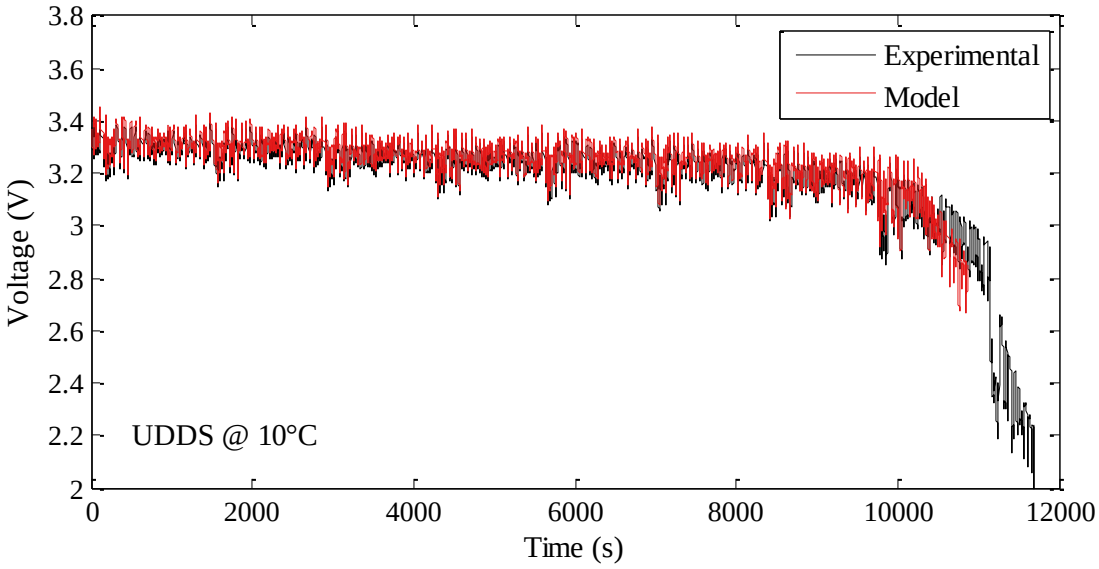

Figure 56 - Experimental vs simulated battery voltage for UDDS current profile at 10°C

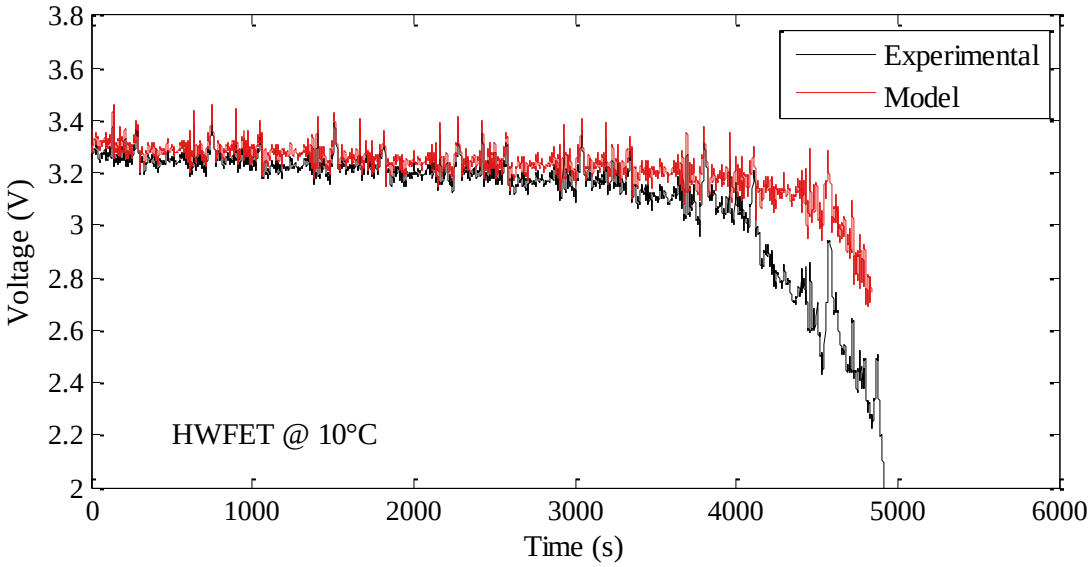

Figure 57 - Experimental vs simulated battery voltage for HWFET current profile at 10°C

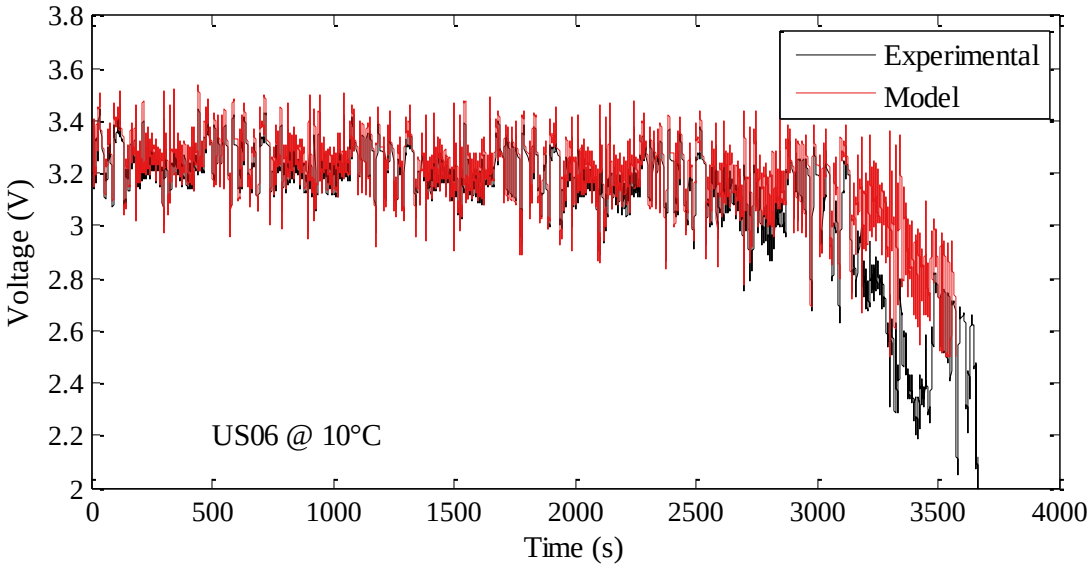

Figure 58 - Experimental vs simulated battery voltage for US06 current profile at 10°C

7.6.3 High Temperature Performance

Model performance shows further improvement in the 25°C to 45°C range. Modeled performance at 45°C is plotted against experimental values in Figure 59, Figure 60, and Figure 61 for the UDDS, HWFET, and US06 current profiles, respectively. Similar plots for 25°C and 35°C are shown in Appendix B

For all drive cycles, model accuracy appears to be excellent throughout the moderate SOC range. Low SOC performance is also fairly good for the HWFET and US06 cycles. Experimentally, the UDDS cycle ran longer than the model predicted. The net discharged energy was 19.63 Ah, compared to the 19.38 Ah capacity determined experimentally. Self-heating may be a contributing factor to the weakness of the model fit at low temperature, but also in the observed expanded the usable battery capacity, especially at lower temperatures.

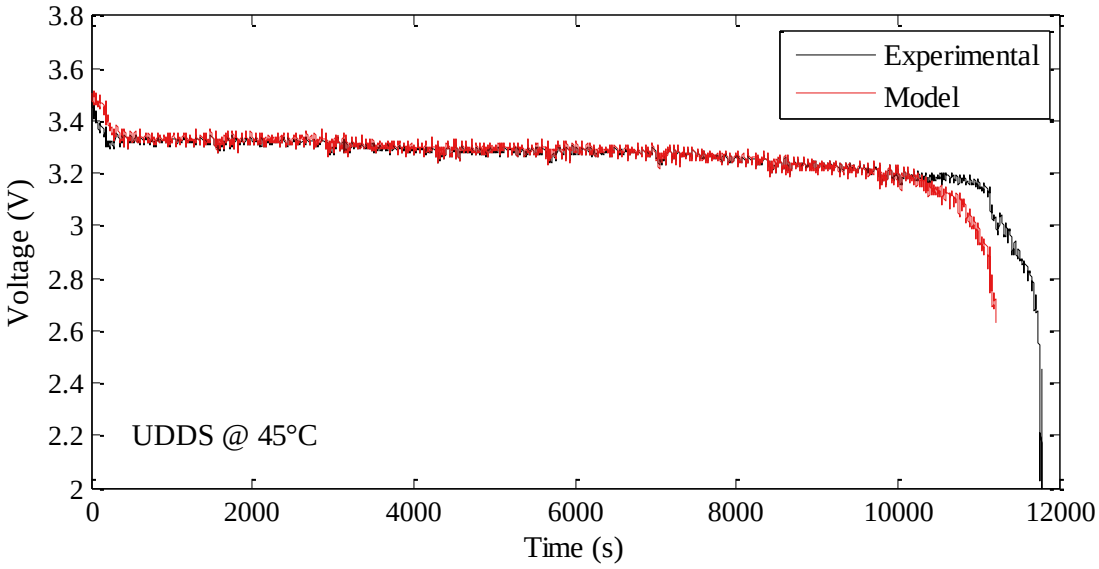

Figure 59 - Experimental vs simulated battery voltage for UDDS current profile at 45°C

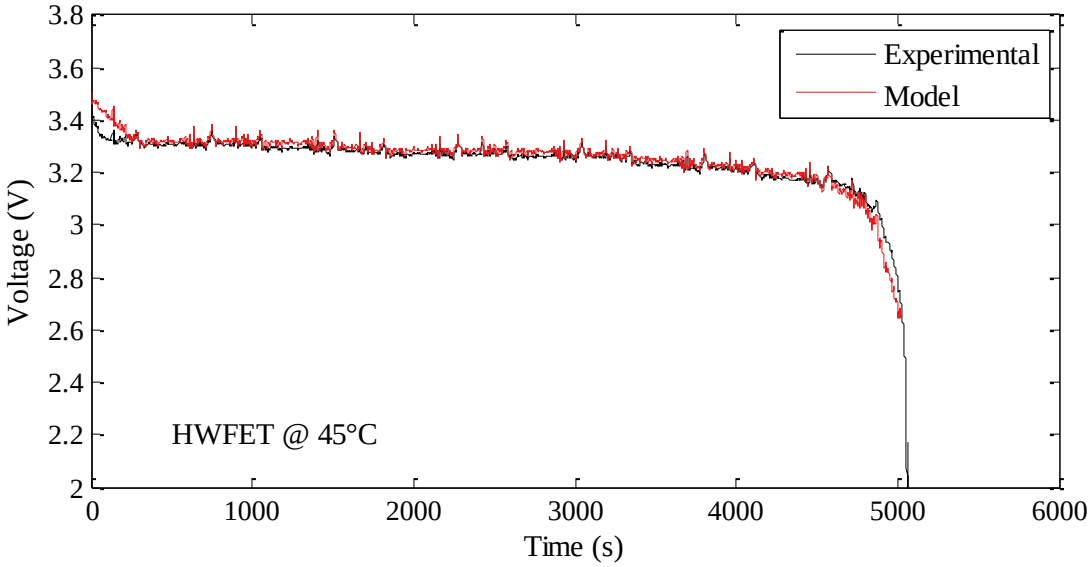

Figure 60 - Experimental vs simulated battery voltage for HWFET current profile at 45°C

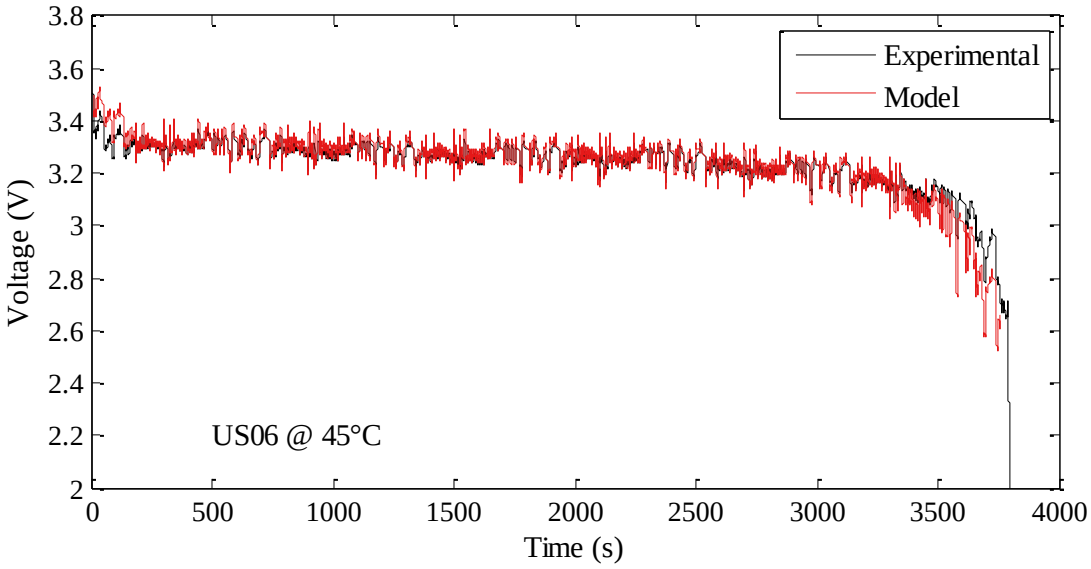

Figure 61 - Experimental vs simulated battery voltage for US06 current profile at 45°C

7.6.4 Error

The ability of the model to predict battery voltage response is assessed using the root mean square error (RMSE) method. Simulation results for the UDDS, HWFET, and US06 drive cycle current waveforms are compared against experimental values at various temperatures. Figure 62 shows the RMSE of the drive cycles across the battery's full SOC range. RMSE values represent the quadratic mean of the error observed. For temperatures of 25°C and higher, RMSE stays between 40-80 mV for all three drive cycles, a deviation equivalent to 1-2% of the cell's nominal voltage. However, as temperature decreases, error rises rapidly. RMSE at -20°C ranges from 203mV for the US06 cycle to 369mV for the HWFET cycle, a deviation equivalent to 5-10% of the cell's nominal voltage. The difference in RMSE values between the drive cycles also becomes magnified at low temperatures.

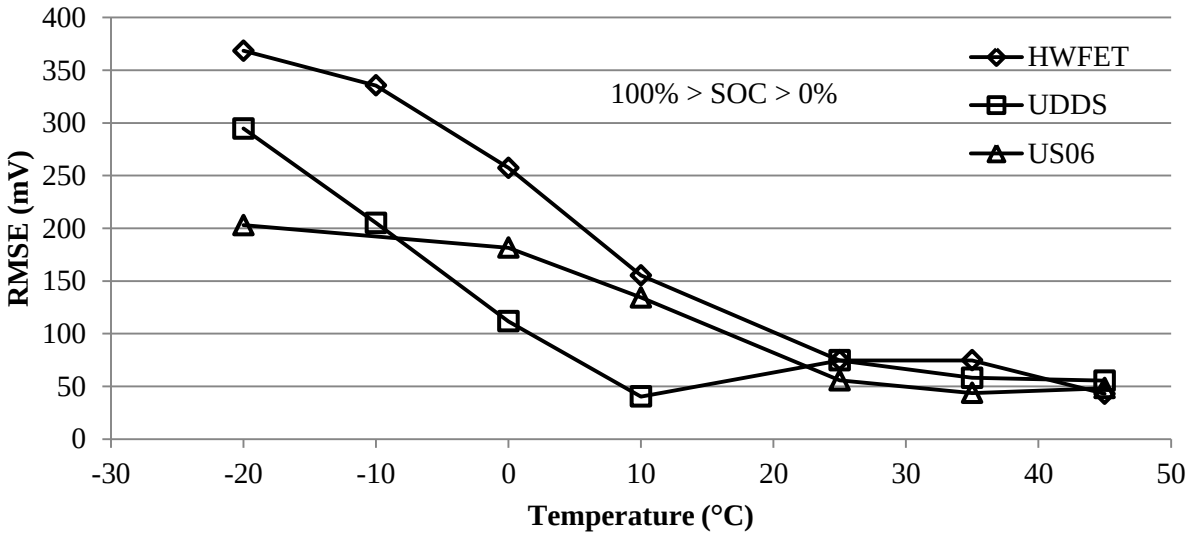

Figure 62 - RMSE for voltage performance of model from 100% SOC to 0% SOC

Observation of Figure 53 through Figure 61 clearly reveals that model performance is poorest at very high and low SOCs. In application, however, the battery will only normally only operate between 25% and 90% SOC. Model RMSE for this SOC range is shown in Figure 63. Performance is markedly better in the 25-90% SOC window, although model performance is still significantly impacted by temperature. RMSE values for 25°C and above was found to be below 30mV for all drive cycles. At -20°C, RMSE ranges from 196mV for the US06 cycle to 281mV for the HWFET.

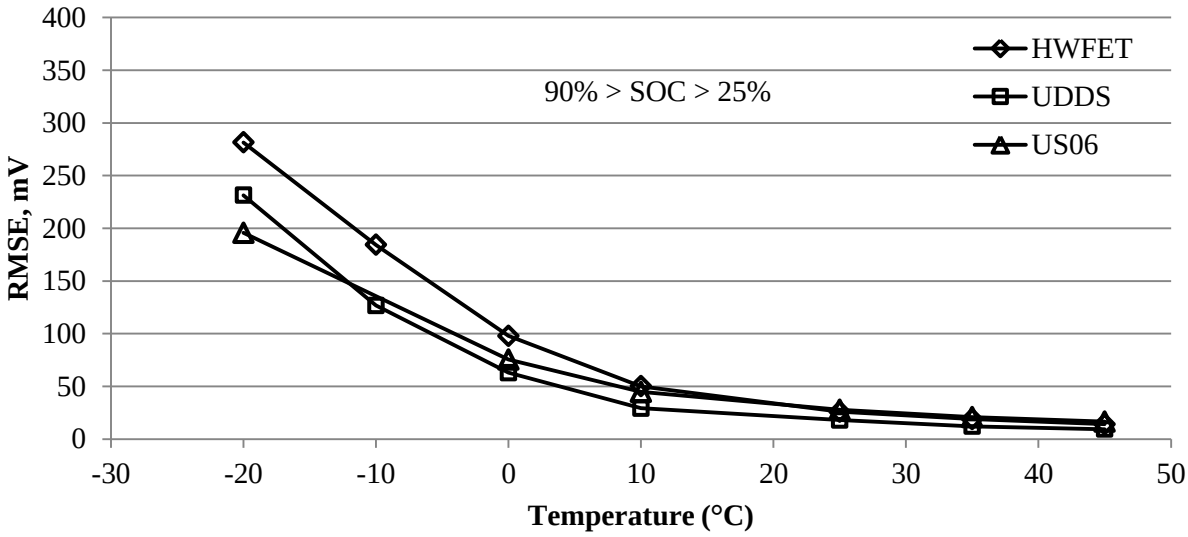

Figure 63 - RMSE for voltage performance of model from 90% SOC to 25% SOC

7.7 Vehicle performance

7.7.1 All Electric Range

The expanded, temperature dependent battery model was implemented in the AWD series PHEV vehicle model. Simulations were carried out at temperatures ranging from -20°C to 45°C. SOC was bounded between 90% and 25% for the purposes of determining all-electric range. The results are shown in Figure 64.

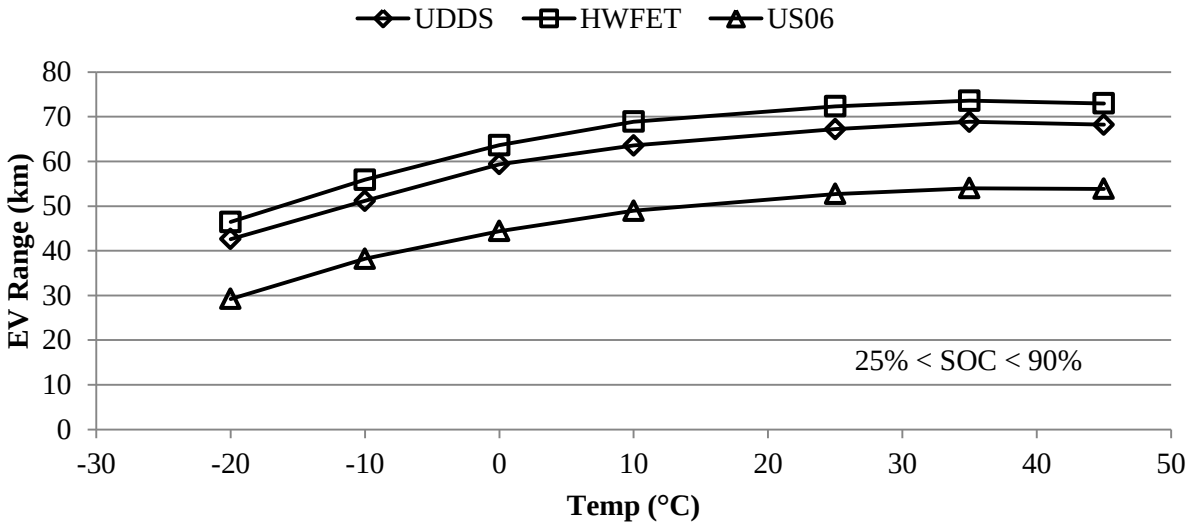

Figure 64 - Simulated all-electric range for UDDS, HWFET, and US06 drive cycles at different temperatures

All-electric range is highest at 25°C and above. It decreases quickly as temperature falls. At -20°C, the vehicle would lose 24.6km (37%) of range under the UDDS cycle, 25.9km (36%) under the HWFET, and 23.5km (44%) under the US06 cycle. The two contributors to this loss of range is decreased battery capacity and decreased charge and discharge efficiency at low temperature. As discussed in Section 7.1, a 30% loss in capacity – and therefore range – is expected from 25°C to -20°C. A further 6-16% loss in range may be attributed to charge and discharge inefficiencies, which is discussed in Section 7.7.2. Depending on the drive cycle, the total expected reduction of electric range due to low temperature capacity loss and battery inefficiency is between 34% and 41%. The observed difference in all-electric range between 25°C and -20°C is thus explained for the UDDS and HWFET cycles. The US06 cycle, due to its

aggressiveness and large power draws may have terminated early due to reaching a voltage limit. Similar explanations can be applied to other temperatures. It should be noted that the other vehicle components (eg. engine, motor, generator) do not have temperature dependent models and in the actual application may be more severely impacted because of their location (i.e. less insulated). These models also need to be capable of accounting for the effect of temperature to refine the all-electric range estimates. Vehicle testing should also be carried out to validate and refine the models.

Some caution should be exercised when scaling experimental data from a single cell to represent an entire battery pack, as it may not scale linearly. For example, single cell data includes an element of resistance between the battery tab and the connector bolted to it. In a production battery pack, the tabs would likely be welded to a bus bar, changing the resistance characteristics. As such, the internal resistance of an actual battery pack would likely be lower than the single cell internal resistance multiplied by the number of cells in the battery pack.

7.7.2 Battery Efficiency

An ideal battery could be considered as one that does not deviate from its open circuit voltage – that is, one that has no internal resistance. This ideal battery would deliver the maximum energy and the minimum possible energy required to charge the battery. By comparing the simulated battery performance to the ideal case, a measure of efficiency may be obtained.

The overall charge and discharge efficiencies over a duty cycle are given by Equation 5 and Equation 6

$$\varepsilon_{chg} = \sum_{i=1}^{N} \frac{1}{N} \left(\frac{V_{OC,i}}{V_{sim,i}} \right) \qquad \text{Equation 5}$$

$$\varepsilon_{dis} = \sum_{i=1}^{N} \frac{1}{N} \left(\frac{V_{sim,i}}{V_{OC,i}} \right) \qquad \text{Equation 6}$$

where ε_{chg}, ε_{dis} is the overall charge and discharge efficiency of the battery, respectively;

V_{OC} is the open circuit voltage of the battery at data point *i;*

V_{sim} is the simulated voltage of the battery at data point *i;*

I_{sim} is the simulated current of the battery at data point *i; and*

N is the number of data points

Simulated charge efficiency for the HWFET, UDDS, and US06 drive cycles for temperatures ranging from -20°C to 45°C are shown in Figure 65. At temperatures of 25°C and higher, efficiency is above 98% for all drive cycles. Efficiency falls at lower temperatures and the difference between the three drive cycles widens. UDDS is the most efficient cycle for the battery, while US06 is the least efficient. At -20°C, charge efficiency is 5 to 10 percent lower than at 25°C or higher. Vehicle simulations show that regenerative braking may recover a maximum of 22% of the discharged energy, so losses due to battery charging could account for a up to a 2.2% loss of electric range at very low temperatures.

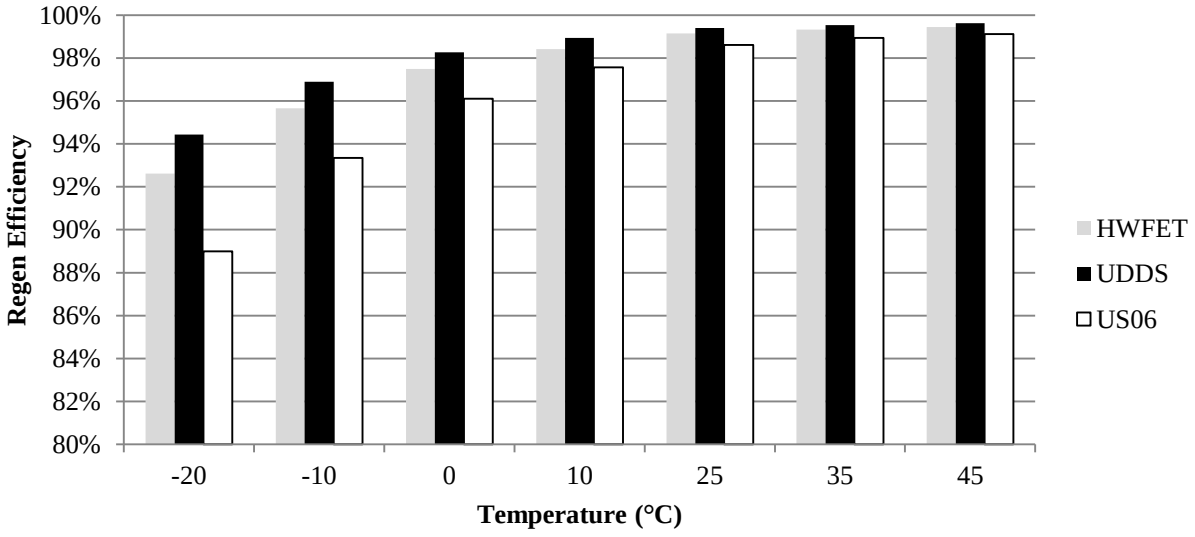

Figure 65- Overall battery charge efficiency during all-electric operation for HWFET, UDDS, and US06 drive cycles at various temperatures

Simulated discharge efficiencies for the HWFET, UDDS, and US06 cycles are shown in Figure 66. At -20°C, discharge efficiency is 5 to 14 percent lower than at 25°C or higher. Discharge inefficiency caused by low temperatures therefore reduces electric range by a further 5-14% after adjusting for range lost due to apparent capacity. As with charge efficiency, the UDDS cycle allows the battery to work most efficiently, while US06 is the most inefficient.

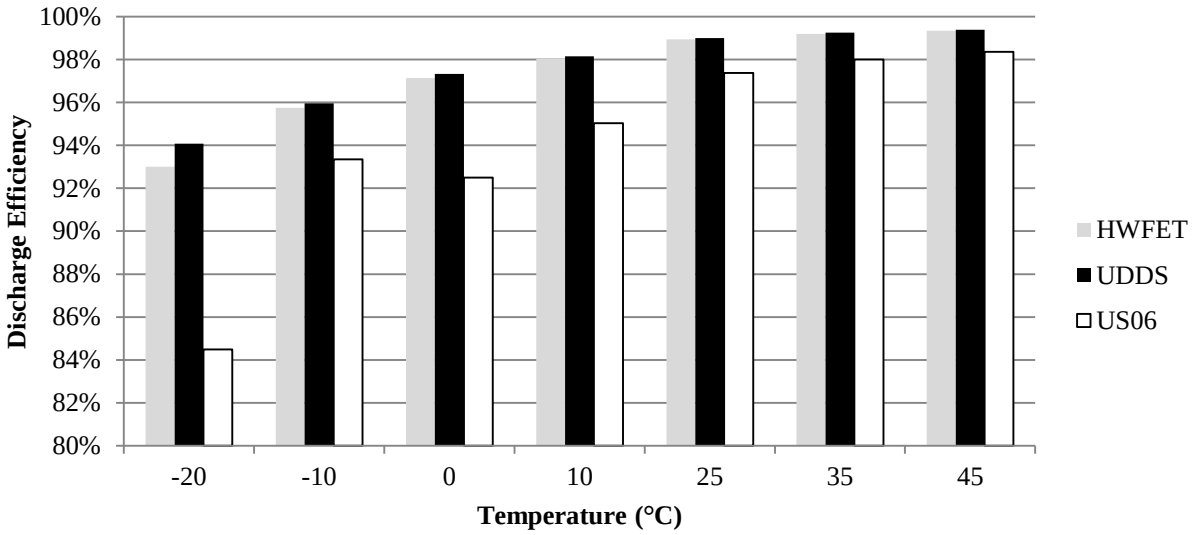

Figure 66 - Overall battery discharge efficiency during all-electric operation for HWFET, UDDS, and US06 drive cycles at various temperatures

8 Conclusions

The following was achieved:

1. A battery test bench was successfully assembled to perform automated testing of single cell lithium-ion batteries. Battery performance was measured using constant current charge and discharge events; hybrid pulse power characterization tests; and UDDS, HWFET, and US06 current profiles.

2. A series PHEV utilizing two electric traction motors was modeled in Autonomie. The model enables simulation of dynamic performance for the UWAFT's EcoCAR2 vehicle which is a modified 2012 Malibu plug-in hybrid. Additionally, the vehicle model provides the framework upon which electric powertrain component models and vehicle control strategies can be developed and evaluated. A 19.7kWh battery pack consisting of seven 15s3p modules was chosen.

3. A temperature dependent R_{int} type battery model was successfully parameterized for A123's $LiFePO_4$ batteries using experimental values and used in Autonomie to estimate vehicle all-electric range at temperatures ranging from -20°C to 45°C.

4. At low temperatures, the battery affects vehicle electric range mainly due to loss of capacity and decreased efficiency. At -20°C, only 70% of the rated capacity is accessible, meaning vehicle range is reduced by 30%. Decreased efficiency at -20°C results in an additional 5-14% loss of electric range compared to performance at 25°C depending on the drive cycle.

9 Recommendations and Next Steps

This work has laid the foundation for using experimental data to model an A123 battery at different temperatures in a PHEV vehicle model. Much can still be done to improve model accuracy.

1. More rigorous thermal testing of the batteries should be carried out to obtain more accurate surface temperature measurements. Thermal gradients across the cell should be mapped. Heat generation and heat capacity of the cells should be found and incorporated into the existing model. Self-heating can then be simulated, and strategies for heating and cooling the batteries can be developed. The battery needs to be tested in an 'jig' that better simulate a cell within a pack.

2. Since the battery pack in actual vehicle will have cooling system, the battery model should include a self-heating (i.e. thermal ramp rate) model to an operational temperature of 25°C, and the maintenance of the temperature at that value.

3. Pack level testing should be carried out. While the model has been validated at the cell level, single cell characteristics may not be linearly scaled to a module or pack level system. For example, the resistances observed from a single cell would include contact resistances where the cell tabs are bolted to the test cables. In a production battery pack, the tabs would be welded to a bus bar, changing the resistance characteristics. Evaluating the internal resistance of a full battery pack would improve the fidelity of the model and yield more accurate vehicle simulation results.

4. Temperature dependent models for other major powertrain components such as electric motors should be created to more accurately model how total vehicle efficiency changes with temperature. Accurate representation of the entire vehicle is required to accurately predict vehicle range, performance, and overall energy consumption.

As the vehicle model matures, it will also serve as a platform for developing vehicle control systems, torque splitting strategies and other optimization algorithms.

References

[1] Natural Resources Canada's Office of Energy Efficiency, "2007 Canadian Vehicle Survey Summary Report," Natural Resources Canada, Ottawa, 2009.

[2] Environment Canada, "National Inventory Report 1990-2012 - Greenhouse Gas Sources and Sinks in Canada," Environment Canada, Gatineau, 1910-7064, 2012.

[3] Environment Canada. Canada's Electricity Story. [Online]. http://www.ec.gc.ca/default.asp?lang=En&xml=0A6CF209-AF7A-4913-A27F-527B4ECF811B.

[4] Oak Ridge National Laboratory, "A Comparative Study of Emerging Vehicle Technology Assessments," ORNL, Oak Ridge, 2011.

[5] Hans Greimel. (2012, April) Automotive News. [Online]. http://www.autonews.com/apps/pbcs.dll/article?AID=/20120430/OEM01/304309976/1424

[6] Nicholas Lutsey, "A technical analysis of model year 2011 US automobile efficiency," *Transportation Research Part D*, vol. 17, pp. 361-369, 2012.

[7] S L Miller, M N Svrcek, K-Y Teh, and C F Edwards, "Assessing the feasibility of increasing engine efficiency through extreme compression," *International Journal of Engine Research*, vol. 12, no. 3, p. 293, 2011.

[8] U.S. Department of Energy. (2012, June) Energy Efficiency & Renewable Energy. [Online]. http://www.fueleconomy.gov/feg/current.shtml

[9] Massimo Ceraolo, Antonio di Donato, and Giulia Franceschi, "A General Approach to Energy Optimization of Hybrid Electric Vehicles," *IEEE Transactions of Vehicular Technology*, vol. 57, no. 3, pp. 1433-1441, May 2008.

[10] Robert Myers. (2007) Mathworks. [Online]. http://www.mathworks.com/company/newsletters/articles/evaluating-plug-in-series-hybrid-designs-for-postal-delivery-vehicles.html

[11] MIT Electric Vehicle Team. (2008) MIT Electric Vehicle Team. [Online]. http://web.mit.edu/evt/summary_powertrains.pdf

[12] C. C. Chan, Alain Bouscayrol, and Keyu Chen, "Electric, Hybrid, and Fuel-Cell Vehicles: Architectures and Modeling," *IEEE Transactions on Vehicular Technology*, vol. 59, no. 2,

pp. 589-598, February 2010.

[13] Mojtaba Shams-Zahraei and Abbas Z. Kouzani, "A Study of Plug-in Hybrid Electric Vehicles," in *IEEE Region 10 Conference*, Singapore, 2009, pp. 1-5.

[14] Jinming Liu, Huei Peng, and Zoran Filipi, "Modeling and Analysis of the Toyota Hybrid System," in *International Conference on Advanced Intelligent Mechatronics*, Monterey, 2005, pp. 134-139.

[15] J. Kessels, "Energy management for automotive power net," Technische Universiteit Eindhoven, Eindhoven, Ph.D. dissertation 2007.

[16] Thomas D. Gillespie, *Fundamentals of Vehicle Dynamics*, Thomas D. Gillespie, Ed. Warrendale, PA: Society of Automotive Engineers, 1992.

[17] United States Environmental Protection Agency. (2010, June) Dynamometer Driver's Aid. [Online]. http://www.epa.gov/nvfel/testing/dynamometer.htm

[18] Dean Rotenberg, Ardalan Vahidi, and Ilya Kolmanovsky, "Ultracapacitor Assisted Powertrains: Modeling, Control, Sizing, and the Impact on Fuel Economy," *IEEE Transactions on Control Systems Technology*, vol. 19, no. 3, pp. 576-589, May 2011.

[19] Y Gene Liao and Allen M. Quail, "Traction motor sizing for optimal fuel economy in propulsion hybridization," *The Open Mechanial Engineering Journal*, vol. 6, pp. 1-11, 2012.

[20] Junjie Li, Xiumin Yu, Huajie Ding, and Ping Sun, "Design and control of the Propulsion for a Series Hybrid Electric Vehicle," in *World Congress on Intelligent Control and Automation*, Changchun, 2010, pp. 2159-2162.

[21] Hoseinali Borhan et al., "MPC-Based Energy Management of a Power-Split Hybrid Electric Vehicle," *IEEE Transactions on Control Systems Technology*, vol. 20, no. 3, pp. 593-603, May 2012.

[22] Yiming He, Mashrur Chowdhury, Pierluigi Pisu, and Yongchang Ma, "An energy optimization strategy for power-split drivetrain plug-in hybrid electric vehicles," *Transpoartation Research Part C*, vol. 22, pp. 29-41, 2012.

[23] Menyang Zhang, Yan Yang, and Chunting Chris Mi, "Analytical Approach for the Power Management of Blended-Mode Plug-In Hybrid Electric Vehicles," *IEEE Transactions onf*

Vehicular Technology, vol. 61, no. 4, pp. 1554-1566, May 2012.

[24] J Wishart, Y.L. Zhou, Z Dong, and F Firmani, "Dynamic modelling and simulation of a multi-regime hybrid vehicle powertrain architecture," *International Journal of Electric and Hybrid Vehicles*, vol. 1, no. 2, pp. 188-219, April 2008.

[25] The Freedonia Group, Batteries.

[26] Frost & Sullivan, Frost & Sullivan Projects Explosive Growth for Lithium-ion Batteries in Electric Vehicle and Hybrid Electric Vehicle Segments, 2010.

[27] David Linden and Thomas B. Reddy, *Handbook of batteries*, 3rd ed.: McGraw-Hill, 2002, ID: 46792664.

[28] AGM Batteries Ltd, Lithium Ion Batteries - An Introduction, 2009.

[29] Ali Reza Kamali and Derek J. Fray, "Review on Carbon and Silicon Based Materials as Anode Materials for Lithium Ion Batteries," *Journal of New Materials for Electrochemical Systems*, vol. 13, pp. 147-160, 2010.

[30] Jaephil Cho et al., "Comparison of Al2O3- and AlPO4-coated LiCoO2 cathode materials for a Li-ion cell," *Journal of Power Sources*, vol. 146, pp. 58-64, 2005, Selected papers pressented at the 12th International Meeting on Lithium Batteries.

[31] Jeffrey W. Fergus, "Recent developments in cathode materials for lithium ion batteries," *Journal of Power Sources*, vol. 195, pp. 939-954, 2010.

[32] Hui Cao, Baojia Xia, Yao Zhang, and Naixin Xu, "LiAlO2-coated LiCoO2 as cathode material for lithium ion batteries," *Solid State Ionics*, vol. 176, pp. 911-914, 2005.

[33] A.P. Lewandowski, A.F. Hollenkamp, S.W. Donne, and A.S. Best, "Cycling and rate performance of Li-LiFePO4 cells in mixed FSI-TFSI room temperature ionic liquids," *Journal of Power Sources*, vol. 195, pp. 2029-2035, 2010.

[34] S.A. Needham, G.X. Wang, H.K. Liu, V.A. Drozd, and R.S. Liu, "Synthesis and electrochemical performance of doped LiCoO2 materials," *Journal of Power Sources*, vol. 174, pp. 828-831, 2007, 13th International Meeting on Lithium Batteries.

[35] Jong Park et al., "Effect of conducting additives on the properties of composite cathodes for lithium-ion batteries," *Journal of Solid State Electrochemistry*, vol. 14, no. 4, pp. 593-597, 2010, 10.1007/s10008-009-0814-5.

[36] Yang Shao-Horn, Laurence Croguennec, Claude Delmas, E. Chris Nelson, and Michael A. O'Keefe, "Atomic resolution of lithium ions in LiCoO2," *Nat Mater*, vol. 2, pp. 464-467, 2003.

[37] Xiangming He et al., "Preparation of co-doped spherical spinel LiMn2O4 cathode materials for Li-ion batteries," *Journal of Power Sources*, vol. 150, pp. 216-222, 2005.

[38] J.P. Tu, H.M. Wu, Y.Z. Yang, and W.K. Zhang, "Spray-drying technology for the synthesis of nanosized LiMn2O4 cathode material," *Materials Letters*, vol. 61, pp. 864-867, 2007.

[39] Hyun-Wook Lee et al., "Ultrathin Spinel LiMn2O4 Nanowires as High Power Cathode Materials for Li-Ion Batteries," *Nano Letters*, vol. 10, pp. 3852-3856, 2010.

[40] C.M. Julien, "Local structure of lithiated manganese oxides," *Solid State Ionics*, vol. 177, pp. 11-19, 2006.

[41] Fernanda F. C. Bazito and Roberto M. Torresi, "Cathodes for lithium ion batteries: the benefits of using nanostructured materials," *Journal of the Brazilian Chemical Society*, vol. 17, pp. 627-642, 2006.

[42] Han Chen et al., "Preparation and electrochemical performance of LiFePO4/C composite with network connections of nano-carbon wires," *Materials Letters*, vol. 65, pp. 559-561, 2011.

[43] Sung-Yoon Chung, Jason T. Bloking, and Yet-Ming Chiang, "Electronically conductive phospho-olivines as lithium storage electrodes," *Nat Mater*, vol. 1, pp. 123-128, 2002.

[44] Lin Zou et al., "Investigations on the modified natural graphite as anode materials in lithium ion battery," *Journal of Physics and Chemistry of Solids*, vol. 69, pp. 1265-1271, 2007.

[45] Ralph J Brodd and Akiya Kozawa, *Lithium-Ion Batteries: Science and Technologies*. New York, USA: Springer, 2009.

[46] B. Gao et al., "Enhanced saturation lithium composition in ball-milled single-walled carbon nanotubes," *Chemical Physics Letters*, vol. 327, pp. 69-75, 2000.

[47] Doron Aurbach et al., "Design of electrolyte solutions for Li and Li-ion batteries: a review," *Electrochimica Acta*, vol. 50, pp. 247-254, 2004, Polymer Batteries and Fuel Cells:Selection of Papers from First International Conference.

[48] George E. Blomgren, "Liquid electrolytes for lithium and lithium-ion batteries," *Journal of*

Power Sources, vol. 119-121, pp. 326-329, 2003, Selected papers presented at the 11th International Meeting on Lithium Batteries.

[49] Sheng Shui Zhang, "A review on electrolyte additives for lithium-ion batteries," *Journal of Power Sources*, vol. 162, pp. 1379-1394, 2006, Special issue including selected papers from the International Power Sources Symposium 2005 together with regular papers.

[50] Idaho National Laboratory, Battery Test Manual for Plug-in Hybrid Electric Vehicles, 2010.

[51] Hongwen He, Rui Xiong, and Jinxin Fan, "Evaluation of Lithium-Ion Battery Equivalent Circuit Models for State of Charge Estimation by an Experimental Approach," *Energies*, vol. 4, pp. 582-598, March 2011.

[52] Xiaosong Hu, Shengbo Li, and Huei Peng, "A comparative study of equivalent circuit models for Li-ion batteries," *Journal of Power Sources*, vol. 198, pp. 359-367, October 2012.

[53] Shuoqin Wang, Mark Verbrugge, John S Wang, and Ping Liu, "Power prediction from a battery state estimator that incorporates diffusion resistance," *Journal of Power Sources*, vol. 214, pp. 399-406, April 2012.

[54] Taesic Kim and Wei Qiao, "A Hybrid Battery Model Capable of Capturing Dynamic Circuit Characteristics and Nonlinear Capacity Effects," *IEEE Transactions on Energy Conversion*, vol. 26, no. 4, pp. 1172-1180, December 2011.

[55] Tarun Huria, Massimo Ceraolo, Javier Gazzarri, and Robyn Jackey, "High Fidelity Electrical Model with Thermal Dependence for Characterization and Simulation of High Power Lithium Battery Cells," in *Electric Vehicle Conference (IEVC), 2012 IEEE International*, Greenville, 2012, pp. 1-8.

[56] Matthew Genovese, Gregory Laskey, and Matthew Kok, "Thermal Management System of a Lithium Ion Battery Pack for a Plug-In Hybrid Electric Vehicle," University of Waterloo, Waterloo, CHE483 Final Design Report 2012.

Appendix A

Numerical values for the parameterized battery model are provided in this Appendix.

Table A1 - Battery model parameters: Capacity (amp-hours)

Temperature (°C)	Capacity (Ahr)
-20	13.275
-10	15.550
0	17.389
10	18.547
25	19.234
35	19.567
45	19.382

Table A2 - Battery model parameters: Open circuit voltage (volts)

SOC (%)	Temperature (°C)						
	-20	-10	0	10	25	35	45
0	3.202	3.184	3.075	2.844	2.405	2.714	2.683
5	3.232	3.228	3.211	3.178	3.187	3.118	3.106
10	3.246	3.244	3.232	3.208	3.208	3.205	3.204
15	3.255	3.256	3.25	3.231	3.231	3.221	3.218
25	3.269	3.272	3.273	3.263	3.26	3.254	3.252
35	3.275	3.278	3.283	3.286	3.291	3.285	3.283
45	3.277	3.281	3.285	3.289	3.294	3.296	3.299
55	3.279	3.284	3.288	3.291	3.296	3.298	3.3
65	3.284	3.292	3.297	3.299	3.305	3.303	3.304
75	3.299	3.32	3.33	3.333	3.335	3.335	3.335
85	3.32	3.328	3.332	3.334	3.336	3.335	3.336
90	3.325	3.33	3.333	3.335	3.337	3.336	3.337
95	3.329	3.332	3.335	3.337	3.34	3.339	3.339
100	3.345	3.344	3.349	3.37	3.505	3.515	3.504

Table A3- Battery Model Parameters: Discharge internal resistance (ohms)

SOC (%)	Temperature (°C)						
	-20	-10	0	10	25	35	45
0	0.0175	0.01	0.0075	0.0062	0.0034	0.0026	0.0021
5	0.0175	0.01	0.0075	0.0062	0.0034	0.0026	0.0021
10	0.0158	0.0095	0.0069	0.0052	0.0025	0.0019	0.0015

15	0.0144	0.009	0.0065	0.0047	0.0023	0.0017	0.0013
25	0.012	0.0082	0.0058	0.004	0.002	0.0016	0.0012
35	0.0105	0.0077	0.0053	0.0037	0.002	0.0015	0.0012
45	0.01	0.0073	0.005	0.0035	0.0019	0.0014	0.0012
55	0.0097	0.007	0.0048	0.0033	0.0018	0.0014	0.0011
65	0.0093	0.0067	0.0046	0.0032	0.0018	0.0013	0.0011
75	0.0091	0.0065	0.0046	0.0032	0.0018	0.0014	0.0012
85	0.0088	0.0063	0.0044	0.0031	0.0017	0.0013	0.0011
90	0.0087	0.0063	0.0043	0.003	0.0017	0.0013	0.0011
95	0.0086	0.0061	0.0043	0.0029	0.0016	0.0013	0.001
100	0.0086	0.0061	0.0043	0.0029	0.0016	0.0013	0.001

Table A4- Battery Model Parameters: Charge internal resistance (ohms)

SOC (%)	Temperature (°C)						
	-20	-10	0	10	25	35	45
0	0.0145	0.0079	0.0045	0.0028	0.0015	0.0012	0.0009
5	0.0145	0.0079	0.0045	0.0028	0.0015	0.0012	0.0009
10	0.0145	0.008	0.0045	0.0028	0.0015	0.0012	0.0009
15	0.0146	0.0081	0.0046	0.0028	0.0015	0.0012	0.0009
25	0.0153	0.0081	0.0046	0.0028	0.0015	0.0011	0.0009
35	0.0156	0.0084	0.0046	0.0027	0.0015	0.0011	0.0009
45	0.0161	0.0086	0.0047	0.0028	0.0015	0.0012	0.0009
55	0.0161	0.0087	0.0047	0.0028	0.0015	0.0012	0.001
65	0.0161	0.0087	0.0047	0.0028	0.0015	0.0012	0.001
75	0.0161	0.0086	0.0047	0.0027	0.0016	0.0012	0.001
85	0.0164	0.0084	0.0046	0.0028	0.0016	0.0012	0.001
90	0.0164	0.0083	0.0045	0.0028	0.0016	0.0013	0.0011
95	0.0166	0.0082	0.0045	0.0028	0.0017	0.0013	0.001
100	0.0166	0.0082	0.0045	0.0028	0.0017	0.0013	0.001

Table A5 - Battery Model Parameters: Maximum 10-second discharge power

	Temperature (°C)						
SOC (%)	-20	-10	0	10	25	35	45
0	140.5	245.8	323.3	378.5	502.7	520.6	536.2
5	140.5	245.8	323.3	378.5	502.7	520.6	536.2
10	157.9	263.3	356.7	433.9	541.3	566.0	581.1
15	173.8	278.1	383.1	458.9	555.9	576.9	590.9
25	211.3	309.3	422.6	490.9	570.3	588.8	600.7
35	242.5	334.1	442.9	510.2	579.9	597.0	607.6

45	254.8	353.0	455.7	519.1	583.5	601.5	612.1
55	264.2	369.5	465.3	526.2	587.2	604.3	615.0
65	275.6	385.2	473.7	532.5	591.0	607.3	617.8
75	286.8	403.3	482.3	539.9	595.0	611.0	621.0
85	300.0	411.9	488.7	544.8	598.2	614.0	623.5
90	304.9	415.3	493.3	547.3	600.1	615.5	625.1
95	309.4	421.4	496.3	551.1	602.7	617.1	626.8
100	309.4	421.4	496.3	551.1	602.7	617.1	626.8

Table A6 - Battery Model Parameters: Maximum 10-second charge power

	Temperature (°C)						
SOC (%)	-20	-10	0	10	25	35	45
0	79.7	162.5	313.4	534.6	705.1	674.6	662.5
5	79.7	162.5	313.4	534.6	705.1	674.6	662.5
10	77.5	153.7	292.4	498.1	706.9	691.3	682.8
15	75.9	147.7	275.9	478.7	709.5	692.9	683.6
25	73.9	137.0	252.2	442.5	715.3	699.1	690.7
35	72.5	132.8	242.7	410.3	718.9	703.3	694.9
45	72.1	132.4	241.4	403.8	719.5	705.5	697.8
55	71.8	132.1	240.8	402.3	717.6	705.6	697.7
65	72.9	131.2	235.4	394.8	704.1	706.3	698.1
75	71.0	124.0	213.0	348.5	636.0	712.3	704.3
85	68.9	121.5	211.8	343.2	626.6	713.3	704.9
90	68.4	121.2	214.2	342.2	624.2	713.5	704.7
95	67.4	121.9	213.6	340.0	617.1	714.1	705.5
100	67.4	121.9	213.6	340.0	617.1	714.1	705.5

Appendix B

This appendix contains plots comparing the experimental to model results for drive cycles at temperatures from -20°C to 45°C. The three drive cycles shown are the UDDS, HWFET, and US06.

B1 - UDDS

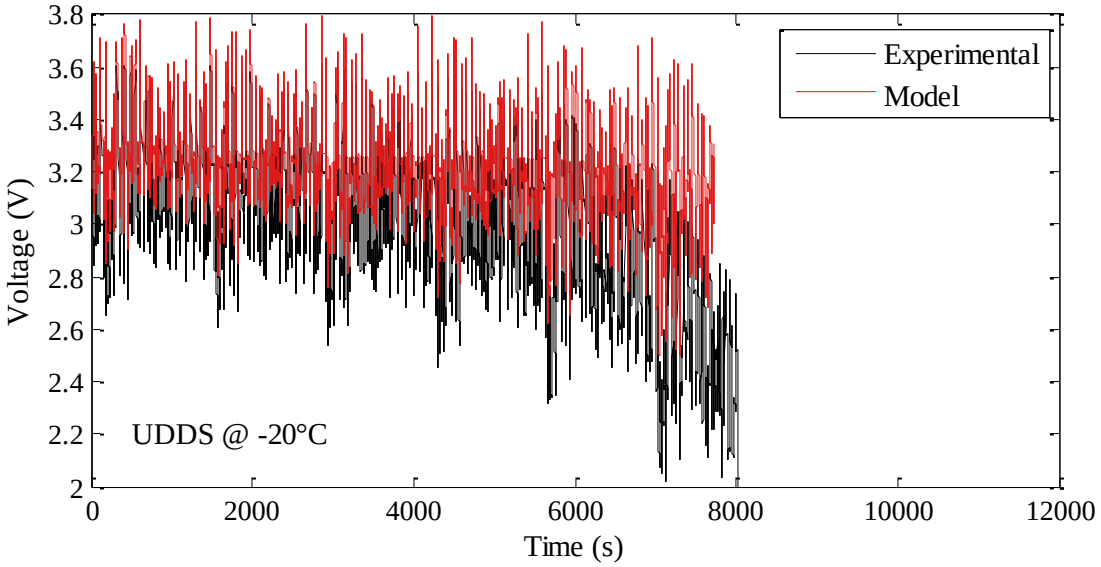

(a)

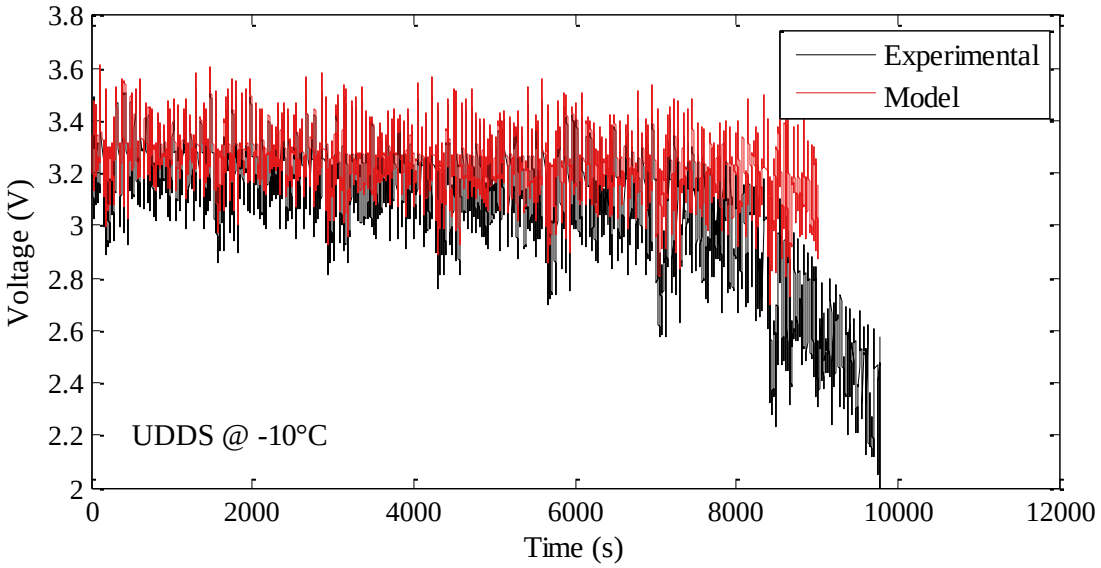

(b)

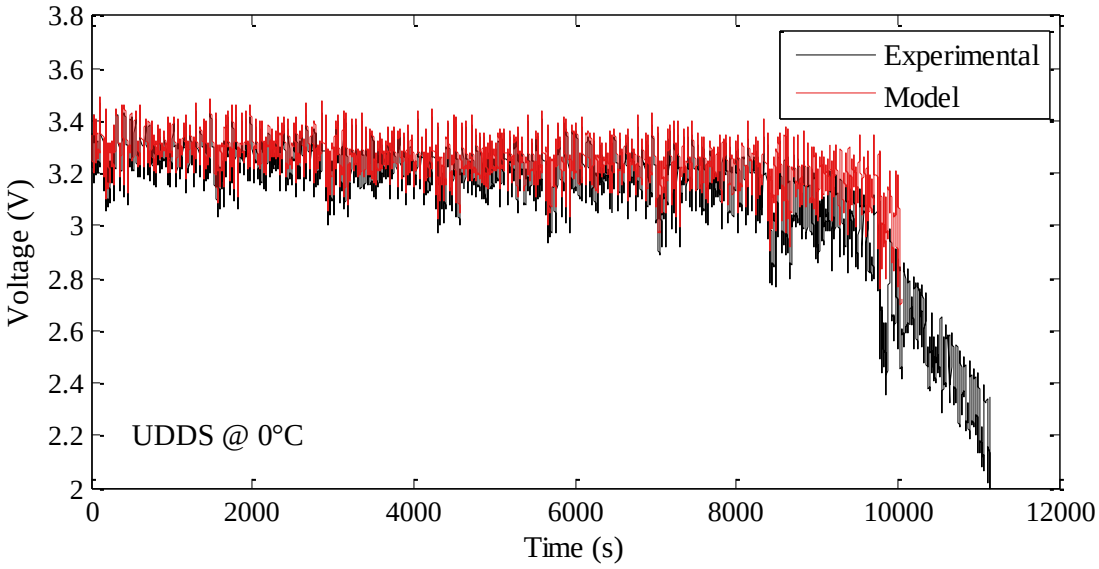
Experimental
Model
UDDS @ 0°C
Voltage (V)
Time (s)
3.8
3.6
3.4
3.2
3
2.8
2.6
2.4
2.2
2
0
2000
4000
6000
8000
10000
12000

(c)

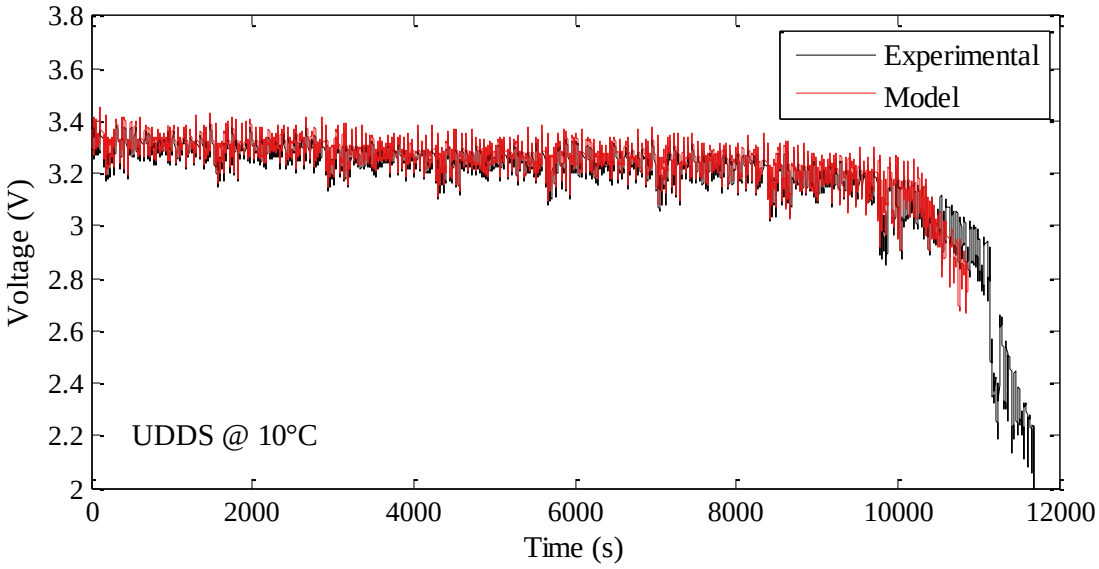
Experimental
Model
UDDS @ 10°C
Voltage (V)
Time (s)
3.8
3.6
3.4
3.2
3
2.8
2.6
2.4
2.2
2
0
2000
4000
6000
8000
10000
12000

(d)

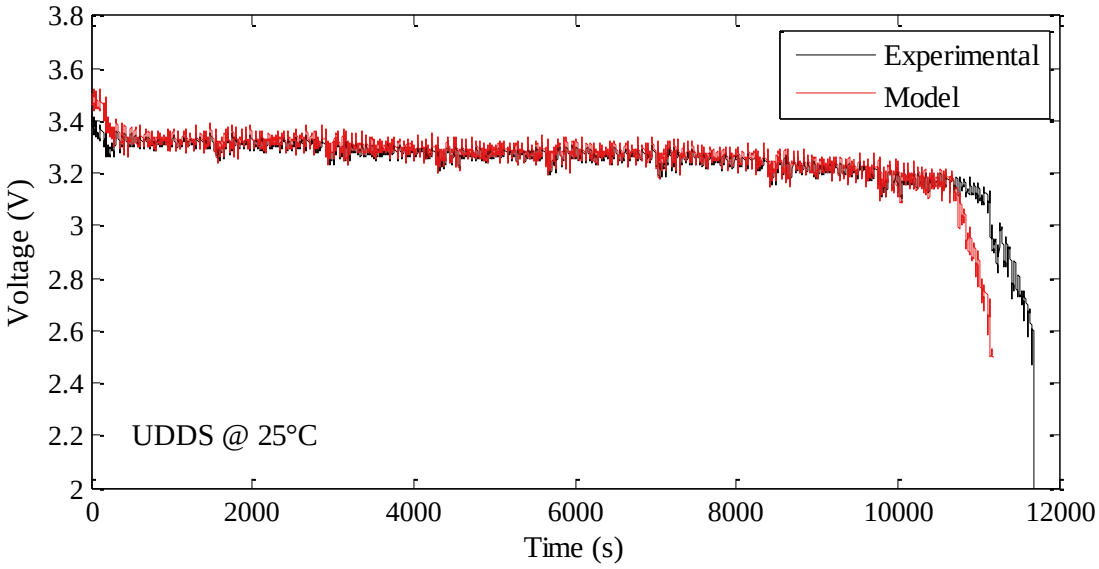
Experimental
Model
Voltage (V)
Time (s)
UDDS @ 25°C
3.8
3.6
3.4
3.2
3
2.8
2.6
2.4
2.2
2
0
2000
4000
6000
8000
10000
12000

(e)

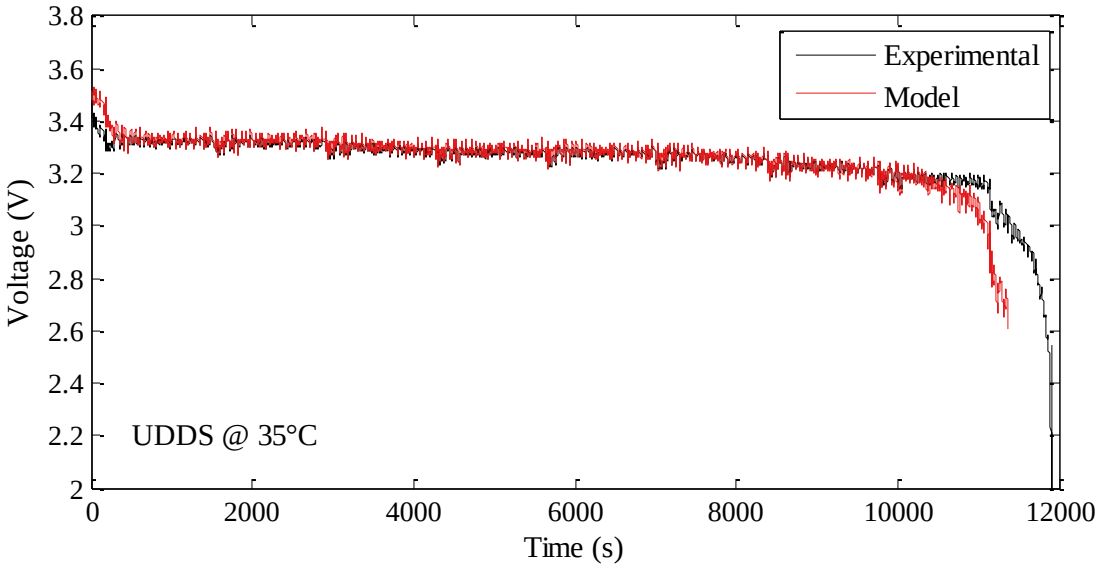
Experimental
Model
Voltage (V)
Time (s)
UDDS @ 35°C
3.8
3.6
3.4
3.2
3
2.8
2.6
2.4
2.2
2
0
2000
4000
6000
8000
10000
12000

(f)

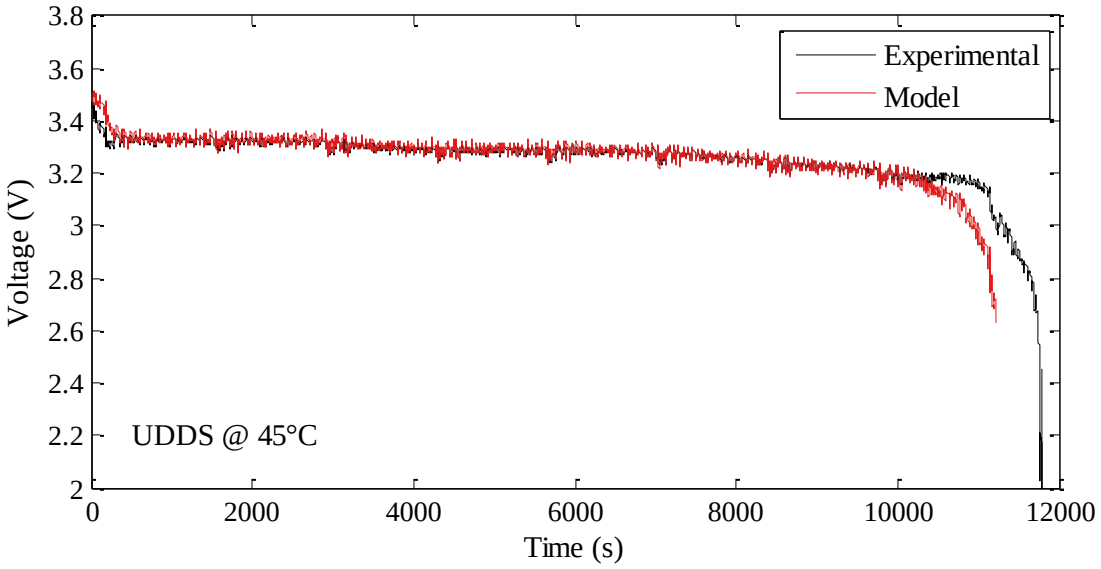

(g)

Figure B1 - Comparison between battery model and experimental results over a UDDS current profile for (a) -20°C; (b) -10°C; (c) 0°C; (d) 10°C; (e) 25°C; (f) 35°C; (g) 45°C

B2 - HWFET

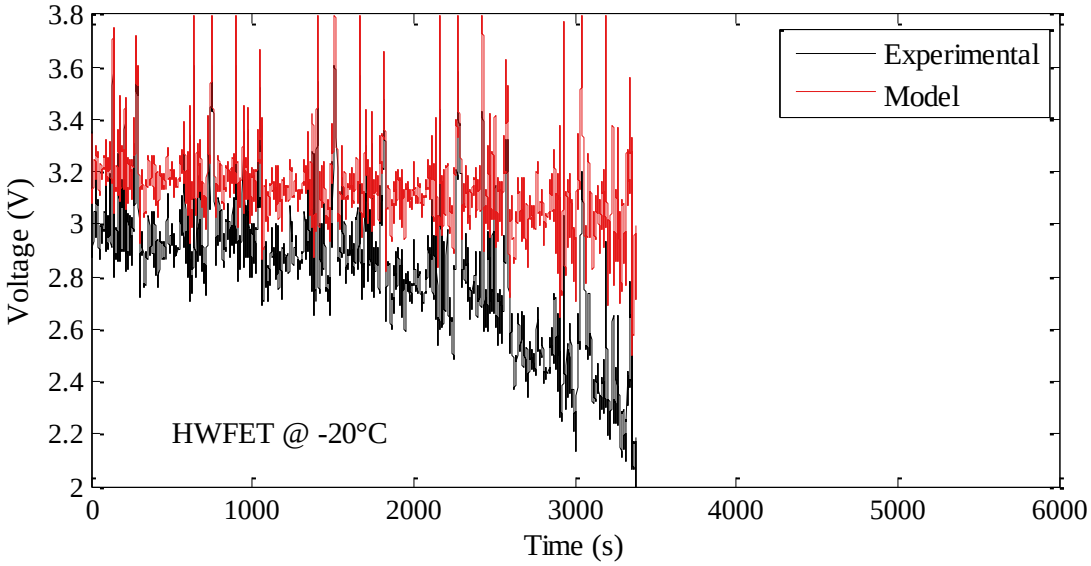
Experimental
Model
Voltage (V)
Time (s)
HWFET @ -20°C
3.8
3.6
3.4
3.2
3
2.8
2.6
2.4
2.2
2
0
1000
2000
3000
4000
5000
6000

(a)

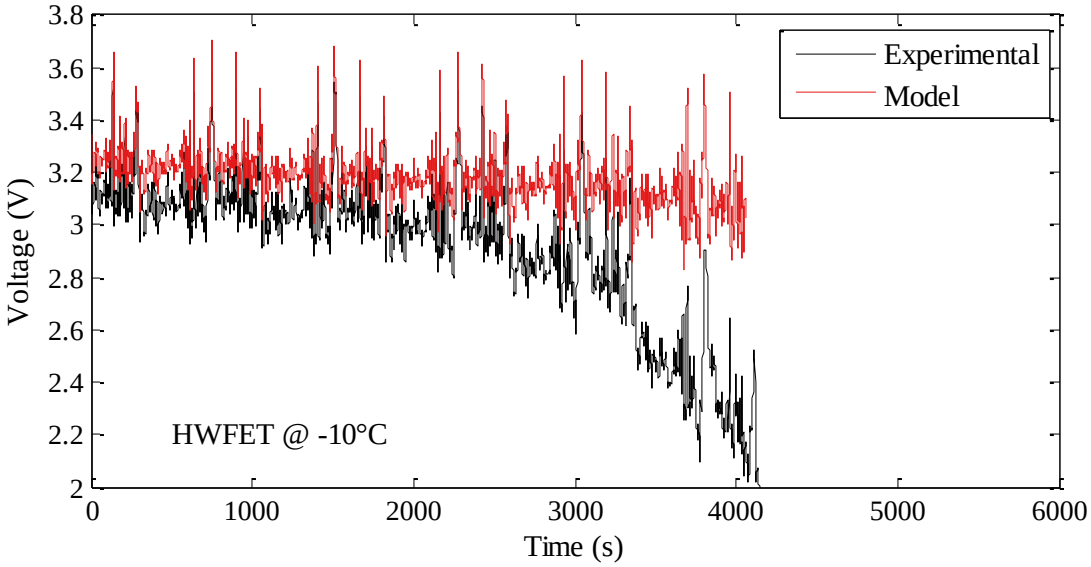
Experimental
Model
Voltage (V)
Time (s)
HWFET @ -10°C
3.8
3.6
3.4
3.2
3
2.8
2.6
2.4
2.2
2
0
1000
2000
3000
4000
5000
6000

(b)

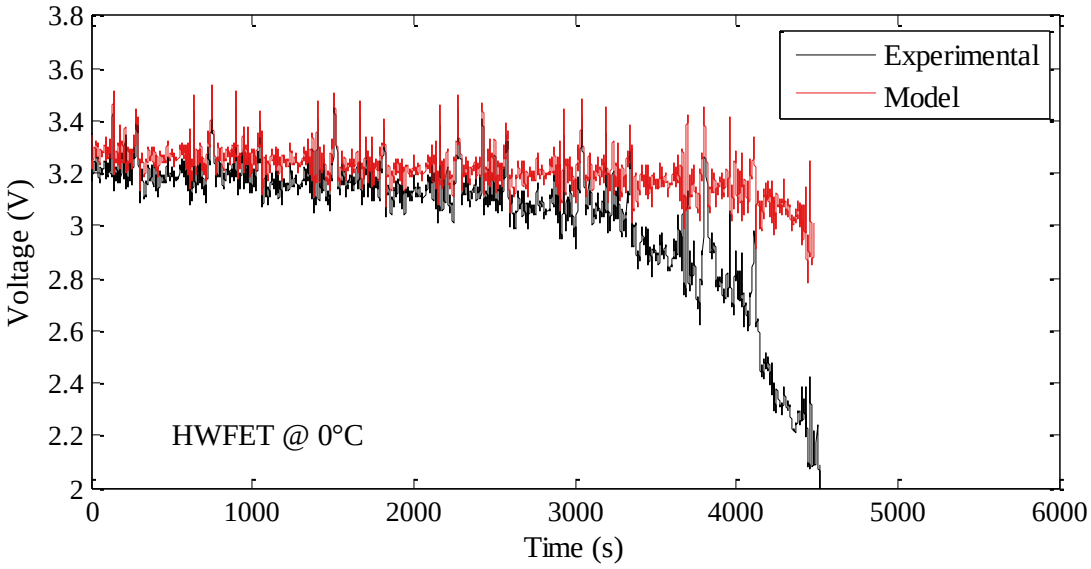
Experimental
Model
HWFET @ 0°C
Voltage (V)
Time (s)
3.8
3.6
3.4
3.2
3
2.8
2.6
2.4
2.2
2
0
1000
2000
3000
4000
5000
6000

(c)

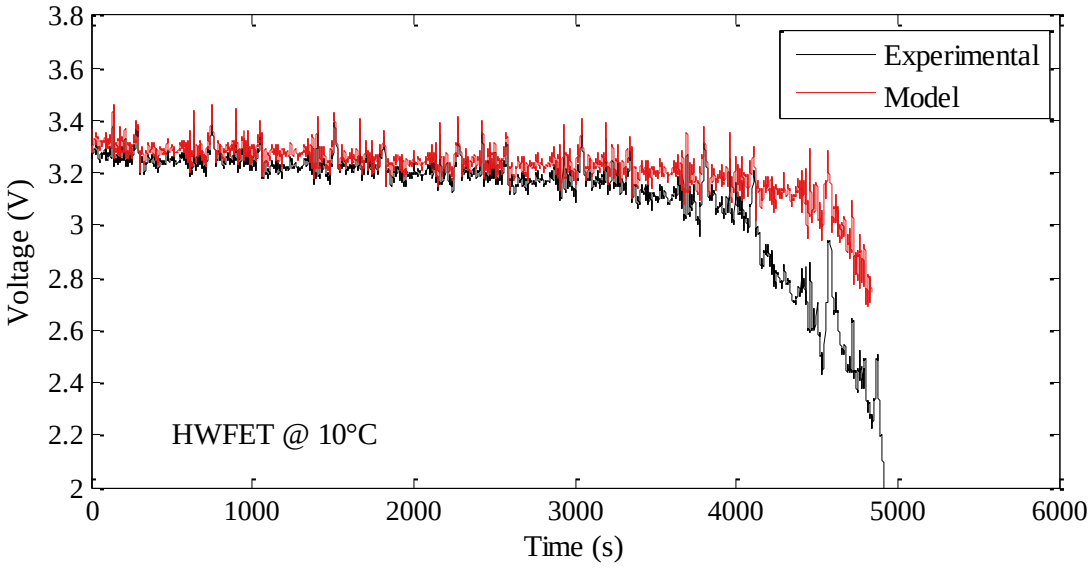
Experimental
Model
HWFET @ 10°C
Voltage (V)
Time (s)
3.8
3.6
3.4
3.2
3
2.8
2.6
2.4
2.2
2
0
1000
2000
3000
4000
5000
6000

(d)

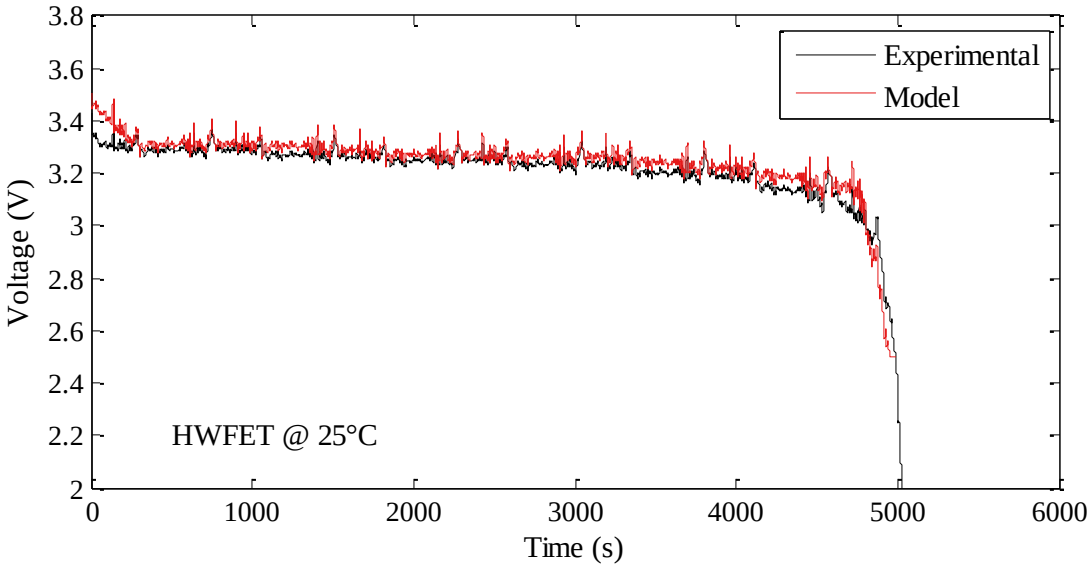
Experimental
Model
HWFET @ 25°C
Voltage (V)
Time (s)
3.8
3.6
3.4
3.2
3
2.8
2.6
2.4
2.2
2
0
1000
2000
3000
4000
5000
6000

(e)

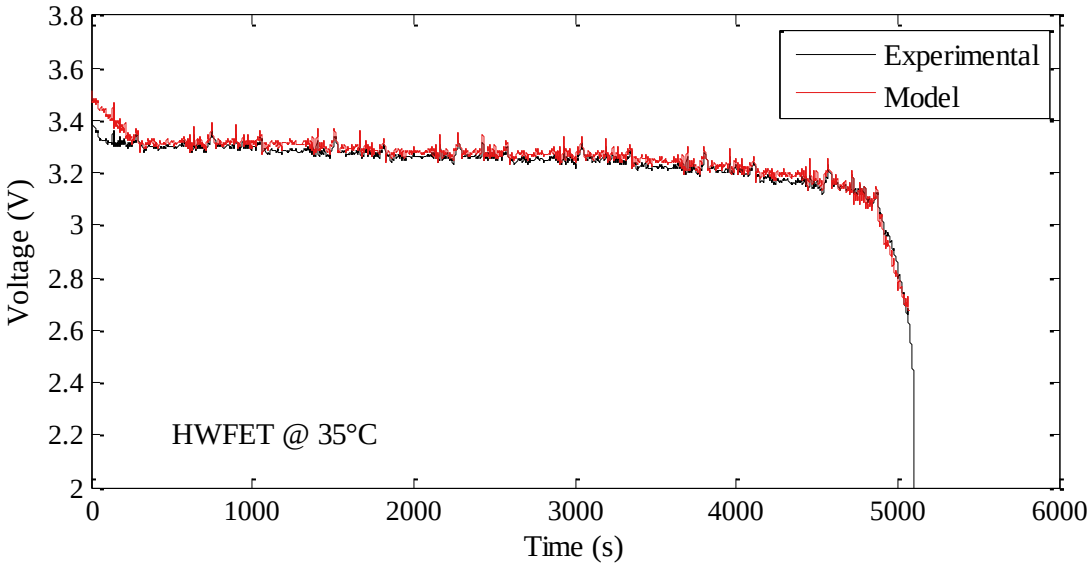
Experimental
Model
HWFET @ 35°C
Voltage (V)
Time (s)
3.8
3.6
3.4
3.2
3
2.8
2.6
2.4
2.2
2
0
1000
2000
3000
4000
5000
6000

(f)

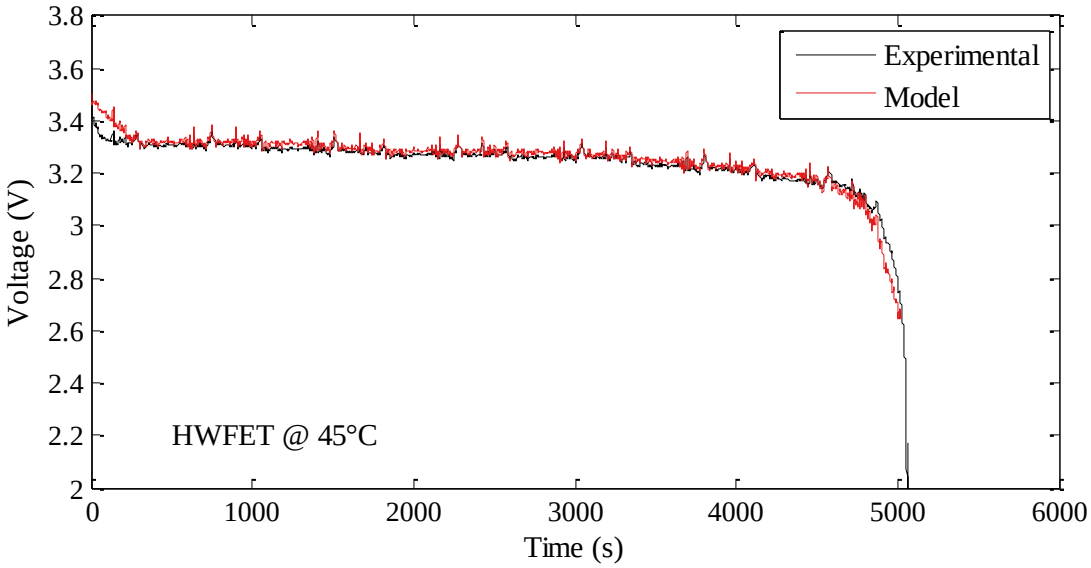

Figure B2 - Comparison between battery model and experimental results over a HWFET current profile for (a) -20°C; (b) -10°C; (c) 0°C; (d) 10°C; (e) 25°C; (f) 35°C; (g) 45°C

B3 - US06

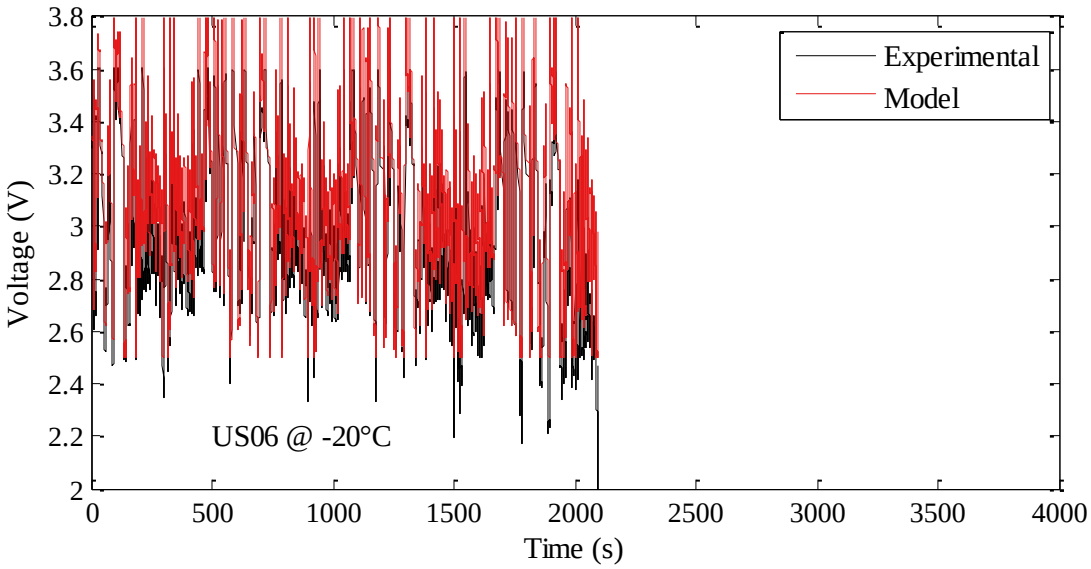
Experimental
Model
Voltage (V)
Time (s)
US06 @ -20°C
3.8
3.6
3.4
3.2
3
2.8
2.6
2.4
2.2
2
0
500
1000
1500
2000
2500
3000
3500
4000

(a)

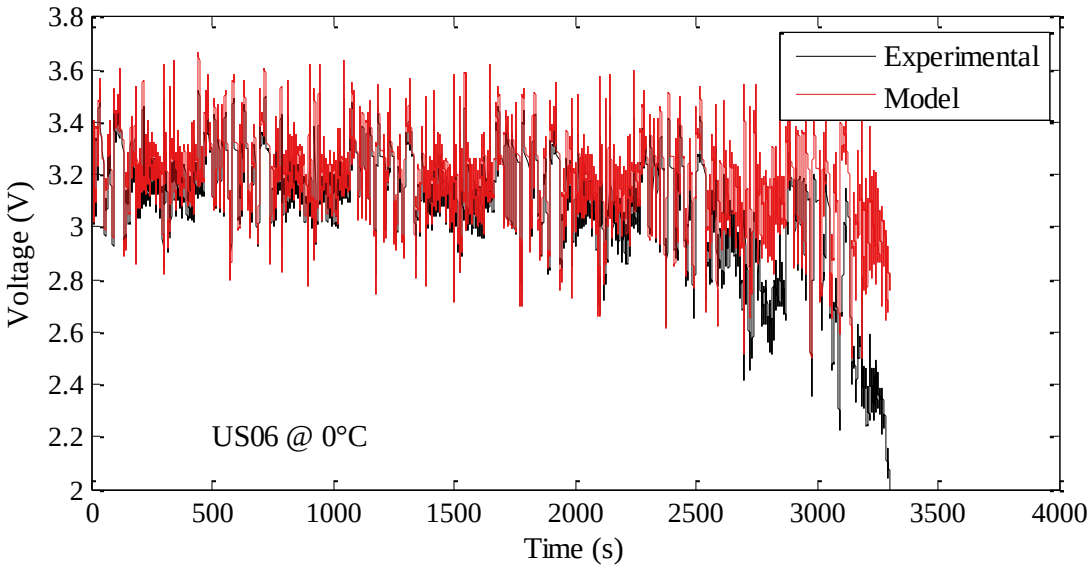
Experimental
Model
Voltage (V)
Time (s)
US06 @ 0°C
3.8
3.6
3.4
3.2
3
2.8
2.6
2.4
2.2
2
0
500
1000
1500
2000
2500
3000
3500
4000

(b)

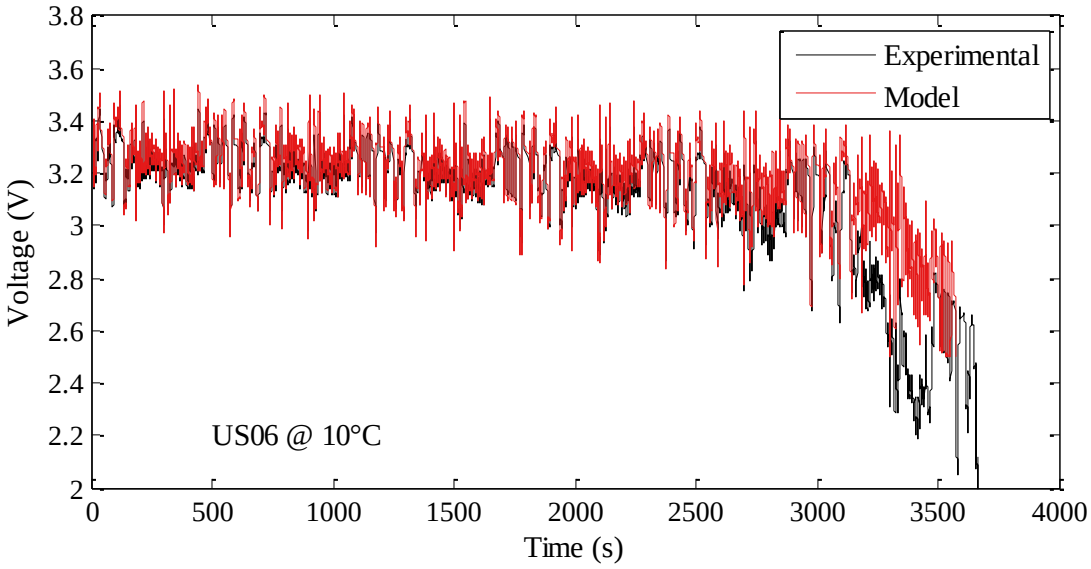
Experimental
Model
US06 @ 10°C
Voltage (V)
Time (s)
3.8
3.6
3.4
3.2
3
2.8
2.6
2.4
2.2
2
0
500
1000
1500
2000
2500
3000
3500
4000

(c)

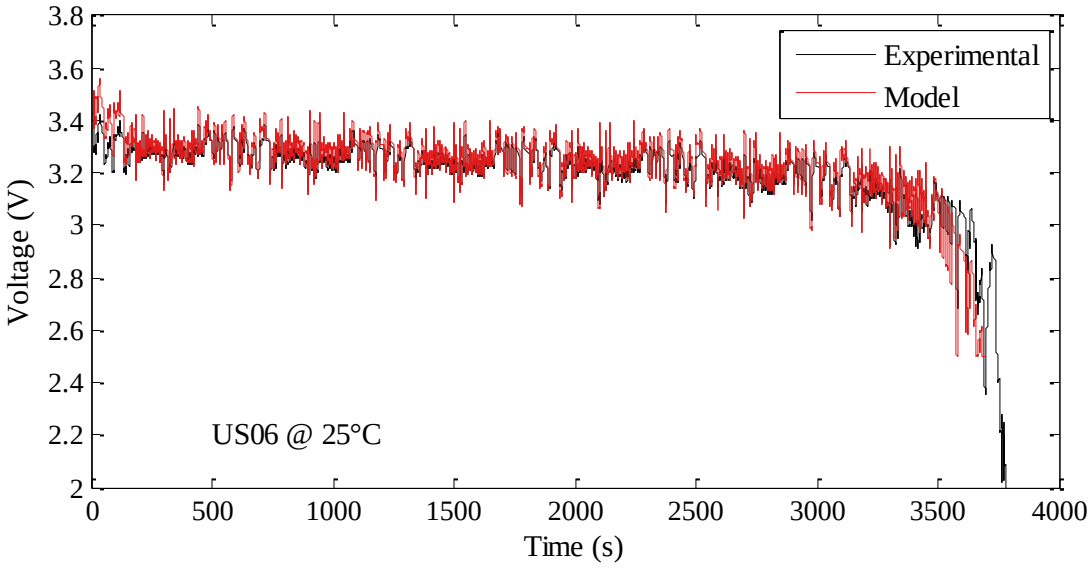
Experimental
Model
US06 @ 25°C
Voltage (V)
Time (s)
3.8
3.6
3.4
3.2
3
2.8
2.6
2.4
2.2
2
0
500
1000
1500
2000
2500
3000
3500
4000

(d)

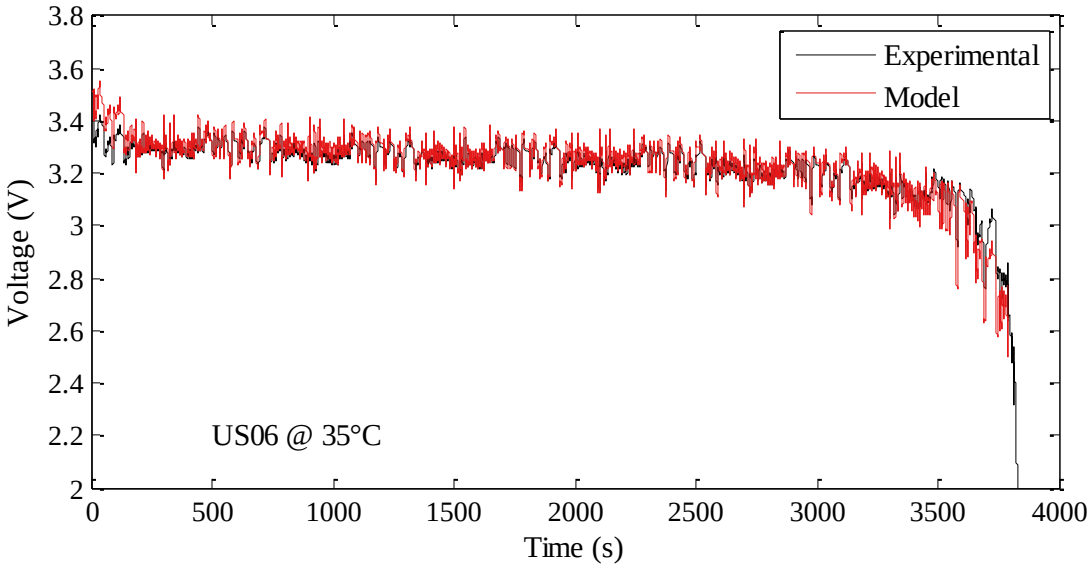

(e)

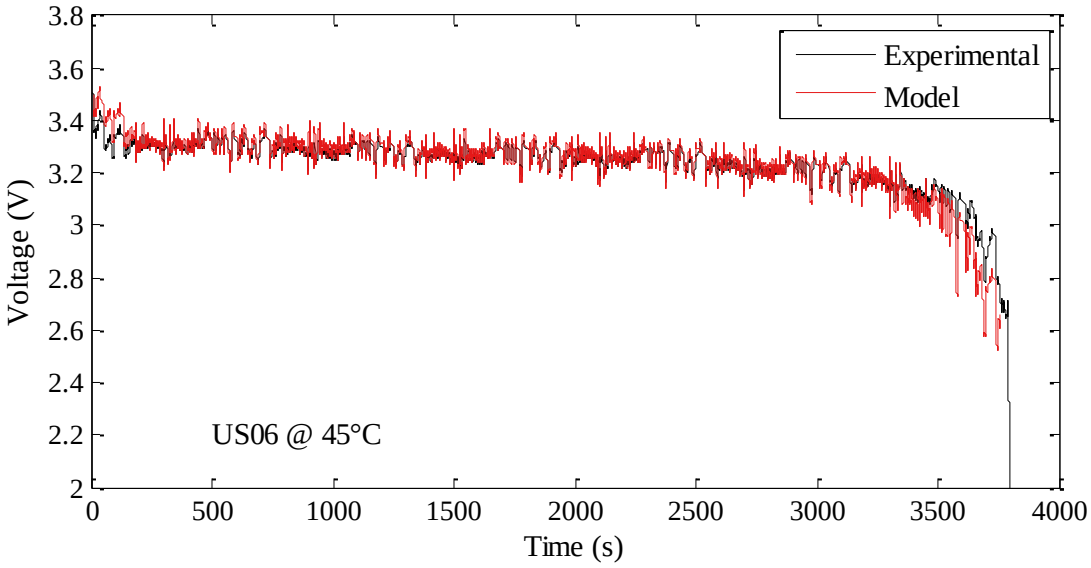

(f)

Figure B3 - Comparison between battery model and experimental results over a US06 current profile for (a) -20°C; (b) 0°C; (c) 10°C; (d) 25°C; (e) 35°C; (f) 45°C